IMPACT OF IRON(II)-INDUCED TRANSFORMATION OF IRON(III) (HYDR)OXIDES ON MOLYBDENUM MOBILITY IN GROUNDWATER

A Thesis Submitted to the College of

Graduate Studies and Research

In Partial Fulfillment of the Requirements

For the Degree of Master of Science

In the Department of Geological Sciences

University of Saskatchewan

Saskatoon

By

Kaixuan Qin

Permission to Use

In presenting this thesis in partial fulfillment of the requirements for a Postgraduate degree from the University of Saskatchewan, I agree that the Libraries of this University may make it freely available for inspection. I further agree that permission for copying of this thesis in any manner, in whole or in part, for scholarly purposes may be granted by the professor or professors who supervised my thesis work or, in their absence, by the Head of the Department or the Dean of the College in which my thesis work was done. It is understood that any copying or publication or use of this thesis/dissertation or parts thereof for financial gain shall not be allowed without my written permission. It is also understood that due recognition shall be given to me and to the University of Saskatchewan in any scholarly use which may be made of any material in my thesis.

Requests for permission to copy or to make other uses of materials in this thesis in whole or part should be addressed to:

Head of the Department of Geological Sciences
114 Science Place
University of Saskatchewan
Saskatoon, Saskatchewan, Canada
S7N 5E2

Abstract

Elevated concentrations of molybdenum (Mo) in groundwater are a growing concern at mines worldwide. However, information on geochemical controls of Mo mobility within mining environments are limited. Sorption onto Fe(III) (hydr)oxides is an important control on the mobility of metal(loid)s in soils, sediments and aquifers and is, therefore, an important mechanism of Mo attenuation within mine wastes and associated groundwater systems. However, sorption effectiveness depends on Mo speciation, pH, and redox conditions. There is potential for re-partitioning and release of associated Mo during Fe(II)-induced transformation of Fe (hydr)oxides. Column experiments were conducted to examine: (1) adsorption behaviour of molybdate (MoO_4^{2-}) on ferrihydrite [$Fe_2O_3 \cdot nH_2O$], goethite [α-FeOOH], and hematite [α-Fe_2O_3]; and (2) Mo re-partitioning during Fe(II)-induced reductive transformation of ferrihydrite and goethite. Results demonstrated that MoO_4^{2-} sorption capacity at circumneutral pH followed the general order: ferrihydrite > goethite > hematite. Subsequent reductive transformation by dissolved Fe(II) led to Mo re-partitioning without a substantial increase in Mo mobility. The extent of Mo mobilization was, however, greater at low (0.2 mM) compared to high (2.0 mM) Fe(II) concentrations. Furthermore, ferrihydrite generally exhibited stronger retention ability during reductive transformation – both for low and high Fe(II) concentrations – compared to goethite. Raman spectroscopy and scanning electron microscopy suggested that lepidocrocite [γ-FeOOH] was the major transformation product in the goethite and ferrihydrite columns. X-ray absorption spectroscopy (XAS) indicated that the Mo coordination environment changed from tetrahedral to octahedral during reduction, which suggests Mo might be incorporated into the transformed Fe phases with a disordered structure. This research improves our understanding of relationships between redox conditions, mineral transformations, and Mo mobility, which is critical for the development of Mo management and remediation strategies in mining environments.

Acknowledgements

This thesis would not be completed without the invaluable instruction and inspiration from my supervisor, Dr. Matt Lindsay. I am sincerely grateful for your guidance throughout the course of my Master's program. Experiencing culture shock and language barrier are inevitable to an international student. However, by showcasing experimental theory and encouraging the use of correct grammar, your patience and support helped me overcome many challenges. I feel lucky to be a member of the Environmental Geochemistry Group, and the graduate experience at the University of Saskatchewan will be one that I cherish forever.

Thank you to my committee members Dr. Derek Peak and Dr. Ning Chen, and the external examiner Dr. Andrew Grosvenor for the insightful comments and the constructive suggestions which enlightened me to think critically.

I would like to acknowledge Dr. Joyce McBeth, Sumaila Samira, Fina Nelson, Jing Chen, Tom Bonli, Eiko Kawamura, and Jason Maley for numerous technical help in PXRD, IC, ICP-OES, XRD, EM, SEM, and Raman spectroscopy. I am also deeply grateful to all Environmental Geochemistry group members, Jake Nesbitt and Dr. Soumya Das for collecting and analyzing XANES data as well as Mattea Cowell, Qingyang Liu, and Colton Vessey for water sampling and measurement. I am also thankful to my friends and family for the help and support.

Finally, financial support for this research was provided by the Natural Sciences and Engineering Council of Canada (NSERC) Discovery Grants program (Grant No. RGPIN-2014-06589). Additional training support was provided by the University of Saskatchewan (U of S) and the NSERC – Toward Environmentally Responsible Resource Extraction – Collaborative Research and Training Experience (NSERC-TERRE-CREATE) program (Grant No. CREAT 449124-2014). A portion of the research described in this thesis was performed at the Canadian Light Source, which is supported by the Canada Foundation for Innovation, NSERC, the U of S, the Government of Saskatchewan, Western Economic Diversification Canada, the National Research Council Canada, and the Canadian Institutes of Health Research.

Table of Contents

List of Tables

List of Figures

List of Abbreviations

AMD	Acid mine drainage
AWS	Acid washed sand
BSE	Back-scattered electron imaging
CLS	Canadian Light Source
EDS	Energy dispersive spectroscopy
EMPA	Electron microprobe analysis
EC	Eelectrical conductivity
FCS	Ferrihydrite-coated sand
FTIR	Fourier transform infrared spectroscopy
GCS	Goethite-coated sand
HCS	Hematite-coated sand
HXMA	Hard X-ray micro-analysis
IC	Ion chromatography
ICP-MS	Inductively coupled plasma - mass spectrometry
ICP-OES	Inductively coupled plasma - optical emission spectroscopy
ICSD	Inorganic crystal structure database
LCF	Linear combination fitting
PCA	Principal component analysis
PXRD	Powder X-ray diffraction
PZC	Point of zero charge
RS	Raman spectroscopy
SEM	Scanning electron microscopy
SSA	Specific surface area
WHO	World Health Organization
XANES	X-ray absorption near edge spectroscopy
XAS	X-ray adsorption spectroscopy
XRD	X-ray diffraction

Chapter 1 Introduction

Molybdenum has a wide range of applications in industry, such as manufacturing stainless steels and electronics, and as a catalyst in chemical and oil industries. For plants and animals, Mo is an essential trace element that catalyzes redox reactions as a metallic cofactor in enzymes (Xu et al., 2013). However, exposure to high concentrations of Mo can damage energy metabolism of human body, resulting in acute symptoms such as gout and diarrhea to chronic diseases including tremor and fatigue (Essilfie-Dughan et al., 2011; WHO, 2011; Smedley et al., 2014). Excessive uptake of Mo can also lead to Cu deficiency (molybdenosis) in ruminants (Carroll et al., 2006; Essilfie-Dughan et al., 2011; Helz et al., 2014). Geologically, Mo exists in combination with other elements forming minerals such as Molybdenite [MoS_2], ferrimolybdite [$Fe_2(MoO_4)_3 \cdot nH_2O$], powellite [$CaMoO_4$] and wulfenite [$PbMoO_4$], as well as associated with Fe and Al oxides and clays (Gustafsson, 2003; Essilfie-Dughan et al., 2011; Xu et al., 2013). These phases are commonly associated with uranium (U), copper (Cu), and arsenic (As). Consequently, elevated Mo concentrations are often observed in waste deposits generated at U, porphyry Cu, and other mines (Das et al., 2007; Essilfie-Dughan et al., 2011; Conlan et al., 2012; Helz et al., 2014; Sejkora et al., 2014). Biogeochemical weathering of minerals within these wastes can release Mo to adjacent surface and groundwater systems.

Powellite [$CaMoO_4$] and wulfenite [$PbMoO_4$] are potential solubility controls on dissolved Mo in mine wastes (Essilfie-Dughan et al., 2011; Conlan et al., 2012; Hayes et al., 2014). Sorption represents another important mechanism of Mo attenuation in these systems (Goldberg et al., 1996; Essilfie-Dughan et al., 2011; Hayes et al., 2014). Iron (hydr)oxides are a principal sorbent of Mo in soils, sediments and aquifers, and in mine wastes (McKenzie, 1983; Goldberg and Forster, 1998; Kim and Jang, 2010; Xu et al., 2013). These minerals may contain Fe(III) and/or Fe(II) and range from poorly crystalline phases such as lepidocrocite [γ-FeOOH] and ferrihydrite [$Fe_2O_3 \cdot nH_2O$], to more crystalline phases including goethite [α-FeOOH], hematite[α-Fe_2O_3], and magnetite [Fe_3O_4] (Schwertmann and Cornell, 2000; Benner et al., 2002; Usman et

al., 2012a). Green rust, which is a group of layered double hydroxides, is another potential sorbent of Mo in the environment. These metastable phases have a general formula of $[Fe^{II}_{(1-x)}Fe^{III}_{x}(OH)_2]^{x+}[x/nA^{n-}\cdot mH_2O]^{x-}$, where A^{n-} represents interlayer anions including SO_4^{2-}, CO_3^{2-}, Cl^-, and OH^- (Schwertmann and Fechter, 1994; Zegeye et al., 2007; Usman et al., 2012b). Iron (hydr)oxides do not always occur as discrete phases; instead, these phases often form coatings on less reactive particles such as sand in soils and sediments (Ryan and Gschwend, 1994; Hanna et al., 2010; Rusch et al., 2010; Sergent et al., 2011). Although Fe (hydr)oxides commonly compose a small fraction of soils, sediments, and aquifers, they are important sorbents for a variety of environmental contaminants including As, Se, and Mo (Hayes et al., 1988; Sherman and Randall, 2003; Gomez et al., 2013). This behaviour is attributed to the intrinsic chemical and physical properties of these Fe phases. For example, Fe (hydr)oxides generally have a high specific surface area (SSA) and point of zero charge (PZC) between 6.5 and 8.5, which facilitates sorption of anions under acidic to circumneutral pH conditions (Schwertmann and Cornell, 2000; Xu et al., 2006; Hanna et al., 2010). Consequently, sorption onto Fe (hydr)oxides is an important control on the fate and transport of Mo in the environment.

Molybdenum is generally not a concern in acidic mine drainage (AMD) systems, where sorption onto Fe (hydr)oxides effectively limits its mobility (Goldberg et al., 1996; Gustafsson, 2003; Xu et al., 2006; Conlan et al., 2012). However, Mo adsorption decreases as pH increases from circumneutral to alkaline pH values (Das et al., 2007; Conlan et al., 2012). Since sulfide mine wastes often evolve from circumneutral to acidic pH conditions over time (Lindsay et al., 2015), understanding the adsorption under circumneutral pH conditions is important for predicting initial Mo mobility in mining environments. Previous studies have investigated the adsorption behaviour of Mo on ferrihydrite, goethite, and hematite, which are abundant in mine wastes and in soils, sediments, and aquifers (Goldberg et al., 1996; Xu et al., 2006; Das and Hendry, 2013). However, these studies have largely focused on equilibrium sorption in batch experiments (Lang et al., 2000; Gustafsson, 2003; Xu et al., 2006; Arai, 2010; Dodbiba et al., 2011). These conditions may not reflect sorption under dynamic flow conditions. In contrast to batch experiments, column tests can be used to examine temporal and spatial influences of transport on Mo sorption (Hanna et al., 2013). Column experiments examining Mo adsorption on Fe (hydr)oxides have not yet been reported.

Changes in redox conditions can alter the stability of Fe (hydr)oxides and, therefore, the mobility of associated elements (Kocar et al., 2006; Boland et al., 2011; Burton et al., 2011; Das et al., 2015). A transition from oxic to anoxic conditions can induce reductive dissolution and/or transformation of Fe (hydr)oxides, resulting in re-partitioning of the associated elements. During reclamation, mine wastes tailings are often covered – commonly with soil, clay, sand or composites of these materials – to limit water infiltration and oxygen ingress, and to reduce long-term oxidative weathering. However, cover systems can also promote the development of reducing conditions within underlying mine wastes (Paktunc, 2013). In addition, water-table fluctuations within partially-saturated mine wastes could change redox conditions and, potentially, alter element mobility (Mok and Wai, 1990; Balistrieri et al., 2003; Bonzongo et al., 2006). During such changes, sorbed metal(loid)s may be released to pore water (Paktunc, 2013) or retained via adsorption or co-precipitation with transformation products or secondary reaction products (Paktunc and Davé, 2002; Paktunc, 2013). Although changes in redox conditions are likely to influence Mo mobility, the potential for enhanced transport or attenuation during a transition to reducing conditions remains unclear. Understanding how adsorption and reduction of Fe (hydr)oxides influence Mo re-partitioning is critical for predicting and managing Mo contamination in mining environments.

1.1 Molybdenum geochemistry

Molybdenum is a group 6B transition metal with 6 positive oxidation states and six stable isotopes. However, Mo(VI) is the dominant oxidation state found in water, soils, and sediments. Although Mo is an essential trace nutrient, exposure to high concentrations can impact energy metabolism in humans, resulting in acute symptoms such as gout and diarrhea or chronic diseases including tremors and fatigue (WHO, 2011; Xu et al., 2013; Smedley et al., 2014). Excessive Mo exposure may interfere with Cu assimilation, thus leading to Cu deficiency in ruminants (Carroll et al., 2006; Essilfie-Dughan et al., 2011; Helz et al., 2014). Considering the potential for negative health effects, the World Health Organization (WHO) has established a 70 μg L^{-1} guideline for Mo in drinking water (WHO, 2011). Nevertheless, Mo concentrations are well below this WHO guideline in most waters (Dalai et al., 2005; Smedley et al., 2014). Data obtained for 38 rivers from five continents revealed an average Mo concentration of 0.8 μg L^{-1} (Miller et al., 2011). However, streams and groundwater impacted by industrial activities (e.g.,

mining operations) can exhibit much higher dissolved Mo concentrations (Smedley et al., 2014). Concentrations up to 200 μg L^{-1} have been reported for treated effluents from Mo mining operations (WHO, 2011). Kargar et al. (2011) reported that Mo concentrations in groundwater near Miduk Copper Complex of Iran reached 1175 μg L^{-1}. Finally, Mo concentrations up to 10000 μg L^{-1} have been reported in drainage from waste rock at a large Cu-Zn mine in Peru (Conlan et al., 2012). Naturally occurring Mo contamination can result from weathering of sulfide-bearing minerals or reductive dissolution of Mo-bearing Fe (hydr)oxides (Rocco and Rubio, 2010; Miller et al., 2011). Dissolved Mo concentrations in both natural and industrial areas are controlled by several factors including aqueous Mo speciation, pH, redox potential, sorption-desorption and precipitation-dissolution reactions. These factors strongly influence the potential for Mo transport and attenuation in soils, sediments and aquifers. As these factors are interrelated, understanding how individual conditions influence Mo fate and transport is important to the development of effective management and remediation strategies.

1.1.1 Aqueous speciation

Molybdenum geochemistry is relatively complex; however, the dominant oxidation state in the environment is Mo(VI), which mainly occurs in tetrahedral coordination as molybdate (MoO_4^{2-}) oxyanion (Goldberg et al., 1996; Xu et al., 2013). Aqueous speciation largely depends on solution pH and Mo concentration (Bourikas et al., 2001). These two factors influence Mo mobility by controlling protonation and polymerization. Molybdenum tends to occur as the soluble MoO_4^{2-} oxyanion under circumneutral to alkaline pH conditions. Sorption of MoO_4^{2-} is limited under these pH conditions, where net surface charges for Fe(III) (hydro)oxides are negative. These trends are consistent with the positive relationship between Mo concentrations and pH observed in British streams (Smedley et al., 2014). In contrast, Mo can protonate to form $MoO_3(H_2O)_3$ under acidic pH conditions (i.e., pH < 4), which can affect sorption affinity by the altering ion charge. At high concentrations (e.g., 10^{-3} M) and low pH values (e.g., pH 3), MoO_4^{2-} tends to polymerize and form polymolybdates such as $Mo_7O_{24}^{5-}$ and $Mo_8O_{26}^{4-}$ (Cruywagen, 2000; Xu et al., 2013). Understanding Mo aqueous speciation is important for precluding the interference of polymolybdates in the investigation of sorption behaviour.

Molybdate is generally the most stable species in oxic to suboxic soils, sediments, and aquifers. Sulfidization of MoO_4^{2-} under sulfate-reducing conditions can, however, produce a

series of intermediate thiomolybdate species including MoO_3S^{2-}, $MoO_2S_2^{2-}$, $MoOS_3^{2-}$ and MoS_4^{2-} (Erickson and Helz, 2000; Xu et al., 2013):

$$MoO_xS_{4-x}^{2-} + H_2S_{(aq)} \rightarrow MoO_{x-1}S_{5-x}^{2-} + H_2O,\ 1 \leq x \leq 4 \quad \text{.....(1.1)}$$

Thiomolybdates ($MoO_xS_{4-x}^{2-}$) are particularly reactive, with a higher potential for attenuation by either co-precipitation or adsorption (Helz et al., 1996; Das et al., 2007). Bostick et al. (2003) investigated the sorption of MoO_4^{2-} and MoS_4^{2-} onto pyrite [FeS_2] and discovered that MoS_4^{2-} forms strong Fe-Mo-S cubane complexes, whereas MoO_4^{2-} forms weak bidentate Mo-O complexes; consequently, an increase in pH promoted desorption of MoO_4^{2-} but not MoS_4^{2-}. These findings suggest that Mo is likely to be more strongly attenuated under sulfate-reducing conditions compared to oxic conditions (Adelson et al., 2001).

Table 1.1: Selected pH-dependent reactions of polymolybdates in solutions.

No	Reactions	pK_a
(1)	$HMoO_4^- + H^+ \rightarrow H_2MoO_4$	4.00
(2)	$MoO_4^{2-} + H^+ \rightarrow HMoO_4^-$	4.24
(3)	$7MoO_4^{2-} + 8H^+ \rightarrow Mo_7O_{24}^{6-} + 4H_2O$	52.86
(4)	$8MoO_4^{2-} + 12H^+ \rightarrow Mo_8O_{26}^{4-} + 6H_2O$	74.38

pK_a values from Xu et al. (2013).

1.1.2 Molybdenum sorption and desorption

The mobility of MoO_4^{2-} in the environment is largely dependent on sorption reactions at mineral surfaces, particularly in oxic environments. The effectiveness of Mo removal via Fe (hydr)oxides sorption has been intensively investigated. Dissolved Mo tends to be effectively removed by sorption or co-precipitation with Fe(III) (hydr)oxides (Legendre and Runnells, 1975) and Mo is commonly associated with these phases in soils (McKenzie, 1983). Helz et al. (2011) suggested that under acidic to circumneutral pH conditions, Mo removal would occur wherever sufficient reactive Fe(III) is present.

The adsorption of Mo(VI) to Fe (hydr)oxides in soils, sediments, and aquifers may include outer- and inner-sphere surface complexes. Outer-sphere complexation involves electrostatic attraction whereas inner-sphere complexation involves ligand exchange. Typically, physical adsorption is a precursor for inner-sphere complexation; therefore, anions with the potential to form inner-sphere complexes compete with those that tend to form outer-sphere complexes. The

extent of complexation depends largely on the pH, ionic strength, the adsorbent, the adsorbate, as well as the competing ions (Goldberg et al., 1996; Goldberg, 2009, 2010). In general, MoO_4^{2-} adsorption onto clay minerals and Fe (hydr)oxides involves inner-sphere complexation via ligand exchange with surface hydroxyl (-OH) groups (Hayes et al., 1988; Zhang and Sparks, 1989; Bibak and Borggaard, 1994; Gustafsson, 2003; Arai, 2010; Xu et al., 2013). Competition between Mo and other oxyanions (e.g., PO_4^{3-}, SO_4^{2-}) can impact surface complexation reactions. For example, the presence of PO_4^{3-}, which also forms inner-sphere complexes, can reduce the extent of Mo adsorption. In contrast, SO_4^{2-} generally forms outer-sphere complexes and has a lesser impact on Mo adsorption (Goldberg and Forster, 1998; Goldberg, 2010; Xu et al., 2013). The impact of these competing ions on MoO_4^{2-} sorption is also dependent upon the relative concentrations in solution. The adsorption behaviour of Mo strongly depends on pH and surface loading, though it may vary with the type of adsorbent and ionic strength.

1.1.3 Adsorption by Fe (hydr)oxides

Several studies have examined the adsorption of MoO_4^{2-} by Fe (hydr)oxides. Goldberg et al. (1996) discovered that the pH dependence of Mo adsorption onto hematite, goethite, poorly crystalline goethite, and ferrihydrite follow similar trends (Fig. 1.1). Maximum Mo sorption is achieved at pH 4 to 5, where $HMoO_4^-$ and MO_4^{2-} become the dominant species at pH above 4.00 and 4.24, respectively (Vlek and Lindsay, 1977; Bibak and Borggaard, 1994). Adsorption decreases gradually with pH increasing from pH 6 to 10 as the surface charge of Fe (hydr)oxides becomes negative (Bibak and Borggaard, 1994). For the common Fe (hydr)oxides, sorption capacity follows the general order: ferrihydrite > goethite > hematite, and McKenzie (1983) explained that this is attributed to the surface area of adsorbents. Generally, Mo adsorption is higher for less crystalline Fe phases (i.e., ferrihydrite), which exhibit higher specific surface areas (McKenzie, 1983; Goldberg et al., 1996). This result is consistent with findings of Goldberg et al. (1996), which demonstrated that goethite adsorbs more Mo than hematite per unit mass. These results indicate that surface area may be the intrisinc control on the sorption capacity of Fe (hydr)oxides. Additionally, the PZC of the adsorbent can also affect the adsorption capacity at a given pH. Since the specific surface area of goethite and kaolinite are comparable (McKenzie, 1983; Bibak and Borggaard, 1994; Schwertmann and Cornell, 2000; Khawmee et al., 2013), the difference in sorption capacity versus pH is attributed largely to difference in PZC for goethite

(6.5 - 8.5) relative to kaolinite (2.0 – 3.1) (Schwertmann and Cornell, 2000; Khawmee et al., 2013).

Ionic strength, temperature, and competing anions have a lesser impact on Mo sorption than pH and surface area (Hayes et al., 1988; Zhang and Sparks, 1989; Goldberg et al., 1996). Zhang and Sparks (1989) conducted sorption experiments using $NaNO_3$ (0.01 to 0.1M) as the background electrolyte and observed limited ionic strength dependence for Mo adsorption on goethite. Inner-sphere complexation of MoO_4^{2-} is the dominant Mo sorption mechanism at pH greater than 4 (Zhang and Sparks, 1989). Adsorption was found to follow two consecutive steps: (1) MoO_4^{2-} forms an ion-pair complex with the protonated surface through electrostatic interaction; (2) ligand exchange forms an inner-sphere surface complex. X-ray adsorption spectroscopy (XAS) studes showed that the coordination of sorbed MoO_4^{2-} on goethite changes from tetrahedral (MoO_4^{2-}) to octahedral (MoO_6) with decreasing pH (pH < 4) (Arai, 2010). This result suggests that under acidic conditions, polymerization is enhanced at high Mo loadings and may further promote Mo adsorption (Antelo et al., 2012).

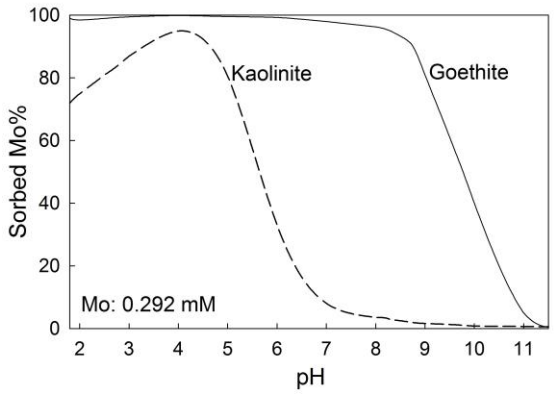

Figure 1.1: Mo adsorption on goethite (solid line) and kaolinite (dashed line) as a function of solution pH (initial Mo concentration: 0.292 mM) (after Goldberg and Forster, 1998).

Molybdenum adsorption onto ferrihydrite has received less attention compared to goethite. However, sorption onto ferrihydrite is likely an important control on Mo mobility in the environment (Goldberg et al., 1996; Gustafsson, 2003; Gomez et al., 2013). Gustafsson (2003) observed complete MoO_4^{2-} adsorption (50 µM) onto ferrihydrite at pH below 5 with a Fe:Mo ratio of 6; maximum MoO_4^{2-} adsorption extends to pH 6 for Fe:Mo ratios of 20 and 60. This study also demonstrated that competitive adsorption of PO_4^{3-} could shift the MoO_4^{2-} adsorption envelope on ferrihydrite down by approximately two pH units. Surface complexation modeling

suggested that H_2MoO_4 forms monodentate complexes with ferrihydrite at low pH. However, Bibak and Borggaard (1994) used Fourier transform infrared (FTIR) spectroscopy to show that Mo forms inner-sphere monodentate and bidentate complexes with ferrihydrite.

Hematite has a much lower Mo adsorption capacity than both ferrihydrite and goethite, which is mainly attributed to its lower surface area (McKenzie, 1983; Goldberg et al., 1996). Kim and Jang (2010) found that Mo adsorption on hematite at pH around 2 reaches equilibrium in 24 h, with 42 and 29% sorbed for initial concentrations of 0.20 and 0.40 mmol kg^{-1} hematite, respectively. The aging effect corresponds to a slight increase in Mo sorption on hematite at pH 10; however, the crystal morphology and specific surface area remains unchanged (Das and Hendry, 2013).

Previous studies have suggested that inner-sphere complexation is the main mechanism of MoO_4^{2-} adsorption onto Fe (hydr)oxides (Zhang and Sparks, 1989; Bibak and Borggaard, 1994; Goldberg, 2010). However, the recrystallization of poorly-crystalline phases (e.g., ferrihydrite) into more crystalline and thermodynamically stable forms (e.g., goethite, hematite) may promote re-partitioning of associated contaminants (Schwertmann and Cornell, 2000; Das et al., 2011b; Masue-slowey et al., 2011). Reductive dissolution of Fe (hydr)oxides also has the potential to release adsorbed Mo; nonetheless, formation of secondary products may also improve Mo attenuation (Gomez et al., 2013). Accordingly, the long-term fate and transport of Mo depend largely on the interaction between Mo and Fe (hydr)oxides under a range of conditions.

1.2 Reductive transformation of Fe (hydr)oxides

The oxidative weathering of Fe(II)-bearing minerals including pyrite in mining settings can promote the formation of Fe (hydr)oxides (Das and Hendry, 2013). Ferrihydrite, which is the most common initial phase to precipitate from rapid hydrolysis of Fe(III), transforms under oxic conditions to more crystalline goethite and hematite with time (Schwertmann and Cornell, 2000; Benner et al., 2002; Cudennec and Lecerf, 2006; Das and Hendry, 2013; Brinza et al., 2015). Two principal transformation pathways have been identified: (1) goethite forms under acidic and alkaline conditions via dissolution/re-crystallization (i.e., Ostwald ripening); (2) hematite forms at elevated temperature and circumneutral pH through dehydration (i.e., solid state transformation) (Schwertmann and Cornell, 2000; Benner et al., 2002; Schwertmann et al., 2004; Cudennec and Lecerf, 2006; Lu et al., 2011; Das and Hendry, 2013; Brinza et al., 2015). Transformation of

ferrihydrite to goethite and hematite generally reduces the surface area of Fe (hydr)oxides available for sorption. However, the transformation rates in the environment are typically slow and can take years to centuries (Kocar et al., 2006; Das et al., 2011a).

In contrast, a transition to anoxic conditions can reduce the stability of Fe (hydr)oxides within a short time (Hansel et al., 2003; Herbel and Fendorf, 2006; Kocar et al., 2006). Under anoxic conditions, Fe(III) can serve as an electron acceptor for anaerobic respiration by Fe-reducing bacteria. These bacteria couple reduction of Fe(III) to Fe(II) with the oxidation of organic carbon (Lovley and Phillips, 1988). The presence of Fe(II) can induce the recrystallization of Fe (hydr)oxides into more crystalline and thermodynamically stable phases (e.g., goethite, magnetite) within days to weeks (Kocar et al., 2006; Zegeye et al., 2007; Gomez et al., 2013). Despite decreases in surface area, transformation products have the potential to retain the associated metal(loid)s either through re-adsorption or incorporation (Kocar et al., 2006). Therefore, Fe(II)-induced reduction can have a profound impact on both Fe (hydr)oxides and associated metal(loid)s.

Transformation of poorly crystalline, metastable ferrihydrite to more crystalline phases under anoxic conditions has been the focus of several studies (Benner et al., 2002; Hansel et al., 2003, 2005; Kocar et al., 2006; Yang et al., 2010; Das et al., 2011a). Common secondary products of Fe(II)-induced ferihydrite transformations are goethite, lepidocrocite, magnetite and green rust. Generally, ferrihydrite transforms to goethite via lepidocrocite, whereas at higher Fe(II) concentrations forms magnetite via goethite and lepidocrocite recrystallization (Benner et al., 2002; Hansel et al., 2003, 2005; Yang et al., 2010; Boland et al., 2014). The coupled and competing pathways are complex and subtle changes in Fe(II) concentrations can yield different transformation products.

For more crystalline phases such as goethite, experimental data demonstrated that uptake of Fe(II) can be a sorption/desorption process and this process does not produce any distinct new phases (Hansel et al., 2005; Latta et al., 2012; Handler et al., 2014). However, Coughlin and Stone (1996) reported the presence of Fe(II) increases the uptake of some divalent cations (e.g., Cu, Ni, and Co) on goethite. Atom exchange interaction between solid Fe(III) and dissolved Fe(II) was illustrated using stable Fe isotopes (Beard et al., 2010; Handler et al., 2014). Usman et al. (2012) noted that high concentrations of Fe(II) promote the formation of green rust; the

likelihood of green rust formation is related to the precursor and follows the order ferrihydrite > goethite > hematite. Microbial reduction of lepidocrocite and other Fe (hydr)oxides may also lead to the formation of green rust and magnetite (Ona-Nguema et al., 2002; Zegeye et al., 2007). It can be concluded that the abiotic transformation of Fe (hydr)oxide is kinetically controlled; however, the mechanisms of Fe(II)-solid phase interactions are still unclear.

1.2.1 Transformation pathways

Iron (hydr)oxide transformations can have a strong impact on the mobility of the associated metal(loid)s. Under oxic conditions, the conversion of ferrihydrite to goethite or hematite may take years to decades or even centuries at ambient temperature (Masue-slowey et al., 2011). However, Fe(II) can catalyze the transformation of ferrihydrite to more crystalline phases within days to weeks (Kocar et al., 2006; Das et al., 2011a). Considering the importance of Fe (hydr)oxides as a control on dissolved metal(loid) concentrations, Fe(II)-catalyzed transformation of Fe (hydr)oxides could have important implications on the fate and transport of metal(loid)s in the environment.

Iron(II) concentrations, pH, time, and associated metal(loid)s influence the rate, degree, and type of the secondary mineral formation. Hansel et al. (2003) observed more than 50% ferrihydrite converted to goethite within 2 h following the addition of 2 mM $FeSO_4$ in batch experiments. Increasing Fe(II) concentration by an order of magnitude did not enhance the transformation extent, though reaction rates increased and different transformation products were observed (Hansel et al., 2005). In general, lower Fe(II) concentrations tend to promote formation of goethite or lepidocrocite, while magnetite formation tends to dominate at higher Fe(II) concentrations (Benner et al., 2002; Hansel et al., 2003, 2005; Zachara et al., 2011). Based on batch experiments, a 1.0 mmolFe(II)/g ferrihydrite threshold for magnetite formation of 0.12 has been proposed (Hansel et al., 2005). Hansel et al. (2003) investigated the effect of Fe(II) concentration by mixing 0 to 4.6 mmol L^{-1} Fe(II) with ferrihydrite-coated sand for 9 days and observed close to a 50% increase in transformation of ferrihydrite to goethite and lepidocrocite with the addition of 0.04 mmol L^{-1} Fe(II) (Fig. 1.2). Ferrihydrite transformation was inhibited at higher Fe(II) concentrations with no additional transformation observed at Fe(II) concentrations greater than 2 mmol L^{-1}. During this experiment, the dominant phase changed from ferrihydrite to a mixture of goethite and lepidocrocite and then to magnetite. Another Fe(II)-bearing mineral,

green rust, also appears as a common transformation product of ferrihydrite and lepidocrocite (Fredrickson et al., 2001; Ona-Nguema et al., 2002; Zachara et al., 2002; Hansel et al., 2003; Usman et al., 2012b; Gomez et al., 2013). As the metastable precursor to magnetite, formation of green rust has been reported under strong reducing conditions where higher Fe(II) concentration is present (Ona-Nguema et al., 2002; Hanna et al., 2013; Wang et al., 2014).

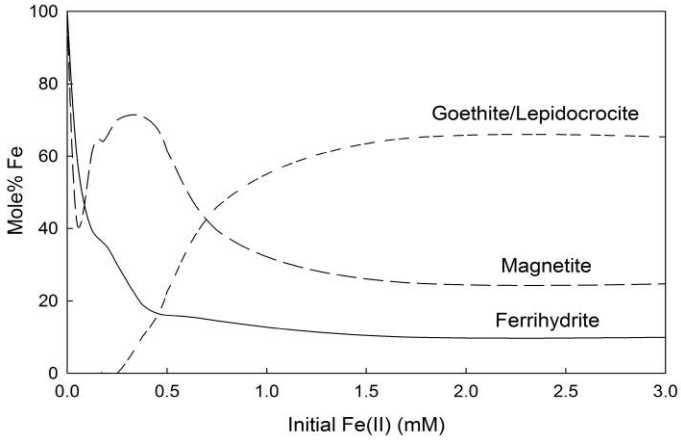

Figure 1.2: Secondary mineralization as a function of initial Fe(II) concentrations. Ferrous chloride (0 to 4.6 mmol/L) was added to 2-line ferrihydrite-coated sand in batch systems for 9 d. Percentages were determined from linear combination fits of k^3-weighted Fe EXAFS spectra (after Hansel et al., 2003).

Apart from the dominant role of Fe(II) concentration, pH and ligand type also influence the composition of ferrihydrite transformation products. Boland et al. (2014) observed that increasing pH (from 6 to 7) favours the formation of goethite relative to lepidocrocite. This observation suggests that lower pH may be conductive to the formation of lepidocrocite and neutral to alkaline environment may accelerate the conversion to goethite (Hansel et al., 2005; Liu et al., 2007). High pH has also been shown to favour magnetite precipitation (Hansel et al., 2005; Boland et al., 2014). The presence of HCO_3^{2-} may impede the formation of magnetite but promote goethite formation regardless of Fe(II) concentrations (Carlson and Schwertmann, 1990; Hansel et al., 2005). Additionally, the presence of SO_4^{2-} tends to promote the formation of goethite while Cl^- enhances the transformation to lepidocrocite (Schwertmann and Cornell, 2000; Hansel et al., 2003, 2005; Liu et al., 2008).

The mechanisms of the competing Fe (hydr)oxide transformations remain an active area of research. Several studies have suggested that these transformations result from either Fe(II)-catalyzed dissolution/re-precipitation or solid state transformation (Cornell et al., 1989; Benner et

al., 2002; Cornell and Schwertmann, 2003; Hansel et al., 2003, 2005; Cudennec and Lecerf, 2005; Liu et al., 2009; Yang et al., 2010; Lu et al., 2011; Latta et al., 2012). Dissolution/re-precipitation is the most widely accepted mechanism for Fe(II)-induced reductive transformation of Fe (hydr)oxides, which involves the dissolution of the mineral precursor, followed by the recrystallization of secondary products (Cornell et al., 1989; Benner et al., 2002; Cornell and Schwertmann, 2003; Hansel et al., 2003; Liu et al., 2009; Yang et al., 2010; Latta et al., 2012). It is proposed that such transformations are initiated by Fe(II) adsorption, followed by an immediate oxidation with an electron transferred to solid Fe(III) atoms (electron hopping) (Yang et al., 2010; Masue-slowey et al., 2011; Frierdich and Catalano, 2012; Boland et al., 2014). The amount of Fe(II) adsorbed and the transport rate of Fe(II) from solution to solid surface appear to dictate the type and precipitation rate of secondary minerals. Solid state transformation was proposed when transformation was observed under unfavorable conditions for the precursor to dissolve (Cornell et al., 1989). This mechanism requires a structural relationship between the transformation percursor and the end product (Jolivet et al., 1992; Cornell and Schwertmann, 2003; Cudennec and Lecerf, 2005; Liu et al., 2005; Lu et al., 2011; Usman et al., 2012b). Such solid state conversion can reduce reaction energies and is kinetically favored (Liu et al., 2009; Lu et al., 2011).

1.2.2 Metal(loid) re-partitioning during reductive transformation

Reductive transformation of ferrihydrite or goethite may impact the mobility of sorbed metal(loid)s. The potential to release or retain these elements is based on their affinity for transformation products and the associated changes in their aqueous speciation. The reductive dissolution of Fe (hydr)oxides is widely accepted to be a key driver of As pollution in Southeast Asia (Smith et al., 2000; Kocar et al., 2006; Tufano and Fendorf, 2008; Tufano et al., 2008; Fendorf et al., 2010; Das et al., 2011b; Wang et al., 2014). Many studies have, therefore, investigated the behaviour of As associated with Fe (hydr)oxides under reducing conditions (Herbel and Fendorf, 2006; Kocar et al., 2006; Paktunc, 2013; Wang et al., 2014). Herbel and Fendorf (2006) reported that As desorption and transport is greatest at the onset of the transition from oxic to anoxic conditions, but that desorption is supressed with elevated Fe(II) concentrations. Compared with As(V), As(III) is more readily released from ferrihydrite in the presence of dissolved Fe(II) (Kocar et al., 2006). Wang et al. (2014) observed that As(III) forms

surface complexes on magnetite while As(V) is incorporated into the mineral structure. Moreover, reducing conditions generated by Fe(II) are not conductive to As(V) reduction to As(III) (Kocar et al., 2006; Amstaetter et al., 2010). X-ray absorption near edge spectroscopy (XANES) has, however, showed that As(III) can be oxidized to As(V) in the Fe(II)-goethite systems (Amstaetter et al., 2010). Past studies have also suggested As (III) oxidation may occur at the ferrihydrite surfaces (Greenleaf et al., 2003; Zhao et al., 2011).

Little is known about the behaviour of other associated metal(loid)s during Fe(II)-induced Fe (hydr)oxides transformations. Reduction of U(VI) during Fe(II)-catalyzed transformations of ferrihydrite has previously been reported (Boland et al., 2011). Additionally, batch experiments have demonstrated that similar to As, the adsorption of Mo and Ni by ferrihydrite can retard transformation rates (Gomez et al., 2013; Wang et al., 2014). Gomez et al. (2013) also found that Mo release from ferrihydrite under static conditions decreases with increasing Fe(II) concentrations; however, the reason for the difference remains unknown. Moreover, coordination environment changes of Mo was observed during ferrihydrite transformation into hematite at elevated temperature, suggesting Mo structural incorporation (Brinza et al., 2015; Das et al., 2016). Information on the behaviour of Mo during Fe(II)-induced Fe (hydr)oxide transformations is currently insufficient to predict Mo mobility in soils, sediments, aquifers, and in mining environments.

1.3 Research hypothesis and objectives

This research examined the impact of Fe(II)-induced transformation of Fe (hydr)oxides on Mo mobility under dynamic flow conditions. More specifically, this research tested the hypothesis that reductive transformation of Fe (hydr)oxides will lead to Mo re-partitioning without a substantial increase in Mo mobility. The following objectives were pursued in testing this hypothesis:

(i) To characterize mechanisms of Mo attenuation by Fe (hydr)oxides under advective flow conditions;
(ii) To examine implications of Fe(II) induced transformation of Fe (hydr)oxides on Mo mobility; and
(iii) To assess the influence of Fe(II) concentration on Fe (hydr)oxide transformation pathways and Mo re-partitioning.

Chapter 2 Materials and Methods

Previous research on Mo sorption has been limited to batch systems, which are characterized by static conditions and changing concentrations with time. These conditions poorly represent most subsurface environments, where groundwater movement can influence reaction rates and pathways. This study examined MoO_4^{2-} adsorption behaviour on ferrihydrite, goethite, and hematite in column flow systems and, thereafter, evaluated Mo re-partitioning during Fe(II)-induced transformation of ferrihydrite and goethite. Sorption of Mo onto silica sand coated with ferrihydrite, goethite, or hematite was performed at circumneutral pH under advective flow conditions. Iron-coated sand has been widely used to examine biogeochemical processes in simulated subsurface environments (Benner et al., 2002; Gupta et al., 2005; Xu and Axe, 2005; Kocar et al., 2006; Hsu et al., 2008; Hwang and Lenhart, 2010; Sergent et al., 2011; Hanna et al., 2013). A pH of 6.5 was chosen to represent the circumneutral mine drainage, which often encounter elevated Mo concentrations (e.g. Conlan et al., 2012; Skierszkan et al., 2016). Iron(II) was subsequently introduced to promote abiotic reductive transformation of theses Fe (hydr)oxides. The two Fe(II) concentrations used in these experiments (0.2 and 2.0 mM) were consistent with the methods employed in the experiments of Hansel et al. (2005) and Masue-slowey et al. (2011). Aqueous and solid-phase analyses were conducted to examine the relationship between Mo re-partitioning and Fe (hydr)oxide transformations. The detailed experimental and analytical methods are provided below.

2.1 Preparation of iron-coated sand

Ferrihydrite, goethite, and hematite were synthesized according to previously-established methods (Schwertmann and Cornell, 2000). Suspensions of these phases were combined with silica sand (20–40 mesh Ottawa Sand, Anachemia), which was first acid-washed in 20% HCl for 48 h, rinsed with DI water, and dried at 110 ℃ for 24 h. The acid washed sand (AWS) and Fe (hydr)oxide mixtures were then shaken at 200 rpm for 48 h to facilitate coating. The Fe content

of the coated sand was determined by inductively coupled plasma-optical emission spectroscopy (ICP-OES) following dissolution of 2 g Fe-coated sand in 8 mL concentrated HCl (OmniTrace, EMD Millipore). Raman spectroscopy and powder X-ray diffraction (XRD) and were performed to confirm the mineralogy and purity of the synthesized Fe (hydr)oxides. Details of the synthesis methods are described below.

2.1.1 Ferrihydrite

Ferrihydrite was synthesized by titrating 500 mL 0.2 M $FeCl_3$ solution with 330 mL 1 N KOH to a pH of 7.5 (Schwertmann and Cornell, 2000). The final 30 mL KOH solution was added dropwise while continually stirred until the solution pH maintained stable at 7.5. The ferrihydrite suspension was then rinsed with DI water and centrifuged three times to reduce ionic strength. The remaining suspension – approximately 400 mL – was transferred into a 1 L glass media bottle (acid-washed), combined with 250 g clean sand, and shook for 24 h. The resulting ferrihydrite-coated sand (FCS) was then rinsed with DI water until the rinse water remained visibly clear. Excess rinse water was removed via vacuum filtration and the FCS was frozen and freeze dried for 24 h to inhibit recrystallization. Freeze drying liberated some loosely-coated ferrihydrite; therefore, the FCS was again rinsed, vacuum filtered, and freeze dried prior to use in the experiments.

2.1.2 Goethite

Goethite was prepared by quickly mixing 90 mL 5 N KOH with 150 mL M $Fe(NO_3)_3 \cdot 9H_2O$ in a molar ratio of 9:5, then diluted with 860 mL DI water (Schwertmann and Cornell, 2000). After that, the 1 L suspension was stirred and heated on a stirring hotplate for 1 h before being transferred to an oven and heated at 60 °C for 60 h. The red-brown ferrihydrite (the initial precipitate) gradually transformed to yellow goethite during heating and condensed well to the bottom. Approximately 4.45 g goethite was produced. The pH of the goethite suspension was around 13, which is not favorable for coating and also contains other ions such as K^+ and NO_3^-. Therefore, the supernatant was decanted and added with concentrated HCl to adjust the pH to neutral. The goethite suspension was then centrifuged and re-suspended three times to remove excess ions. The neutralized suspension was added with 200 g clean sand and shook for 48 h. The goethite-coated sand (GCS) was rinsed with copious DI water until the water was clear and freeze dried.

2.1.3 Hematite

Hematite was synthesized from forced hydrolysis of Fe(III) under acidic conditions (Schwertmann and Cornell, 2000; Hwang et al., 2007). The acidic solution (1 L 0.002 M HCl) was preheated in the oven at 98 ℃ before being added with freshly weighed 5.6 g $FeCl_3 \cdot 6H_2O$ Then the suspension was stirred and moved back to the oven and heated at 98 °C for 3 more days. During the heating, the color of the suspension changed from orange-brown to bright red. Maintaining the temperature to be greater than 90 °C is critical for hematite formation. The pH of the solution was highly acidic (pH < 2), which is not favorable for coating. Therefore, the resulting suspension was added with a few drops of 1 N KOH to bring pH up to around 6 and washed with DI water (supernatant decanted). After centrifugation, around 130 g silica sand was added to the hematite suspension. The mixture was then shook on the platform shaker for 48 h, after which the hematite-coated sand (HCS) was rinsed by DI water and air-dried.

2.2 Column experiments

2.2.1 Column setup

The amount of Fe coated on the FCS (~2600 mg Fe/kg) was slightly lower than that of on the GCS (~3200 mg Fe/kg), but more than double that of on the HCS (~1150 mg Fe/kg). These results are in the range of values in the literature (Schwertmann and Cornell, 2000; Benner et al., 2002; Hansel et al., 2003; Hwang et al., 2007; Hanna et al., 2013). Each type of sand (HCS, GCS and FCS) was dry packed into glass columns (Chromaflex) in triplicate to study MoO_4^{2-} mobility during sorption and reductive transformation. The columns measured 30 cm long with a 4.8 cm internal diameter and a total volume of 543 mL. The columns were packed with approximately 23 cm Fe-coated sand between 3 to 4 cm layers of AWS at the ends (Table 2.1). The total weight of sand in each column was approximately 900 g, with 700 g Fe-coated sand and 200 g of AWS. Column inlets were connected with polyfluorotetraethylene (PTFE) tubing to a low-flow multi-channel persistaltic cassette pump (205CA, Watson-Marlow, USA), which was used to pump approximately 245 mL d^{-1} input solution through the columns. The outlets were connected with PTFE tubing to a 100 mL amber glass flow-through cell to facilitate column effluent sample collection (Fig. 2.1). Overflow from the flow-through cells subsequently flowed into a 1 L bottle and the flow volumes were monitored gravimetrically over time. These columns and all tubing were wrapped with aluminum foil to exclude light.

Table 2.1: Composition of column solids.

Intervals (cm)	Estimated Mass (g)	Notes
0 - 3	94	Acid-washed sand
3 - 5	64	Fe-coated sand
5 - 7	64	
7 - 9	64	
9 - 11	64	
11 - 13	64	
13 - 15	64	
15 - 17	64	
17 - 19	64	
19 - 21	64	
21 - 23	64	
23 - 26	64	
26 - 30	115	Acid-washed sand

Table 2.2: Experiment stages and composition of input solution.

Reagent	Concentration (mM)			
	Saturation	Phase I: Sorption	Phase II: Reduction - low Fe(II)	Phase II: Reduction - high Fe(II)
$CaCl_2 \cdot 2H_2O$	1.2	1.2	1.2	1.2
Na_2SO_4	2.1	2.1	1.9	0.9
K_2SO_4	1.7	1.7	1.7	0.9
$MgSO_4 \cdot 7H_2O$	0.4	0.4	0.4	0.4
KCl	0.5	0.5	0.5	2.1
NaCl	2.5	2.5	3.8	5.8
$NaHCO_3$	2.1	2.1	2.1	2.1
NaBr	/	0.8	/	/
$NaMoO_4 \cdot 2H_2O$	/	0.1	/	/
$FeSO_4 \cdot 7H_2O$	/	/	0.2	2.0

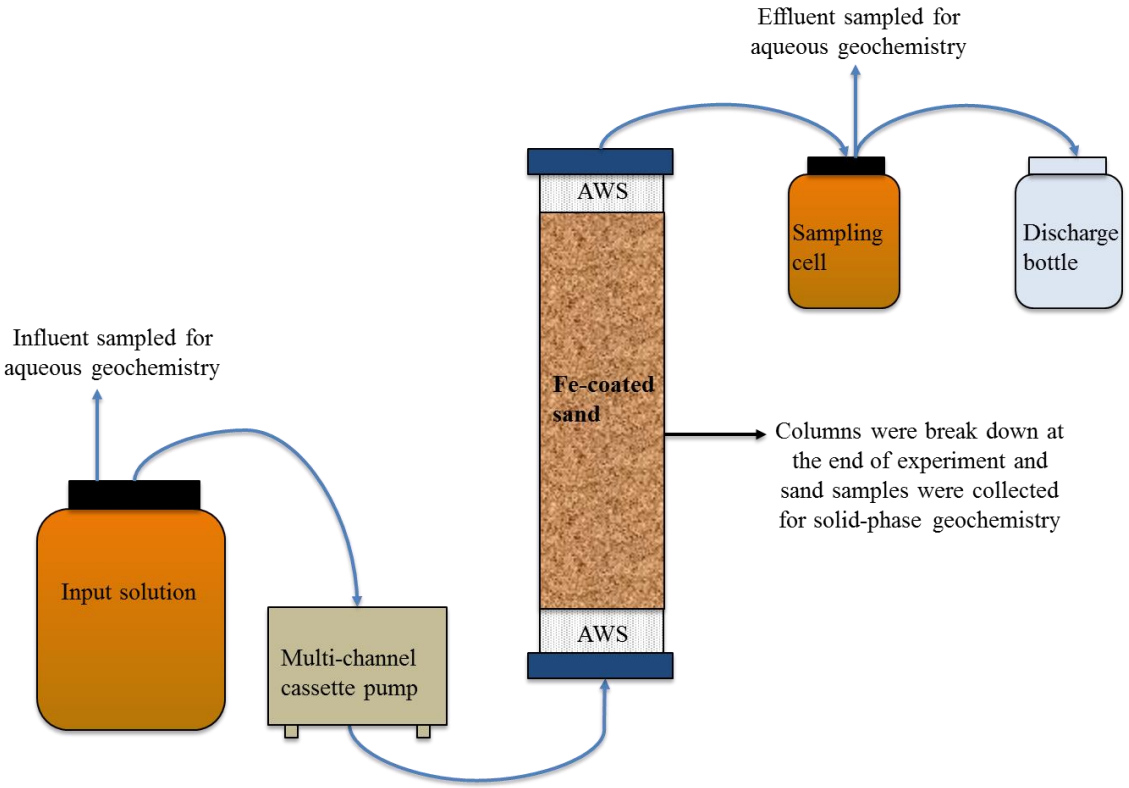

Figure 2.1: The schematic diagram of column experiment (only one column is depicted). The input bottles and columns are wrapped with aluminum foils throughout the experiment. Column output is collected from the sampling cell. Overflow from the sampling cell goes to the discharge bottle, and flow rate is tracked here. The groundwater flow direction is input solution → pump → column → sampling cell → discharge bottle.

The columns were flushed with carbon dioxide (CO_2) gas for 24 hours before initial saturation with Mo-free artificial groundwater. This solution was prepared with DI water and contained 1.2 mM $CaCl_2 \cdot 2H_2O$, 2.1 mM Na_2SO_4, 1.7 mM K_2SO_4, 0.4 mM $MgSO_4 \cdot 7H_2O$, 0.5 mM KCl, 2.5 mM NaCl, 2.1 mM $NaHCO_3$ (Table 2.2). The pH of this and all other input solutions was adjusted to 6.5 in the presence of 10 mM PIPES buffer, which has minimal impact on metal sorption (Szecsody et al., 1994). Column pore volumes were estimated gravimetrically as the difference between the unsaturated and saturated column masses.

2.2.2 Sorption experiment (Phase I)

Column experiments were conducted at room temperature (23 ± 2°C) with adsorption experiment kept under oxic conditions (Eh: 440 ± 30mV). Three control columns (KQ-1, KQ-4 and KQ-7, Table 2.3) were performed for adsorption only (the preliminary test) to estimate Mo transport, breakthrough, and solid-phase distribution. The adsorption process lasted for 35, 21,

and 48 days for control columns KQ-1(GCS), KQ-4(HCS), and KQ-7(FCS), respectively. Molybdate sorption in the HCS column was limited compared to the FCS and GCS columns; therefore, HCS columns were exluded from subsequent experiments. Two columns of each type (GCS: KQ-2 & KQ-3, FCS: KQ-8 & KQ-9) finished Mo breakthrough before being examined for abiotic reduction at different Fe(II) levels.

Following saturation with Mo-free simulated groundwater, the input solution was switched to Mo-bearing (0.1 mM) Phase I solution and the column-sorption experiment was initiated. This concentration of Mo was chosen to mimic those operative in mining and mill drainage while avoiding the formation of Mo polymers. Sodium bromide (NaBr) was used as a non-reactive tracer to evaluate column transport properties. For the conservative tracer experiment, the effluent was sampled at 2 to 4 h intervals over three days. Aqueous geochemistry sampling was performed two to three times a week during the adsorption phase. Due to different adsorption capacities, GCS columns showed Mo breakthrough ahead of FCS columns, however, they were maintained under the same condition as FCS columns until reduction. The sorption experiment lasted for 101.73 and 102.61 days for the GCS (KQ-2, KQ-3) and FCS (KQ-8, KQ-9) columns, respectively.

Table 2.3: Column ID and experimental stages.

Column ID	Content	Phase I: Saturation	Phase II: Sorption	Phase III: Reduction - low Fe(II)	Phase III: Reduction - high Fe(II)	Column comment
KQ-1	GCS	√	√			control
KQ-2	GCS	√	√	√		reduction
KQ-3	GCS	√	√		√	reduction
KQ-4	HCS	√	√			control
KQ-7	FCS	√	√*			control
KQ-8	FCS	√	√	√		reduction
KQ-9	FCS	√	√		√	reduction

2.2.3 Reductive transformation experiment (Phase II)

Following complete Mo breakthrough, the GCS (KQ-2, KQ-3) and FCS (KQ-8, KQ-9) columns were transferred to a glove box (Coy Laboratory Products) with an anoxic atmosphere (< 5 vol. % H_2, balance N_2). Two input solutions with different Fe(II) concentrations (i.e., 0.2 mM and 2.0 mM) were prepared by dissolving pre-determined amounts of $FeSO_4 \cdot 7H_2O$ (Sigma-

Aldrich) in the Phase II input solution that was first bubbled in the glove box with high purity N_2 for at least 24 h. Oxygen removal was evident from measured Eh values, which decreased to -280 ± 50mV. Temperature and influent pH were maintained the same as in Phase I of the experiment (i.e., Mo sorption). However, to avoid increasing SO_4^{2-} concentration with $FeSO_4 \cdot 7H_2O$ addition, the amount of other ions were adjusted accordingly, leaving Cl^- as the only increase as it is conservative (Table 2.2). Water samples were collected and monitored in the glove box daily for the first week and then every second day until the conclusion of the experiment. The column experiments ended when effluent Mo concentrations reached a pseudo steady state. Consequently, reduction lasted 54.6 days for the high Fe columns (KQ-3, KQ-9) and 55.6 days for low Fe columns (KQ-2, KQ-8).

2.2.4 Water sampling and analysis

The input solutions and column effluents were sampled and analyzed as a function of time. Water samples were collected using sterile polyethylene syringes (Norm-Ject®, Henke-Sass, Wolf GmbH, Germany). Measurements of pH, Eh, and electrical conductivity (EC) were performed immediately on unfiltered samples. The pH meter (Orion 8156 Ross Ultra) was calibrated by pH 4, 7, and 10 buffers, and checked against the pH 7 buffer before each measurement. Redox potential was measured using a combination platinum redox electrode (Orion 9678) with Ag/AgCl filling solution (Orion 900011). Zobell's and Light's solutions (Ricca Chemical) were used to test the performance of the redox electrode (Thermo Scientific). The conductivity (Orion 011050) was monitored with 1413 μS/cm standard (Orion 011007). Alkalinity was measured by titrating a known volume of filtered (0.2 μm PES membrane) sample with standardized sulfuric acid (Hach), which had been added with bromocresol green-methyl red indicator (Ricca Chemical, endpoint pH 4.5). The filtered water samples (0.2 μm PES membrane, both acidified and non-acidified) were refrigerated (4 ℃) for aqueous composition analysis. The non-acidified ones were used for concentrations of inorganic anions by ion chromatography (IC). Water samples for major cations and trace elements were preserved by concentrated HNO_3 to a pH less than 2. Inductively coupled plasma-optical emission spectroscopy (ICP-OES) was employed to determine the concentrations of major cations such as Fe_{tot}, Mo_{tot} and Ca_{tot}. Transport parameter was estimated by Br tracer, which was measured using electrode (Orion 9635) with samples pre-added with ionic strength adjustor (ISA: Orion 940011). Column

dispersivity was evaluated by fitting Br breakthrough in CXTFIT/Excel (Tang et al., 2010). The aqueous concentration of Fe(II) during reduction was analyzed by the spectrophotometry (Ferrozine) while Fe_{tot} was determined by ICP-OES (Gibbs, 1979). Column influent and effluent were preserved by concentrated HCl and diluted to the range of Fe standards (100 to 1000 ppb). Base on the data analyzed by IC and ICP-OES, the aqueous composition was modelled by PHREEQC with a modified version of the WATEQ4F database containing additional Mo phases (Parkhurst, 1995). Total amount of Mo retained and released was calculated by integrating the concentration differences and the flow rate over time using the equation:

Mo retained or released = (influent [Mo]-effluent [Mo])*time elapsed*flow rate …….(2.1)

Note that a PV of Mo-bearing input solution was flushed out of the columns at the beginning of reduction, therefore, that amount of flushed Mo was not taken into account.

2.2.5 Solid-phase sampling and analysis

Prior to the deconstructive sampling, flow was terminated and columns were drained out overnight by turning the columns upside-down to maintain consistent flow direction. The sand in the columns was then collected in 50 mL centrifuge tubes at 2 cm intervals along the column length. Control samples (KQ-1, KQ-4 and KQ-7) were air dried, while the reduction columns were flash frozen, freeze dried and stored in a desiccator under an anoxic atmosphere until analysis. Solid-phase Mo, Fe and S content was determined at 6 or 7 intervals in each column by digesting 2 g of Fe-coated sand in concentrated HCl followed by ICP-OES analysis.

2.2.5.1 X-ray diffraction

X-ray diffraction (XRD), electron microprobe analysis (EMPA) and micro-Raman spectroscopy (RS) were performed to verify the purity of synthesized Fe (hydr)oxides and to examine mineralogical transformations. As a conventional technique, XRD has the advantage to easily identify materials using thousands of known standards. The present study used XRD to investigate Fe phases that were collected after sand coating. Ground hematite, goethite and ferrihydrite powders were mounted onto glass holders with a drop of methanol and allowed to dry before analysis. The XRD scans were measured using a PANalytical Empyrean diffractometer at the department of Geological Sciences, University of Saskatchewan. The diffractometer was equipped with a Co Kα radiation source set to 40 kV and 45 mA over a range in 2θ from 10 to 90° (2°/min). The raw XRD data were analyzed using Highscore Plus

Panalytical software using the Inorganic Crystal Structure Database (ICSD) (Bergerhoff et al., 1983) (Fig. 2.2). Synchrotron-based high energy powder X-ray diffraction (PXRD) was also used to characterize the synthesized Fe (hydr)oxides and corresponding Fe-coated sand samples. Ground samples and the LaB_6 standard were loaded into kapton capillaries and 2D PXRD patterns were collected at beamline CMCF-BM (Canadian Light Source, CLS) with a wavelength of 0.68878A. The 2D diffraction patterns were then calibrated and converted to 1D patterns using GSAS-II (Toby and Von Dreele, 2013). Phase identification was then conducted using Match software and its database. The crystallinity can be reflected by the peak sharpness (Hayes et al., 2014). The hematite diffraction pattern demonstrated a good fit with the dataset of hematite in ICSD: 98-010-8081, the sharp and intensive peaks at 2θ of ~39°, 42°, and 64° were consistent with published values (Schwertmann and Cornell, 2000; Das and Hendry, 2011). The characteristic broad peaks at 40° and 73° indicate the purity of two-line ferrihydrite, which was consistent with published values (Schwertmann and Cornell, 2000; Das and Hendry, 2011). The XRD pattern of goethite was confirmed by ICSD: 98-006-1693 and the peak positions at ~21°, 26°, and 43° were in good agreement with that presented in the literature (Carlson and Schwertmann, 1990; Hansen et al., 1994; Schwertmann and Cornell, 2000; Das and Hendry, 2011). However, the goethite pattern also displayed an amorphous background which matches the ferrihydrite broad peaks, suggesting the presence of ferrihydrite impurity. This result can be explained by the synthesis method of goethite via aging and heating ferrihydrite under an alkaline condition. Though the corresponding coated sand was also checked with XRD and PXRD, diffraction patterns failed to show the expected peaks of Fe minerals (see Appendix). The difficulty in identifying the Fe coating is because the amount of Fe is below the detection limits (1-5wt%) (Sergent et al., 2011; Gomez et al., 2013; Hanna et al., 2013). In conclusion, XRD technique verified the synthesized Fe (hydr)oxides are hematite, goethite, and 2-line ferrihydrite.

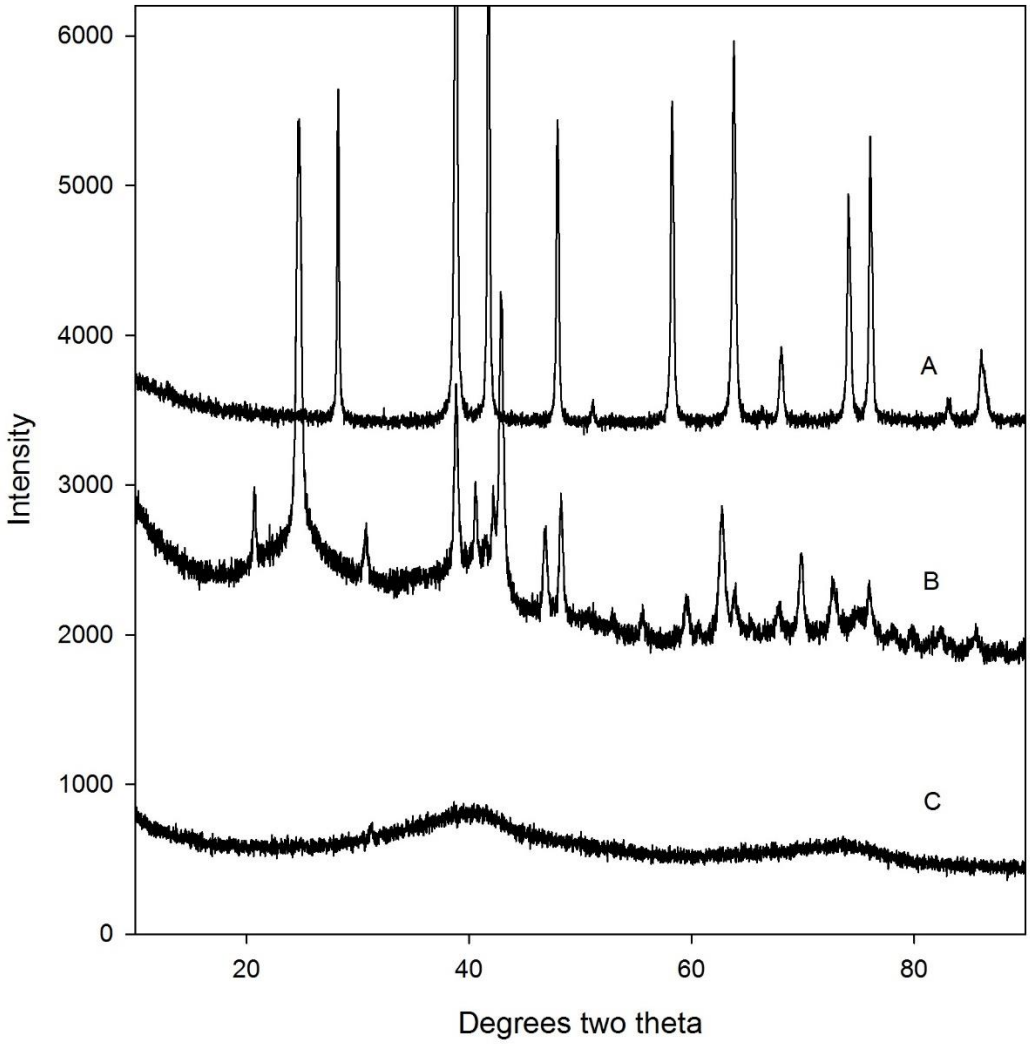

Figure 2.2: XRD patterns of synthesized Fe (hydr)oxides: (A) hematite; (B) goethite; (C) 2-line ferrihydrite.

2.2.5.2 Raman spectroscopy

Raman spectroscopy was performed on synthesized Fe (hydro)xides and the Fe-coated sands. The Fe minerals were ground while sand samples were directly mounted onto a glass slide wrapped with metal foil. Measurements were made using Renishaw InVia Raman microscope (Saskatchewan Structural Sciences Centre, University of Saskatchewan) with a solid state laser diode operating at 785 nm Lens and a 1200 l/mm (633/780) grating. A laser power of 0.1% was chosen for all samples to minimize any laser-induced transformation and fluorescence. The instrumental silicon calibration standard was measured at 520 cm^{-1} each time before use. Extended scans (100-1200 cm^{-1}) were collected using the 50x objective (to reduce noise ratio) for

30 accumulations. The Fe (hydro)xide references were synthesized during sand coating, expect for magnetite and $FeMoO_4$ (Sigma-Aldrich). Samples of Fe-coated sand, control columns and reduction columns were all examined. Sand samples from the columns were collected from the 5-7cm interval one week after column breakdown. As Fe (hydr)oxides are discretely coated on sand, Raman spectra were collected for the dark spots (Fe (hydr)oxides) under the microscopy.

2.2.5.3 Electron microprobe

Sand samples from the reduction columns were examined by electron microprobe analysis (EMPA, JEOL JXA-8600 Superprobe Analyzer, department of Geological Sciences, University of Saskatchewan) to determine elemental composition of Fe-coated sands and solid-phase column samples. This electron microprobe was equipped with three automated wavelength dispersive spectrometers operating at 15 kV and 25 nA beam current. Samples (5-7 cm interval) from the reduction columns were coated with carbon to increase the conductivity and only shortly exposed to air during the transfer to a vacuum sample chamber. Both backscattered electron (BSE) and energy dispersive spectroscopy (EDS) detectors were used for data collection. The contrasting feature in BSE comes from the atomic number and chemical distribution. For example, sand quartz consists of Si and O, which are of low atomic number and appear gray.

2.2.5.4 Scanning electron microscopy

High-resolution scanning electron images were collected to identify the crystal morphology of Fe phases. Sand samples used for electron microprobe were subsequently coated with gold for analysis by scanning electron microscopy (Hitachi SU8010). Samples were prepared under anoxic conditions then quickly transferred to the vacuum chamber of a FESEM-cold field emission SEM instrument at the Western College of Veterinary Medicine Image Center, University of Saskatchewan. Scanning electron images were obtained under 5000 V accerelating voltage with 40,000x magnification.

2.2.5.5 X-ray absorption spectroscopy

X-ray absorption spectroscopy (XAS) was employed to examine changes in Mo coordination before and after reduction. Molybdenum K-edge X-ray absorption near edge structure (XANES) spectroscopy was performed at the Hard X-ray Micro-Analysis (HXMA) beamline (06-ID-1) at the CLS. Solid-phase samples collected from the 5 - 7 cm interval were selected for XANES analysis. Approximately 200 mg freeze-dried sand was packed into Teflon holders between two

layers of polyimide (Kapton) tape. Spectra were collected from −200 to +200 eV relative to the theoretical adsorption edge for elemental Mo (20,000 eV). Spectra for reference compounds were collected in transmission mode, whereas sample spectra were measured in fluorescence mode using a 32-element Ge detector (Canberra Industries Inc.). Transmission data from a Mo foil (10 μm thick) positioned downstream of the sample was used for internal energy calibration.

Chapter 3 Results

3.1 Column characteristics

Porosity varied from 0.36 to 0.39 among columns and the average bulk density was 1.68 kg L^{-1} (Table 3.1). The flow rate was consistent in all columns (~245 mL d^{-1}) though it slightly increased (less than 2%) in the reduction process. Linear pore-water velocity ranged from 34.8 to 37.5 cm d^{-1} (average 35.6 cm d^{-1}) during the adsorption and reduction phases. Dispersivity was consistently low with values ranging from 0.06 to 0.18 cm (Fig. 3.1). Cumulative volume in each column was around 25.0 L during Mo adsorption, and this value was 13.6 L during Fe(II) reduction.

Table 3.1: Physicochemical characteristics of columns.

Parameters	KQ-1	KQ-2	KQ-3	KQ-7	KQ-8	KQ-9
Total packed sand (g)	905.66	916.29	897.92	913.29	909.90	907.30
Fe-coated sand (g)	702.23	698.85	697.71	702.69	702.49	703.67
Porosity	0.37	0.38	0.39	0.38	0.37	0.36
Bulk Density (kg L^{-1})	1.67	1.69	1.65	1.68	1.68	1.67
Flow rate-adsorption (mL d^{-1})	238.67	240.28	244.39	241.45	244.98	245.17
Flow rate-reduction (mL d^{-1})	/	243.99	245.03	/	247.94	246.14
Adsorption duration (day)	35.11	101.73	101.73	48.23	102.61	102.61
Reduction duration (day)	/	55.61	54.63	/	55.61	54.63
Total volume-adsorption (L)	8.38	24.57	24.92	13.78	25.23	25.16
Total volume-reduction (L)	/	13.73	13.40	/	13.87	13.45
Velocity-adsorption (cm d^{-1})	35.19	34.82	34.79	34.06	36.29	35.52
Velocity-reduction (cm d^{-1})	/	35.37	34.88	/	37.09	37.48
Mo retardation	/	23.2	23.1	/	92.2	90.8
Dispersivity (cm)	0.08	0.12	0.11	0.06	0.18	0.13

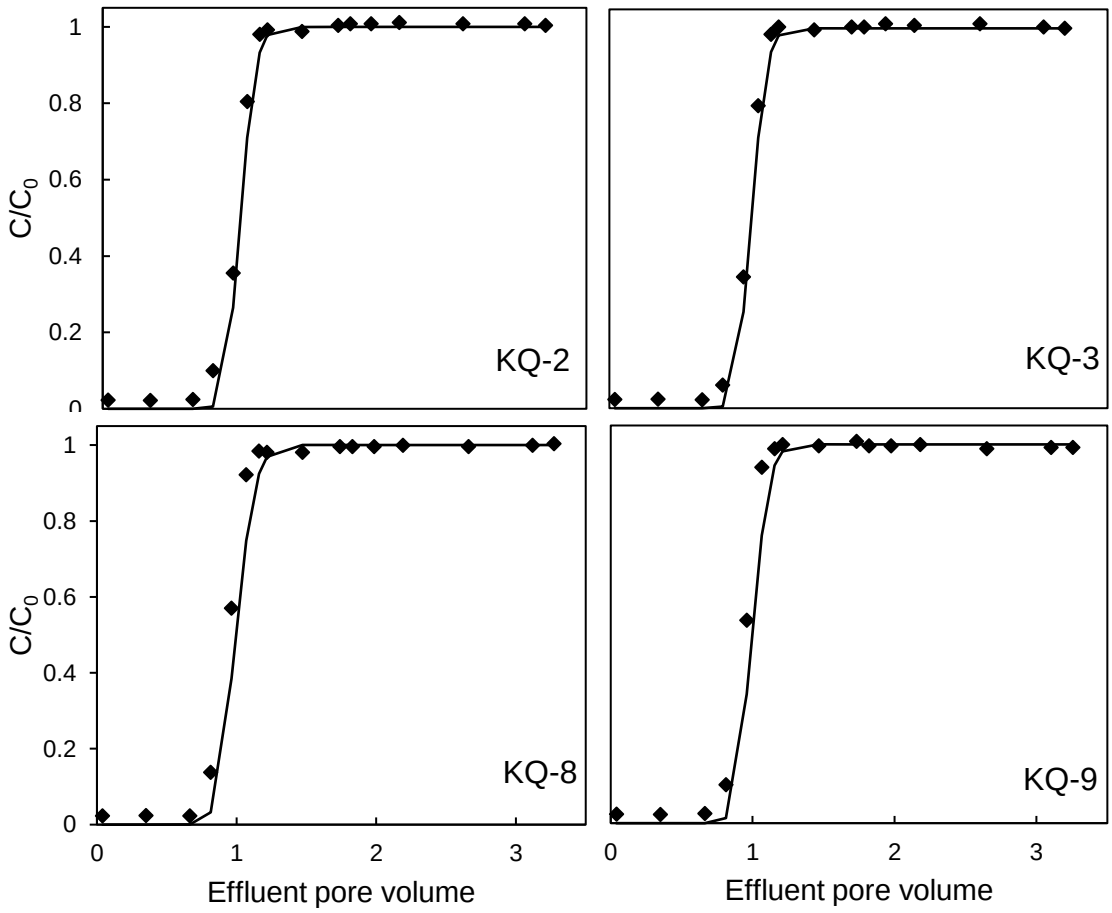

Figure 3.1: Tracer breakthrough curves showing measured (symbols) and modeled (lines) results.

3.2 Aqueous geochemistry

3.2.1 *Phase I: sorption*

The geochemical conditions in the effluent were consistent with the influent expect for the variation in Mo_{tot} concentrations (Fig. 3.2 – 3.5). Effluent pH was consistently circumneutral (average 6.55 ± 0.05) during Mo sorption. Alkalinity averaged 200 ± 10 mg L^{-1} (as $CaCO_3$) and Eh averaged 440 ± 30mV in column influent and effluent. Effluent concentrations of SO_4^{2-} and Cl^- were consistent with input concentrations, which indicates that SO_4^{2-} and Cl^- sorption was limited in all columns. The concentrations of Fe in the influent and effluent were below the detection limit.

Measureable effluent Mo_{tot} was first observed at approximately 15 PV in the goethite columns and at approximately 84 PV in the ferrihydrite columns, with estimated C/C_0 of 0.5 at 23

PV and 91 PV for the goethite and ferrihydrite columns, respectively. Total Mo retained in the ferrihydrite columns was more than three times the amount of that of in the goethite columns (~60 mg) (Table 3.2). Geochemical modeling demonstrated that the input solution (Phase I: Mo adsorption) was near-saturation with respect to powellite [$CaMoO_4$]. The majority of Mo was MoO_4^{2-}, with $NaMoO_4^-$ took up a lesser portion. The relative percentage of these species in the effluent were consistent with those in the input solution. Polymers (e.g., $HMo_7O_{24}^{5-}$) was not formed in the influent and effluent. This result is consistent with the findings in the literature that the Mo concentration (0.1 mM) employed is mainly MoO_4^{2-} monomer (Cruywagen, 2000; Bourikas et al., 2001; Xu et al., 2013).

3.2.2 *Phase II: reduction*

For the low Fe columns (KQ-2 and KQ-8), no appreciable changes in pH and alkalinity were observed during the reduction phase. There was a slight decrease in pH by 0.1 unit at the beginning of the reduction phase which corresponded to a ~10% decrease in alkalinity. In contrast, the differences in pH and alkalinity between column influent and effluent were contrasting for the high Fe columns. Columns KQ-3 and KQ-9 both exhibited approximately abrupt decreases by 0.7 pH and ~60% alkalinity at the onset of reduction. However, the maximum decreases occurred at different times for the two columns: KQ-3 (1 PV) after switching to reduction as compared to KQ-9 (4 PV). The trends after the initial decreases were different as well: effluent pH and alkalinity in KQ-3 increased quickly to the level of the influent in 12 PV; whereas for KQ-9, the whole process took twice the amount of time, and pH and alkalinity concomitantly plateaued for 10 PV before returning to the influent level.

Effluent Mo_{tot} and Fe_{tot} concentrations were substantially different from the column influent. The release of Mo from the low Fe columns was considerably greater than that of the high Fe columns, and the trend in the goethite columns was more continuous than the ferrihydrite columns. Specifically, the concentration of Mo in KQ-2 decreased continuously from 12.7 to less than 0.2 mg L^{-1} within 30 PV, while the decreasing trend in KQ-8 was featured by 10 PV of stable concentration at ~8 mg L^{-1}. In contrast, effluent Mo concentrations in KQ-3 decreased from 13.2 to less than 0.2 mg L^{-1} over the subsequent 10 PV. Effluent Mo in KQ-9 decreased by two steps: it initially plunged to ~1.3 mg L^{-1} in 5 PV, followed by a slow decrease for a period of 15 PV before Mo was minimal (< 0.2 mg L^{-1}). Effluent pH, alkalinity, and Fe concentrations

increased to input values when effluent Mo became minimal. It should be note that the remained 1 PV of input solution in Phase I also contributed to the initial increase of Mo at the onset of reduction. Total amount of Mo released during Phase II demonstrated that increasing Fe(II) concentration can substantially supress Mo mobilization. Compared with the high Fe columns, Mo release was 6 times greater in the low-Fe columns. The Mo released/retained% illustrated that the ferrihydrite columns were able to retain higher percentages of Mo than the goethite columns especially under low Fe conditions. It can be inferred that the ferrihydrite transformation products have a stronger interaction with Mo compared with the goethite transformation products.

The trends in Fe_{tot} concentrations seemed to mirror those of Mo. Effluent Fe in the low Fe columns was undetectable (less than 0.01 mg L^{-1}) until 12 PV and 15 PV in KQ-2 and KQ-8, respectively. Column KQ-2 then experienced a gradual increase until reaching the influent level after 50 PV. However, Fe concentrations in KQ-8 fluculated between 4.5 and 7.5 mg L^{-1} until the conclusion of the experiment. Similar to the trend in pH and alkalinity, Fe concentrations in KQ-3 climbed to the level of the influent in 12 PV, however, KQ-9 took a longer process to reach the input values, which also encampuss a 10 PV plateau at ~60 mg L^{-1}. The similar trends (plateau) indicate a connection between Fe and acid production. Geochemical modeling also suggested that the input solution (Phase II: Fe reduction) was near-saturation with respect to siderite [$FeCO_3$]. The major aqueous component was Fe^{2+}, with the rest being $FeSO_4^0$ and $FeHCO_3^+$. The modeling result is consistent with measurements conducted by spectrophotometry and ICP-OES. The dominant aqueous species, Fe(II), took up more than 98% Fe_{tot} in the column input solution, and 83% and 99% Fe_{tot} in the low Fe and high Fe effluent. The pearson correlation coefficient between Fe(II) and Fe_{tot} concentrations are 0.932 and 0.982 for all datasets in the low Fe and high Fe columns, respectively. As a consequence, Fe_{tot} is referred as Fe(II) hereafter. The trend of SO_4^{2-} concentration in the column effluent varied along with the influent, with no distinct changes in all four columns.

Table 3.2: Elements retained and released (mg).

column ID	Mo retained (Phase I)	Mo released (Phase II)	Mo released/retained%
KQ-2	61.1	-19.0	-31.1
KQ-3	59.5	-2.67	-4.49
KQ-8	197	-34.1	-17.3
KQ-9	191	-5.61	-2.93

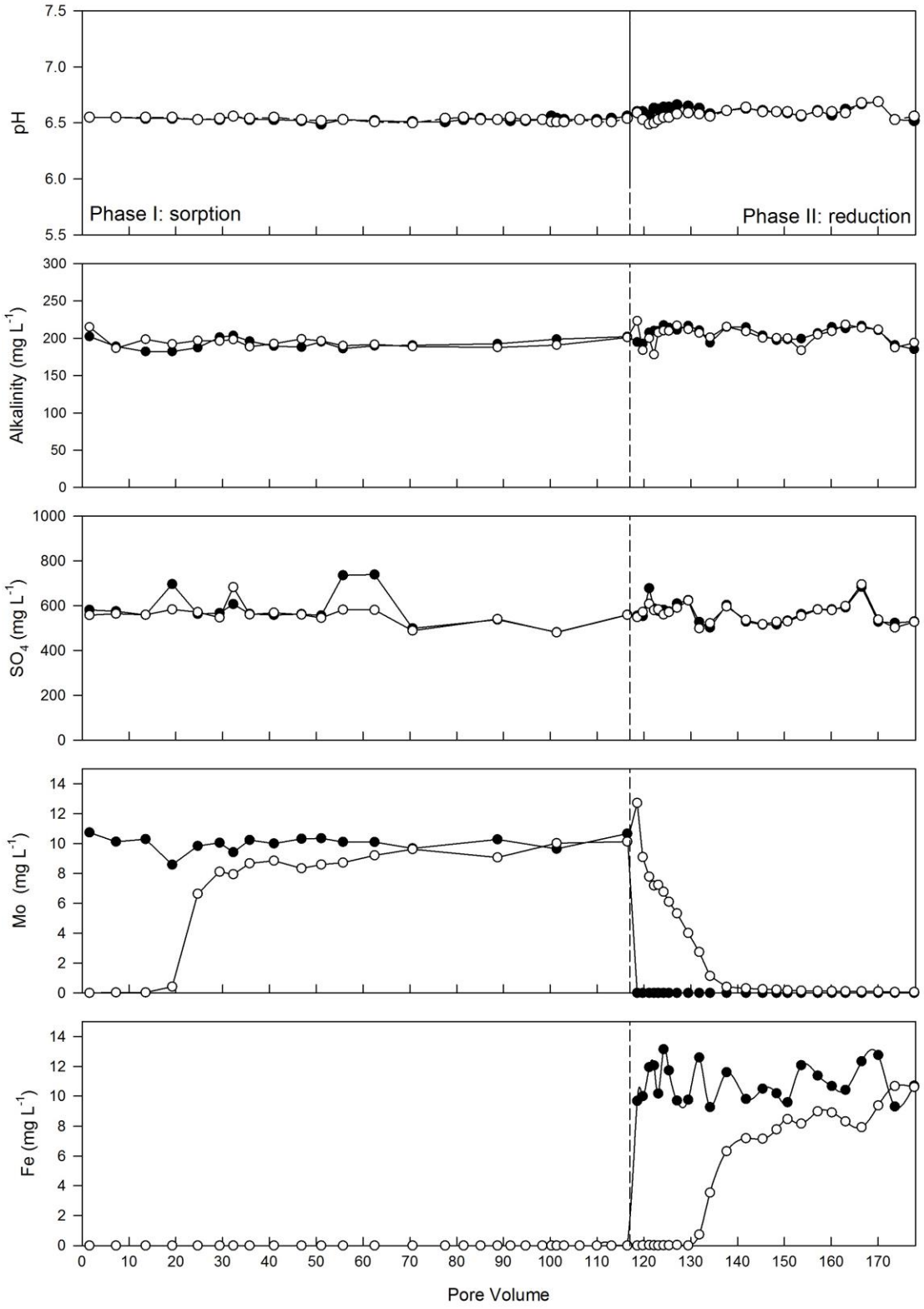

Figure 3.2: Column KQ-2: influent (closed symbols) and effluent (open symbols) concentrations of SO_4^{2-}, Mo, Fe, pH and alkalinity ($CaCO_3$) as a function of pore volume. The dashed vertical line represents the switch from Adsorption (Phase I) to Reduction (Phase II).

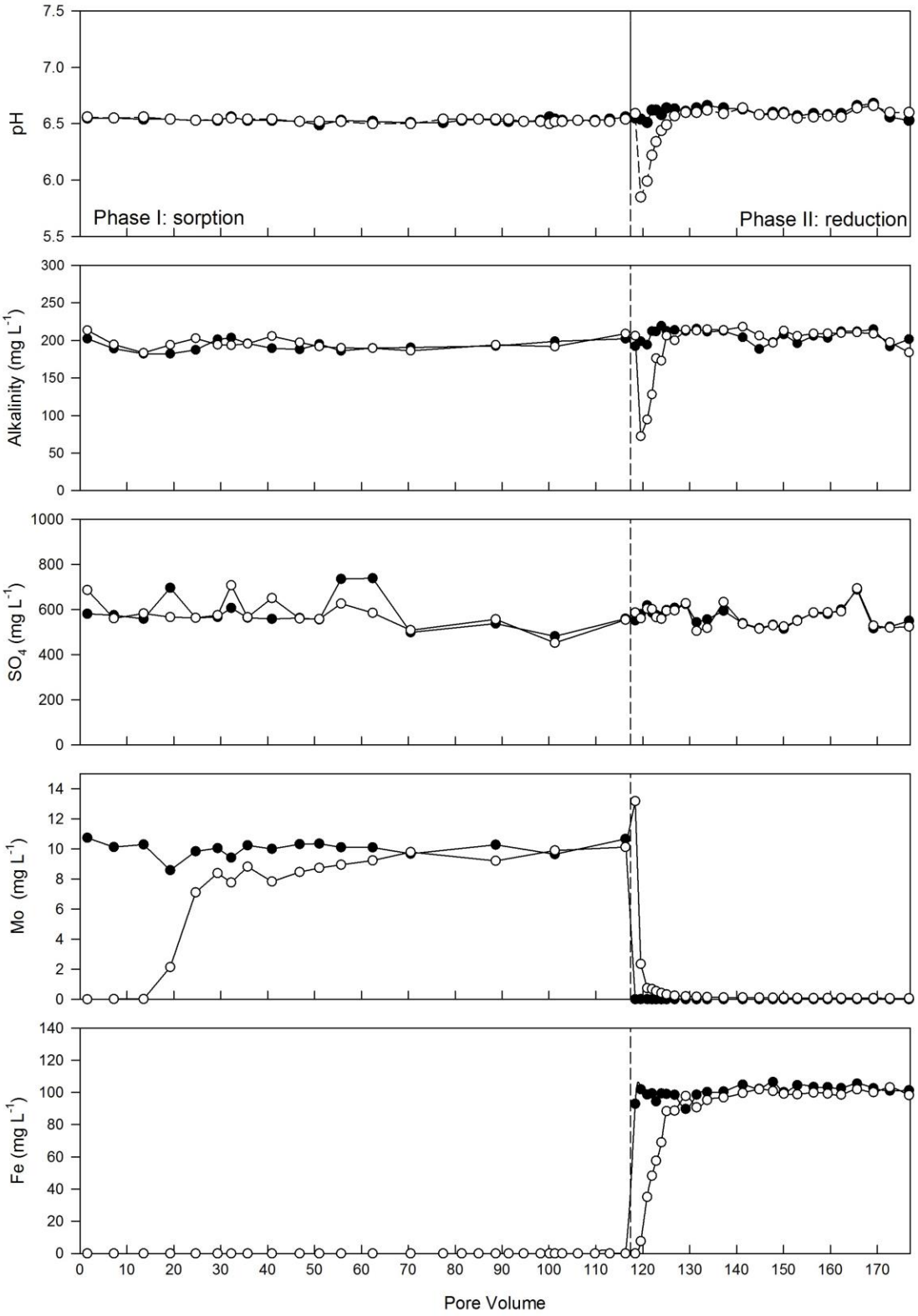

Figure 3.3: Column KQ-3: influent (closed symbols) and effluent (open symbols) concentrations of SO_4^{2-}, Mo, Fe, pH and alkalinity ($CaCO_3$) as a function of pore volume. The dashed vertical line represents the switch from Adsorption (Phase I) to Reduction (Phase II).

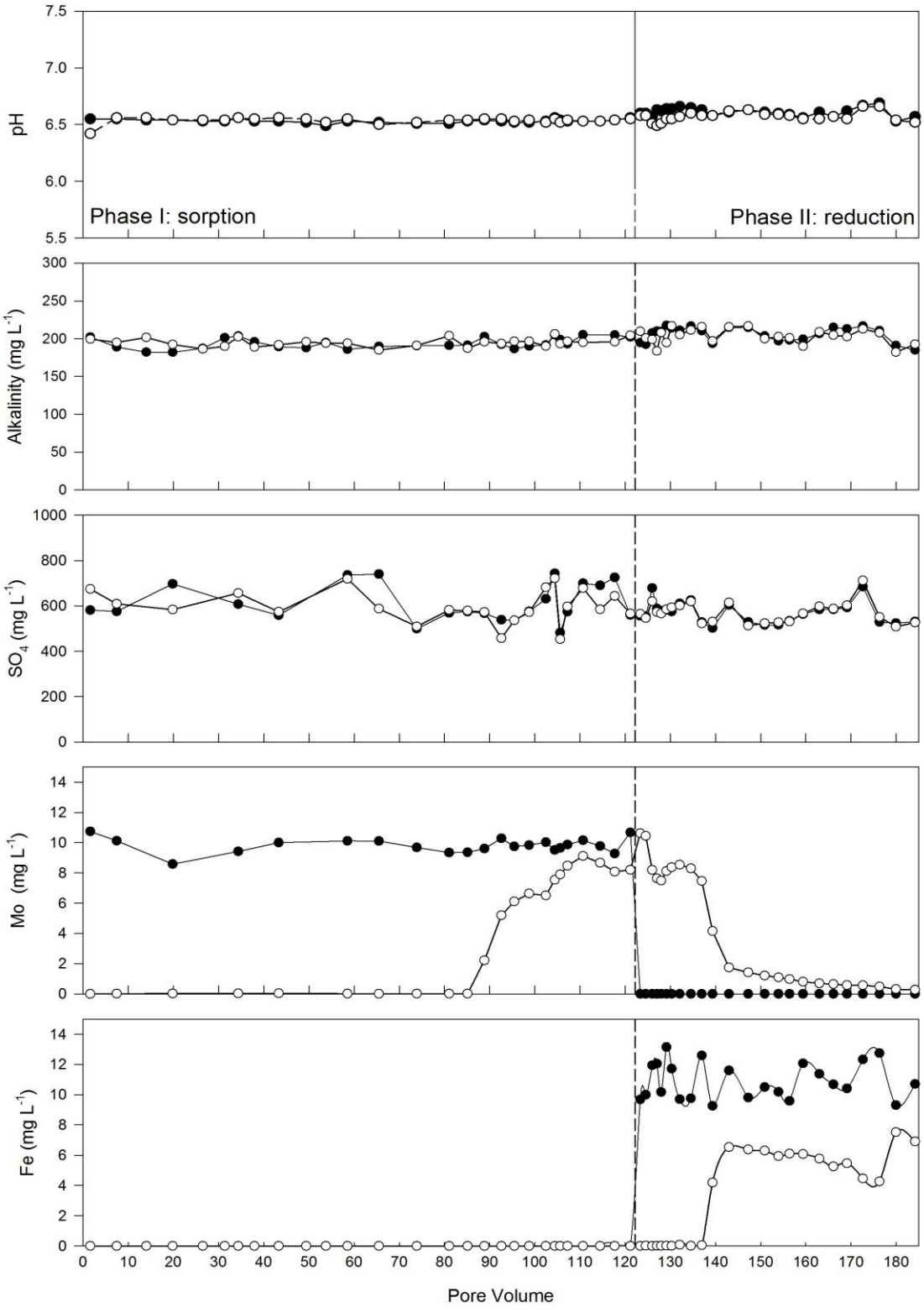

Figure 3.4: Column KQ-8: influent (closed symbols) and effluent (open symbols) concentrations of SO42-, Mo, Fe, pH and alkalinity ($CaCO_3$) as a function of pore volume. The dashed vertical line represents the switch from Adsorption (Phase I) to Reduction (Phase II).

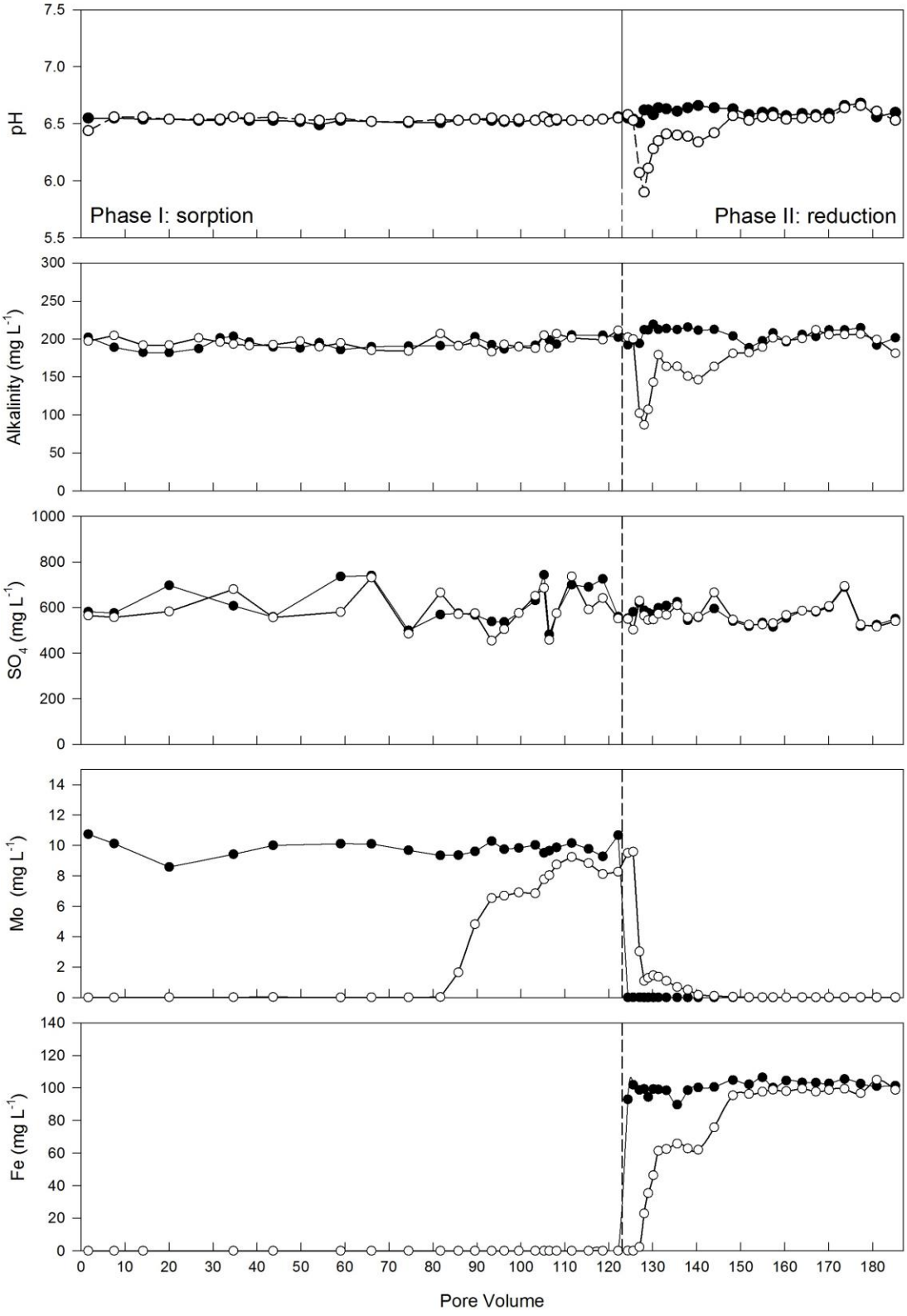

Figure 3.5: Column KQ-9: influent (closed symbols) and effluent (open symbols) concentrations of SO_4^{2-}, Mo, Fe, pH and alkalinity ($CaCO_3$) as a function of pore volume. The dashed vertical line represents the switch from Adsorption (Phase I) to Reduction (Phase II).

3.3 Solid-phase geochemistry

3.3.1 Spatial distribution

Spatial distribution of total Mo, Fe, and S varied among each type of columns (Fig. 3.6). Since the ferrihydrite control column was terminated before Mo breakthrough, solid-phase Mo decreased halfway along the column and only the first three intervals were used for comparison. The mass ratio of Mo/Fe in the control columns followed the order: FCS (0.11) > GCS (0.026) > HCS (0.011). Adsorption capacity of each Fe phases was also evaluated by the mass ratio of Mo/Fe (hydr)oxide, which followed the order: ferrihydrite (as $5Fe_2O_3 \cdot 9H_2O$) (0.061) > goethite (0.016) > hematite (0.0076). In addition, Fe was relatively evenly distributed on each type of sand, with no measurable redistribution. Substnatially less S was associated with the column solids relative to Mo. The S content and distribution was similar for FCS and GCS columns, which exhibited an increasing trend with distance along the columns.

A decrease in Mo content near the column inlets was observed following the reduction phase. The Mo/Fe mass ratio dropped by ~50% to 0.014 over the first 3 - 5 cm interval in KQ-2, while this value only experienced a slight decrease in KQ-3 over this interval. The FCS columns both exhibited decreases in Mo/Fe ratio at the column inlets: KQ-8 declined by ~55% to 0.038 while KQ-9 decreased to 0.094. In general, a greater proportion of sorbed Mo was retained in the high Fe(II) influent columns (KQ-3, KQ-9) and on FCS compared to GCS. A slight increase in solid-phase Fe was observed during the reduction phase. Overall, the introduction of Fe(II) promoted Mo redistribution within the columns; however, the amount of released Mo was supressed by higher Fe(II) concentrations.

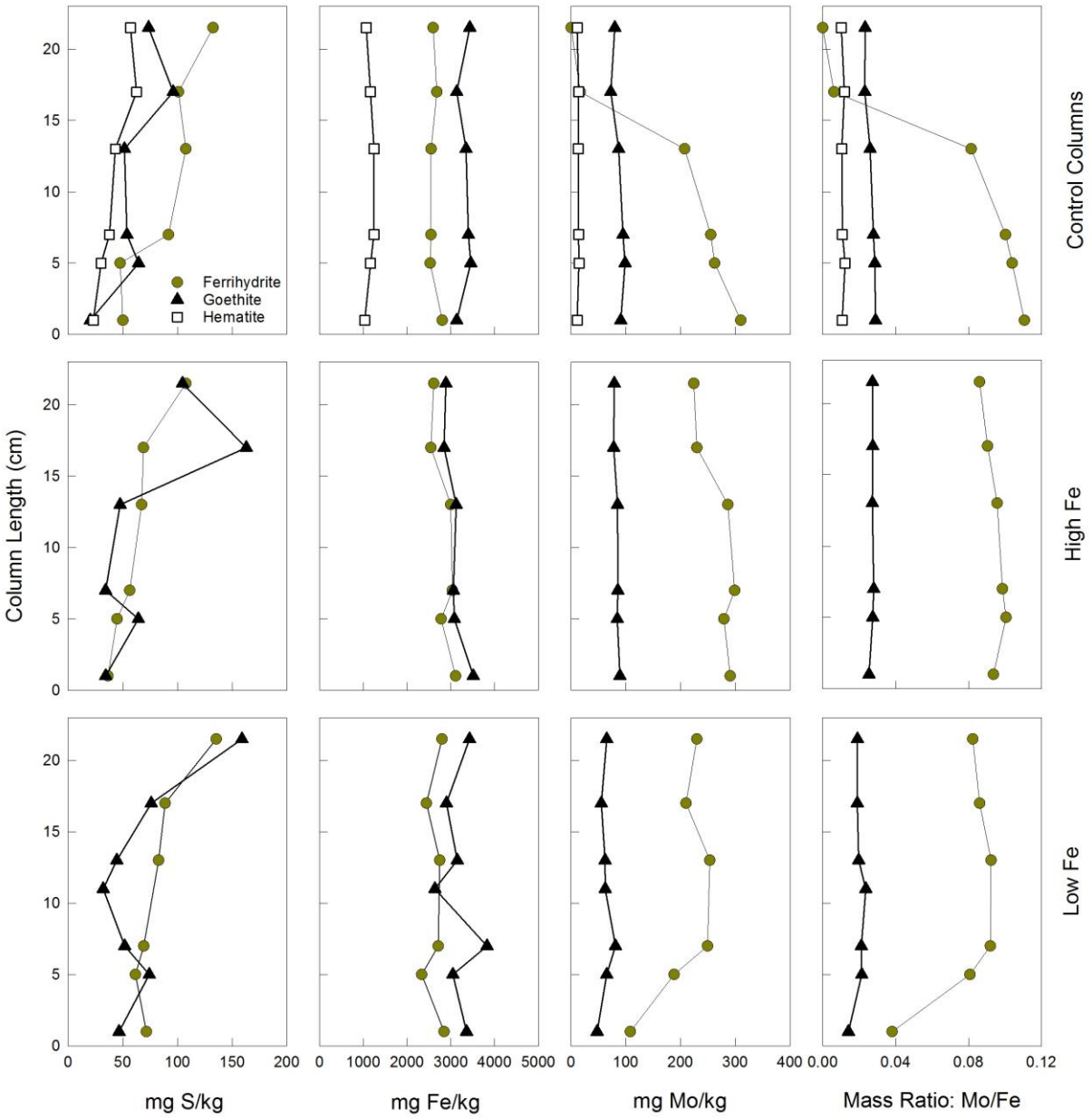

Figure 3.6: Solid-phase concentrations of Mo, Fe, and S (per kg sand) along the column length. Plot symbols: square-hematite, triangle-goethite, circle-ferrihydrite. Control columns: KQ-1, KQ-4, KQ-7; high Fe: KQ-3 and KQ-9; Low Fe: KQ-2 and KQ-8.

3.3.2 Raman spectroscopy

3.3.2.1 Standards

The Fe minerals and sand samples can be identified by the band position and their relative intensities (Fig. 3.7 and Table 3.3). For mixtures, higher intensity of certain bands normally indicates a higher concentration of the corresponding phase. The mineral crystallinity may be

inferred by the broadness of a band: broad bands normally indicate a poorly-crystalline phase, while narrow bands are typical of crystalline phases (Courtin-Nomade et al., 2010; Das and Hendry, 2011). Silica sand spectra exhibited bands at ~124, ~202, ~261, ~352 and ~461 cm^{-1}, with the band at ~461 cm^{-1} being the strongest. These values are in good agreement with previous results of α-quartz, with bands at ~128, ~205, ~464 cm^{-1} (Mernagh and Liu, 1997). Raman spectra of $FeMoO_4$ possessed characteristic bands at ~349, ~780 (the strongest), ~966 and ~990 cm^{-1}. These bands coincide with the distinctive bands of $Fe_2(MoO_4)_3$ (shifts at ~346, ~784, ~970, and ~990 cm^{-1}) in Routray et al. (2010) and Tian et al. (2005), these shifts are assigned to the bending mode, asymmetric and symmetric stretches of MoO_4. The magnetite spectra exhibited two weak bands at ~298 and ~520 cm^{-1} and two conspicuous broad band at ~110 and 667 cm^{-1}. In the literature, a broad band falls between 661 and 676 cm^{-1} is widely accepted as the only distinct band for magnetite (de Faria et al., 1997; Legodi and Waal, 2007; Monika Hanesch, 2009; Das and Hendry, 2011). However, the broad band at ~110 cm^{-1} has not been reported in the literature. Synthesized 2-line ferrihydrite displayed three broad and weak bands at ~368, ~508, and ~709 cm^{-1}. These bands are consistent with studies in literature (Cornell and Schwertmann, 2003; Monika Hanesch, 2009; Das and Hendry, 2011). The goethite spectra consisted of two conspicuous bands at ~297 and ~384 cm^{-1}, and three weak bands at ~243, ~477, and ~549 cm^{-1}. These identified bands are comparable with previously published values at ~243, ~297, ~385, ~479, and ~549 cm^{-1} (de Faria et al., 1997; Cornell and Schwertmann, 2003; Legodi and Waal, 2007; Monika Hanesch, 2009; Das and Hendry, 2011). The Raman spectra of lepidocrocite were from the published work of Das and Hendry (2011), which featured one strong band at ~249 cm^{-1} together with a few weak peaks at ~140, ~214, ~345, ~374, and ~524 cm^{-1}. These values are in good agreement with previous studies (de Faria et al., 1997; Cornell and Schwertmann, 2003; Monika Hanesch, 2009). Synthesized hematite spectra could be characterized by three sharp and intense bands at ~220, ~290, and ~408 cm^{-1} with three weak bands at ~242, ~496, ~609 cm^{-1}. These strong and weak bands have all been identified in previously reported studies (de Faria et al., 1997; Cornell and Schwertmann, 2003; Legodi and Waal, 2007; Monika Hanesch, 2009; Das and Hendry, 2011). Raman spectroscopy confirmed that the synthesized Fe (hydr)oxides are hematite, goethite, and 2-line ferrihydrite. These strong bands recognized for Fe (hydr)oxides can be used for mineral identification on the Fe-coated sand. The spectra of Synthesized GCS and FCS demonstrated the characteristic bands of silica quartz and the corresponding Fe phase.

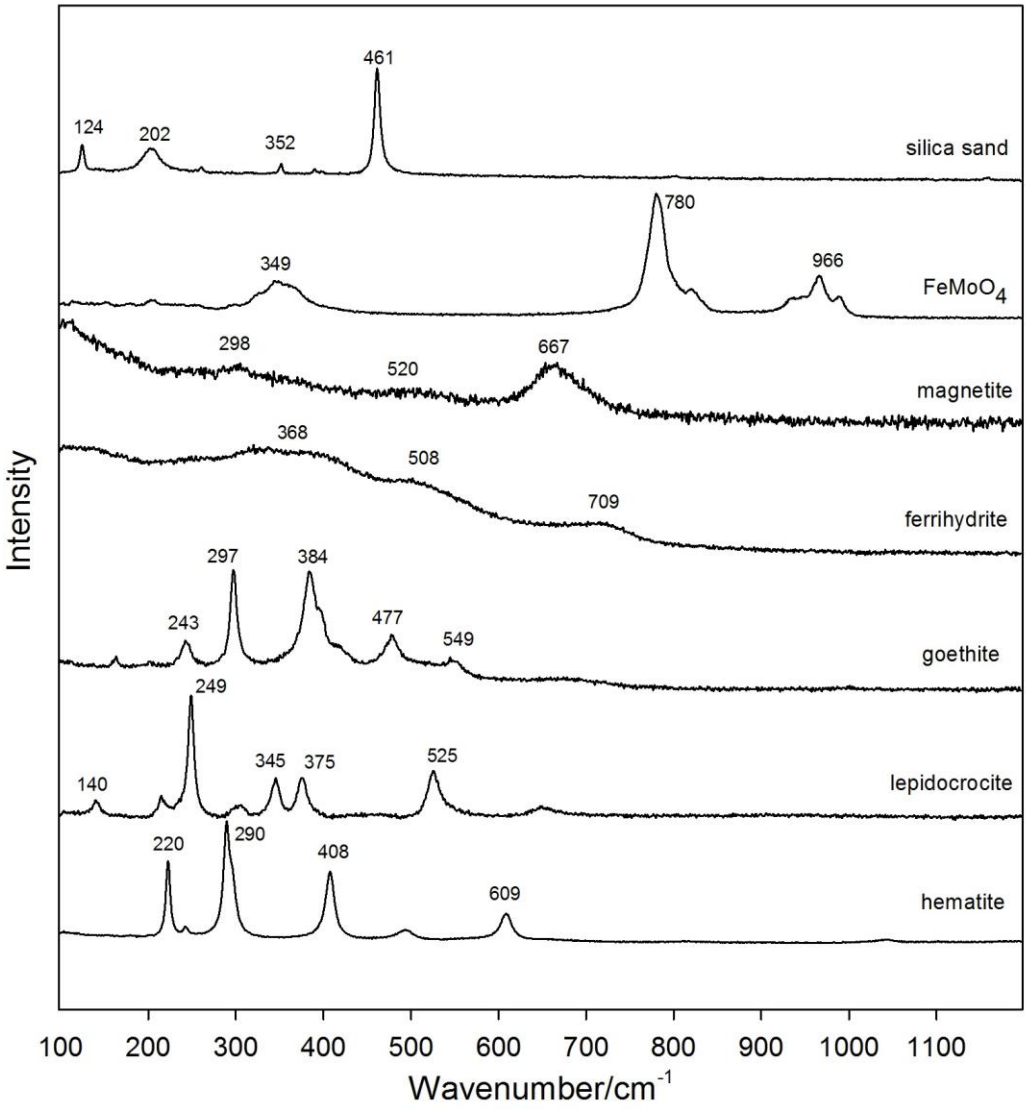

Figure 3.7: Raman spectra of silica sand and synthesized Fe (hydr)oxides.

Table 3.3: Characteristic Raman wavenumber (cm^{-1}) for individual standards.

Silica sand	124, 202, 261, 352, <u>461</u>*
$FeMoO_4$	349, <u>780</u>, 816, 966, 990
Magnetite	110, 298, 520, <u>667</u>
Ferrihydrite	368, 508, <u>709</u>
Goethite	243, 297, <u>384</u>, 477, 549
Lepidocrocite	140, 214, <u>249</u>, 345, 374, 524
Hematite	220, 242, <u>290</u>, 408, 496, 609

*The underlined is the strongest band.

3.3.2.2 Phase I: sorption

Spectra for GCS samples from KQ-1 were consistent with that of silica quartz expect for three additional bands at ~243, ~297 and 385 cm^{-1}, indicating the presence of goethite (Fig. 3.8). The weaker bands of goethite (i.e., ~477, and ~549 cm^{-1}) were not apparent in these spectra due to the low abundance of goethite relative to quartz. Distinct band for adsorbed MoO_4^{2-} was not observed, which is likely due to low Mo concentrations on GCS. Raman spectra for FCS exhibited the characteristic bands of silica quartz as well as the broad and weak bands of ferrihydrite (Fig. 3.9). After Mo adsorption, the spectra of KQ-7 not only displayed the bands of FCS but also showed a broad band at 923 cm^{-1}. And this additional band may be associated to sorbed MoO_4^{2-} (Das and Hendry, 2013). The absence of additional bands indicate that goethite and ferrihydrite transformation did not occur during Phase I.

3.3.2.3 Phase II: reduction

Subsamples from KQ-2 and KQ-3 demonstrated similar band positions: aside from the silica bands, the band at ~250 cm^{-1} was indicative of lepidocrocite. Similarly, the spectra from the ferrihydrite columns (KQ-8 and KQ-9) exhibited the characteristic bands of silica quartz and lepidocrocite. The weak bands of ferrihydrite were not discernable on these spectra. The characteristic band for MoO_4^{2-} (923 cm^{-1}) was not observed as well, wich might be attributed to the decrease in Mo concentration and/or changes in binding coordination.

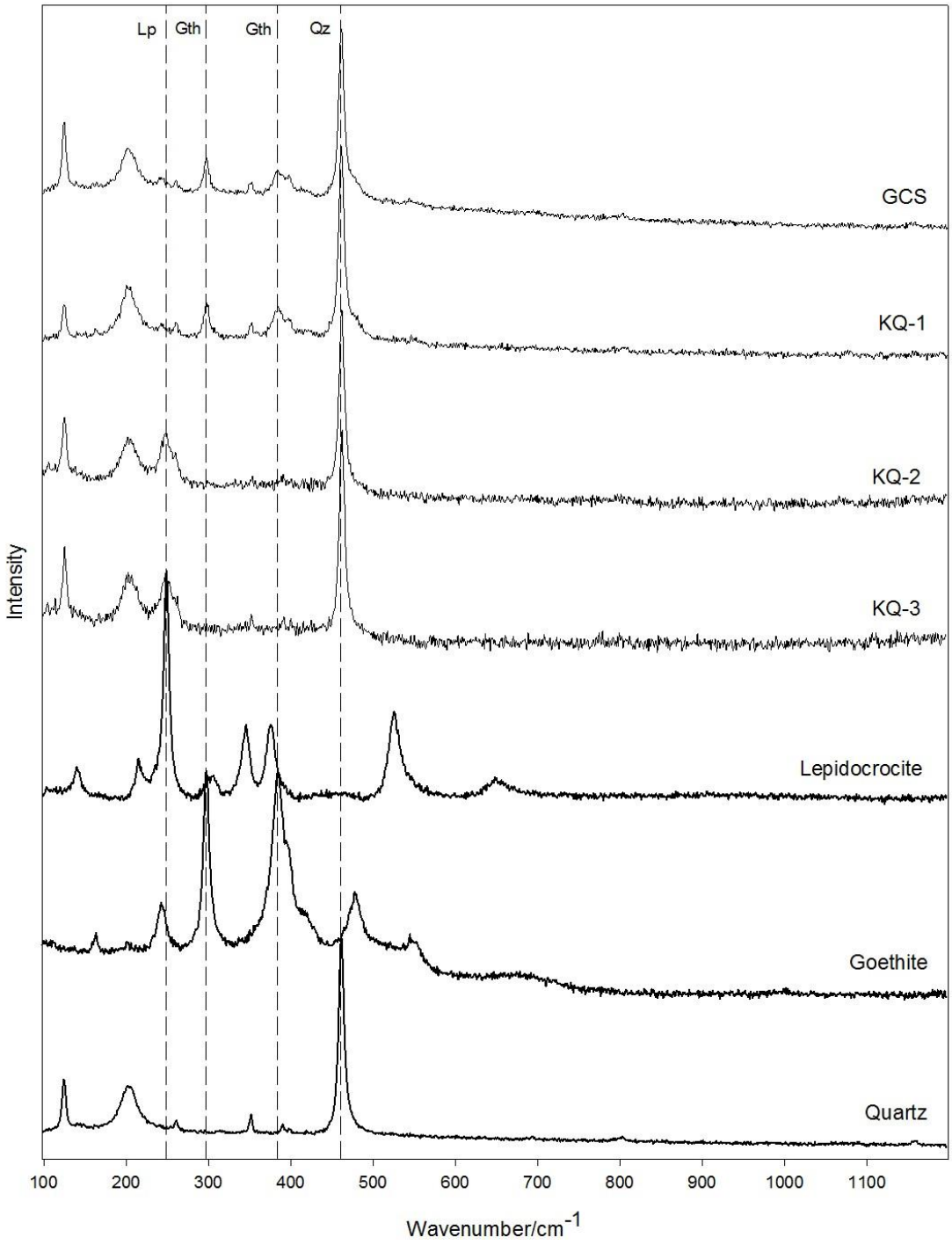

Figure 3.8: Raman spectra of sand samples from the goethite columns before and after reduction.

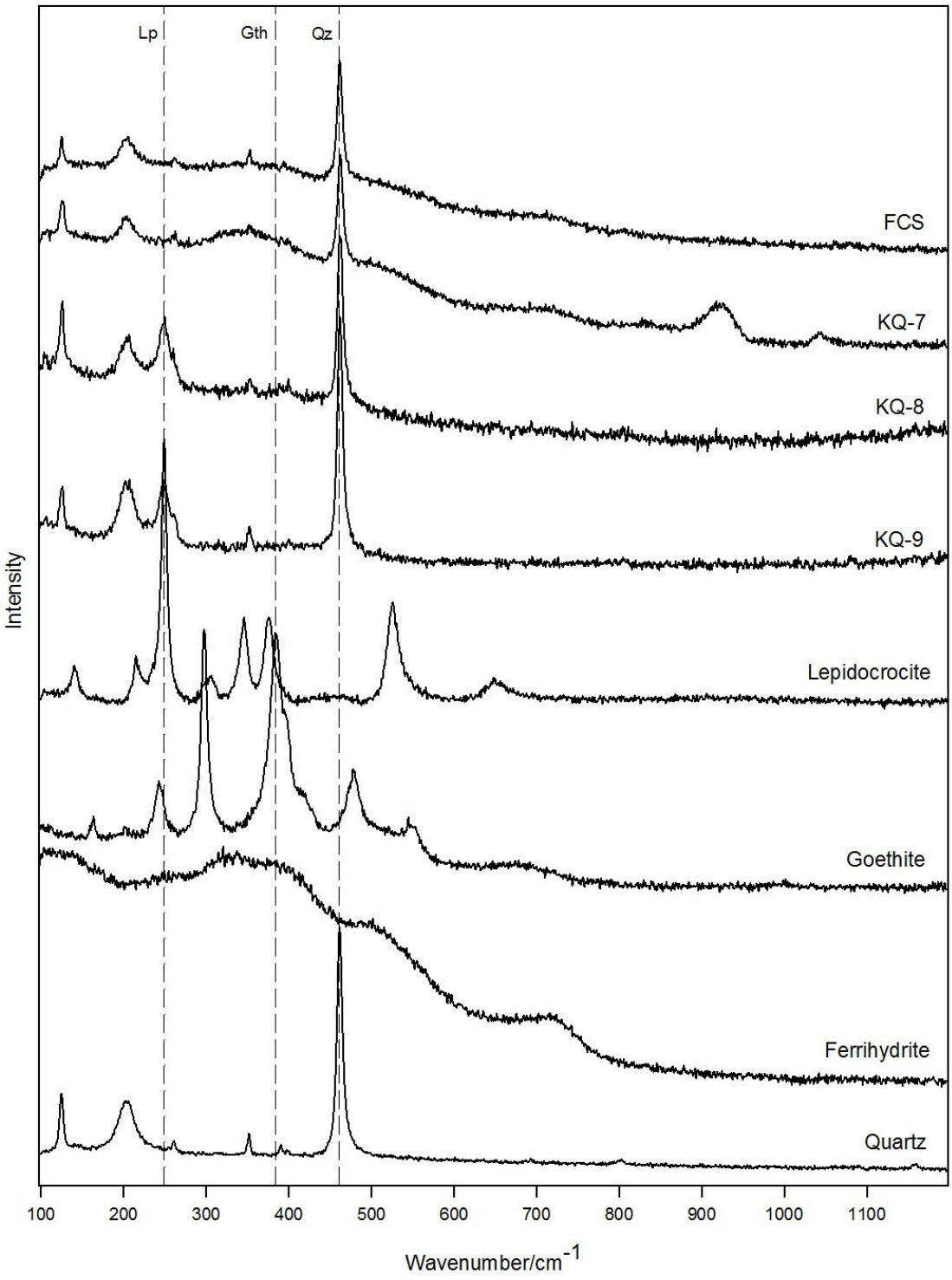

Figure 3.9: Raman spectra of sand samples from the ferrihydrite columns before and after reduction.

3.3.3 Electron microprobe

Backscattered electron images displayed the Fe coatings in whole grain and transection (Fig. 3.10). It can be seen that the grain size varied from 300 to 700 μm in diameter. The iron-rich coatings were not homogeneously distributed and appeared to aggregate on angular margins of sand grains. Compared with the size of the grain, the coating was a very thin layer with a maximum thickness 10 μm (Fig. 3.10(C) and 3.10(F)).

The EDS spectra collected from bright spots demonstrated strong peaks of Fe and relatively weak peaks of Si, suggesting these locations contain high concentrations of Fe (hydr)oxides (Fig. 3.11). Compared with Fe, the relatively high intensity of Mo on the ferrihydrite samples (KQ-8 and KQ-9) indicates higher concentrations of Mo than that of the goethite samples. This observation is consistent with the previously discussed stronger adsorption and retention ability of ferrihydrite.

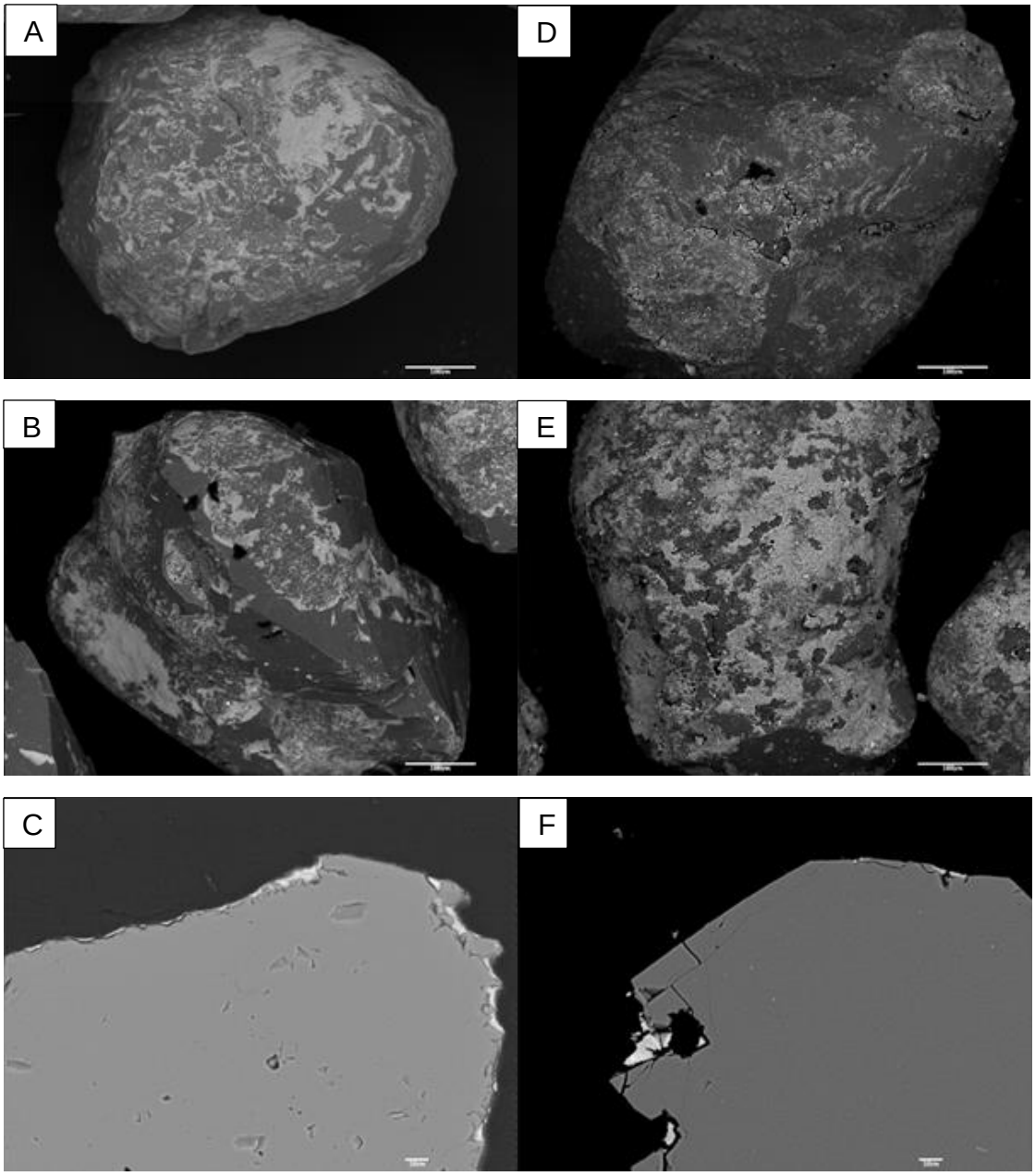

Figue 3.10: BSE images of Fe-coated sand from the reduction columns: (A) KQ-2; (B) KQ-3; (C) Transection of KQ-3; (D) KQ-8; (E) KQ-9; (F) Transection of KQ-9. Scale bars are 100 μm in the whole grain images and 10 μm in the transection images.

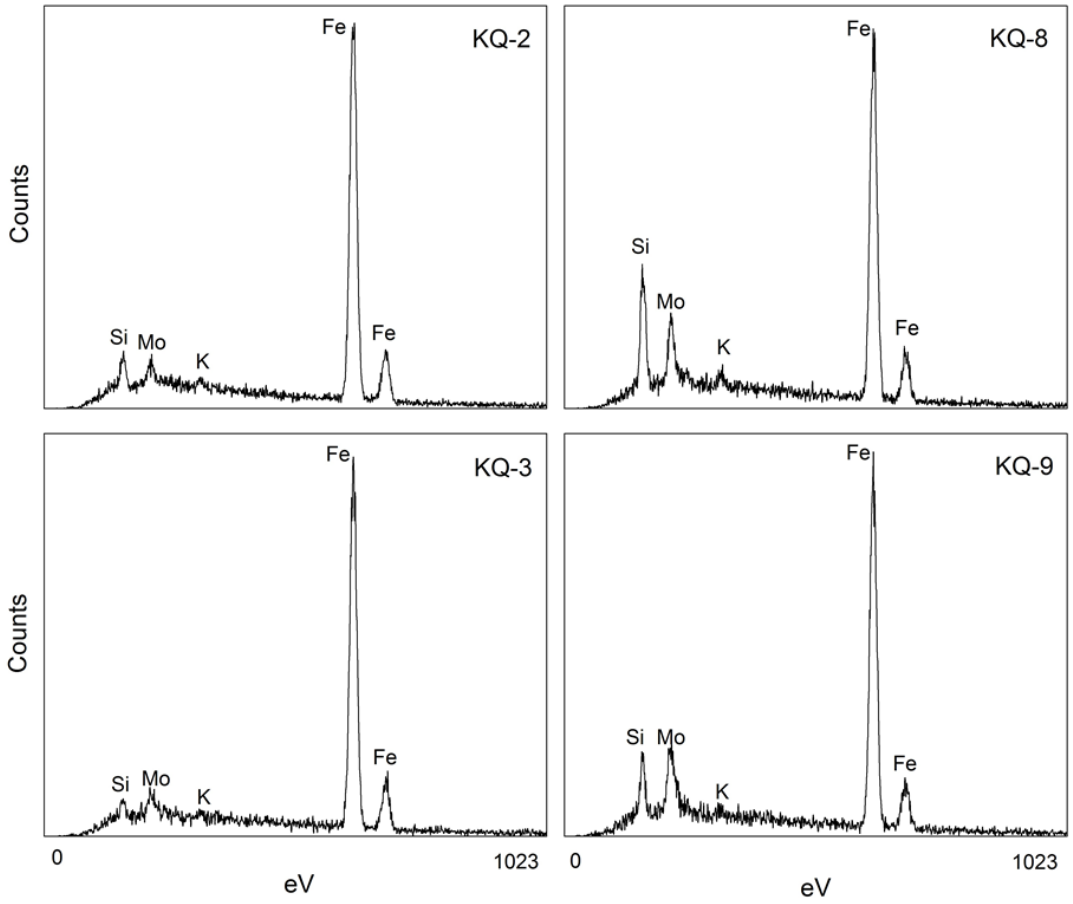

Figure 3.11: The EDS spectra obtained from the bright features showing the characteristic peaks of Si, Mo, and Fe.

3.3.4 Scanning electron microscopy

Iron(III) (hydr)oxides were heterogeneously coated on the sand surface, with localized aggregates growing at the cracks (images not shown). These Fe (hydr)oxides displayed a variety of sizes and shapes. The SEM image from the goethite control column (Fig. 3.12(A)) demonstrated long rod-shaped goethite crystals and a type of small-sized unidentified morphology (Cornell and Schwertmann, 2003; Hansel et al., 2003; Xu and Axe, 2005; Amstaetter et al., 2010; Rusch et al., 2010). The nano-sized ferrihydrite from KQ-7 heavily aggregated on the sand surface (Fig. 3.12(D)). For the reduction columns, the large rod-shaped crystals in the goethite reduction columns (Fig. 3.12(B) and 3.12(C)) resembled the common habit of goethite (Cornell and Schwertmann, 2003; Hansel et al., 2003; Xu and Axe, 2005; Amstaetter et al., 2010; Rusch et al., 2010). However, this morphology was not identified in the ferrihydrite reduction columns (Fig. 3.12(E) and 3.12(F)). Instead, a type of twinned crystals was

commonly found in KQ-8 and KQ-9, which is another possible goethite morphology (Cornell and Schwertmann, 2003; Hansel et al., 2003; Liu et al., 2010). Observed in all the reduction samples, the lath-like/platy crystals indicated the presence of lepidocrocite (Cornell and Schwertmann, 2003; Liu et al., 2010; Bae and Lee, 2013; Kozin et al., 2014); in addition, the hexagonal crystals exhibited the morphology which is consistent with that of green rust (Cornell and Schwertmann, 2003; Ruby et al., 2003; Lindsay et al., 2008; Kocar et al., 2010; Sergent et al., 2011). Ferrimolybdate typically exhibits cyrstals between 50 and 150 nm in size, which could not be discerned from ferrihydrite or goethite nano-crystals by SEM images (Cornell and Schwertmann, 2003; Routray et al., 2010).

Scanning electron microscopy displayed the heterogeneous morphologies of Fe crystals after reduction, which suggested the possible presence of goethite, lepidocrocite, ferrihydrite and green rust. This technique also revealed that goethite exhibited different shapes in the goethite (rod-shaped) and ferrihydrite (twinned) columns. It is suggested that the twinning of goethite can be facilitated by foreign species (Cornell and Schwertmann, 2003). Considering there were more sorbed MoO_4^{2-} in the ferrihydrite columns, MoO_4^{2-} could act as the foreign species to promote the formation of goethite twinning (Cornell and Schwertmann, 2003).

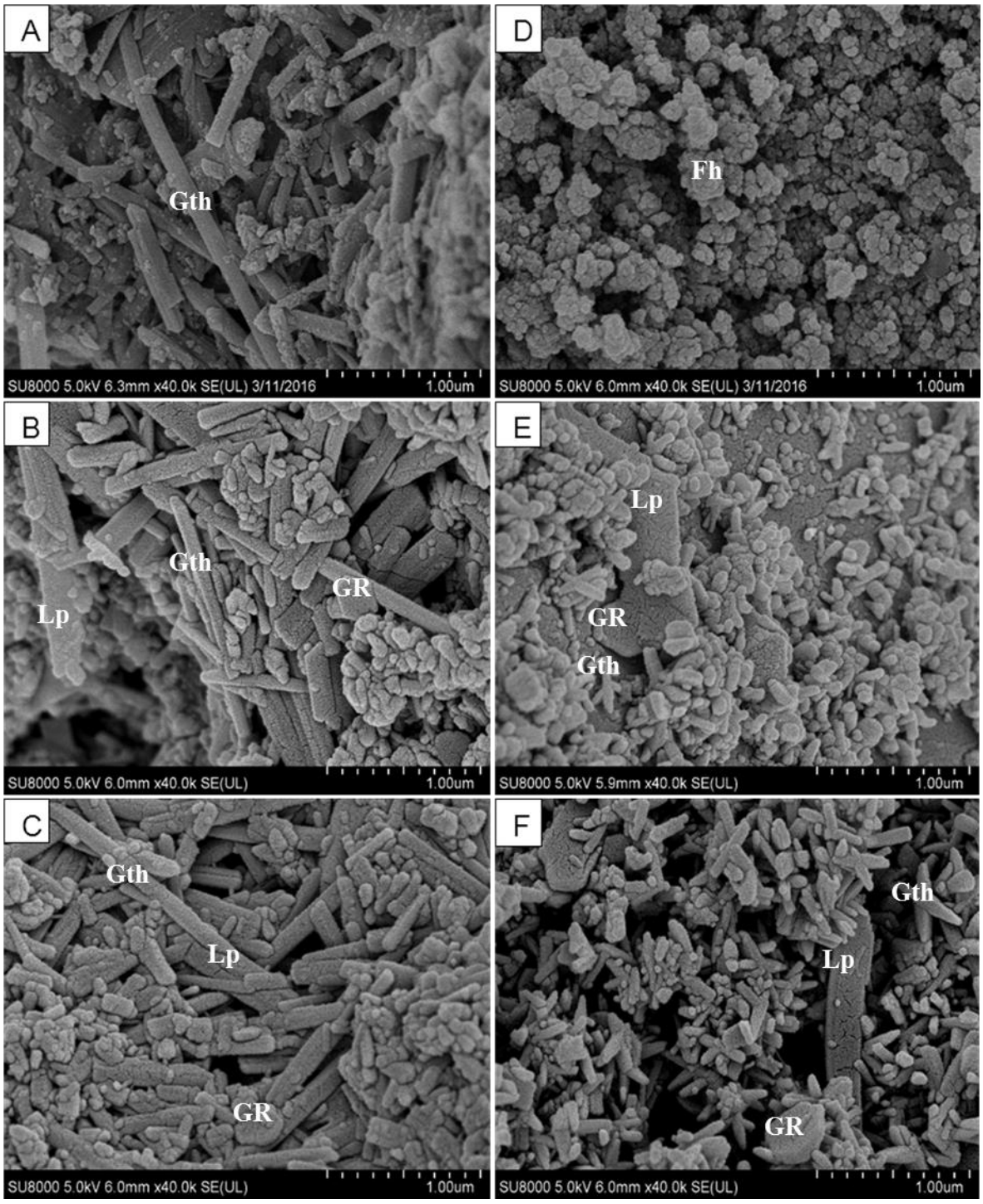

Figure 3.12: SEM images of Fe-coated sand from the control and reduction columns: (A) KQ-1; (B) KQ-2; (C) KQ-3; (D) KQ-7; (E) KQ-8; (F) KQ-9. Scale bars are 1.00 μm.

3.3.5 X-ray adsorption spectroscopy

The Mo K-edge positions were consistent at 20,015 eV for solid-phase samples collected from the 5 – 7 cm intervals following Phase I (sorption) (Fig. 3.13 and 3.14). The Mo K-edge XANES spectra for Phase I GCS (KQ-1) and FCS (KQ-7) samples were characterized by a distinct pre-edge feature at 20,003 eV on the main absorption edge. These spectra are consistent with sorbed Mo in tetrahedral coordination (Arai, 2010). This pre-edge feature was less pronounced in spectra obtained for GCS (KQ-2, KQ-3) and FCS (KQ-8, KQ-9) samples collected following the reduction phase. The decrease in pre-edge intensity likely results from a change in Mo coordination (Ressler et al., 2000; Arai, 2010) or structural disorder (Brinza et al., 2015). Additionally, the post-edge for these Phase II samples exhibited two distinct humps positioned at 20,022 and 20,035 eV that were not apparent in the Phase I sample spectra. These two post-edge features were generally consistent with those observed for molybdenum trioxide [MoO_3], which is characterized by octahedral Mo coordination (Ressler et al., 2000; Arai, 2010). The spectrum obtained for a KQ-8 exhibited a slightly larger pre-edge peak but similar post-edge features to that of KQ-9. This observation suggests that Mo within KQ-8 may be characterized by a combination of tetrahedral and octahedral coordination environment, which signifys that the changes in Mo coordination is kinetically controlled. These changes in the Mo coordination environment suggest that Mo phases exhibiting tetrahedral Mo(VI) coordination (i.e., $FeMoO_4$, $Fe_2(MoO_4)_3$) were less likely to form (Sejkora et al., 2014).

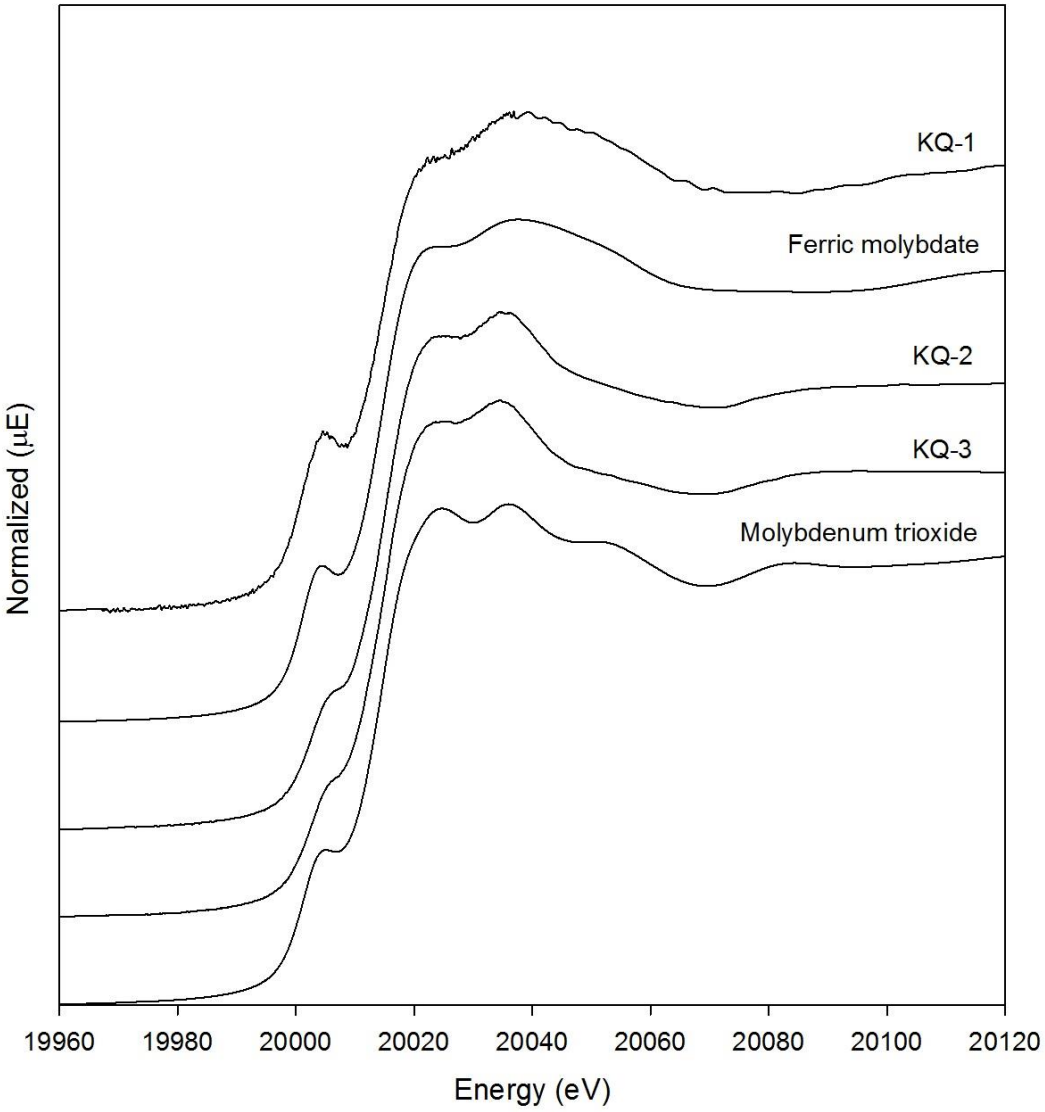

Figure 3.13: Molybdenum K-edge XANES spectra collected following Phase I (KQ-1) and Phase II (KQ-2, KQ-3) in the goethite columns.

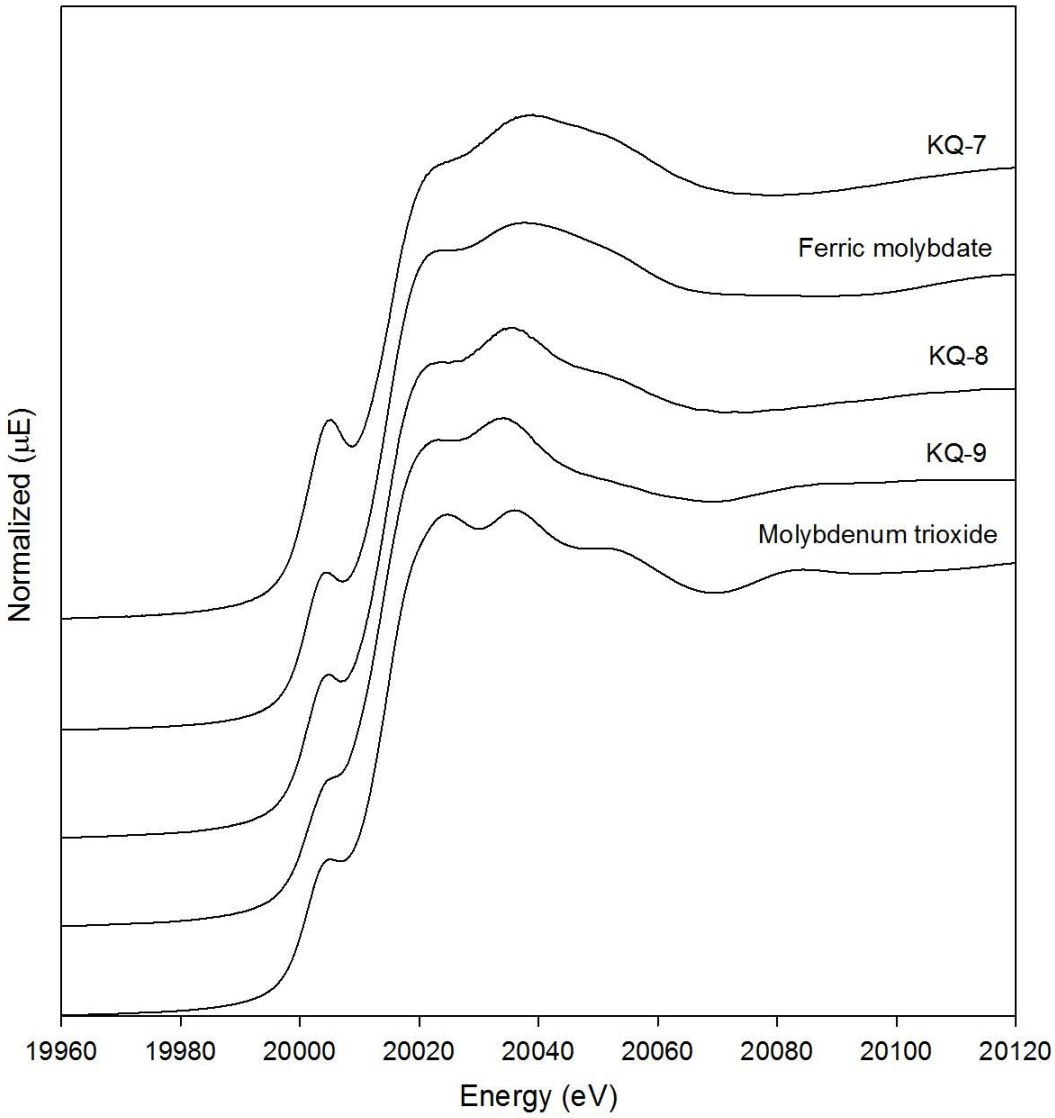

Figure 3.14: Molybdenum K-edge XANES spectra collected following Phase I (KQ-7) and Phase II (KQ-8, KQ-9) in the ferrihydrite columns.

Chapter 4 Discussion

4.1 Molybdate behaviour

4.1.1 Phase I: sorption

Adsorption capacity evaluated by the mass ratio of Mo/Fe followed the order: ferrihydrite > goethite > hematite. This result is consistent with previous studies and can be related to the order of their specific surface area (Vlek and Lindsay, 1977; McKenzie, 1983; Bibak and Borggaard, 1994; Schwertmann and Cornell, 2000; Usman et al., 2012a). Ferrihydrite is amorphous and generally has a higher surface area ranging from 100 to 700 m^2 g^{-1}; goethite possesses less surface area which varies from 30 to 100 m^2 g^{-1} ; hematite is more crystalline and its surface area is in the range between 10 and 90 m^2 g^{-1} (Schwertmann and Cornell, 2000; Cornell and Schwertmann, 2003).

As another adsorptive anion in the input solution, SO_4^{2-} has the potential to compete for sorption sites with MoO_4^{2-}. However, there was no distinct SO_4^{2-} concentration difference between the influent and the effluent, which indicates that SO_4^{2-} sorption is minimal. Molybdate adsorption was much stronger than that of SO_4^{2-}, suggesting different adsorption mechanisms. The present study strongly support previous findings that MoO_4^{2-} adsorption onto Fe (hydr)oxides is through inner-sphere complexation, whereas SO_4^{2-} adsorption is considered as outer-sphere complexation (Hayes et al., 1988; Zhang and Sparks, 1989; Bibak and Borggaard, 1994; Goldberg and Forster, 1998; Gustafsson, 2003; Arai, 2010; Xu et al., 2013). Therefore, the increasing trend in solid-phase S along the column can be explained by the competing adsorption mechanism: MoO_4^{2-} is completely retained in the columns through inner-sphere complexation progressively from the inlet to the outlet until breakthrough; in contrast, SO_4^{2-} adsorption (outer-sphere) is outcompeted by MoO_4^{2-}, while the majority flush through and only a small amount is captured down the columns. It is speculated that over time a portion of the sorbed SO_4^{2-} complexes changes from outer- to inner-sphere, which becomes capable of competing for the

sorption sites with MoO_4^{2-}; when MoO_4^{2-} sorption progresses down the columns, it is unable to replace the inner-sphere SO_4^{2-} complexes.

4.1.2 Phase II: reduction

Molybdenum was released from all columns following Fe(II) introduction. Effluent Mo concentrations were greatest at the onset of the reduction phase, which coincided with acid production and Fe(II) retention. The trend in pH and Fe(II) signify that Fe(III) (Hydr)oxides was precipitating, and here Fe(III) was produced by the oxidation of Fe(II):

$$3H_2O + Fe^{3+} \rightarrow Fe(OH)_{3(s)} + 3H^+ \quad (4.1)$$

The mirroring effect between Mo release and Fe(II) breakthrough/acid production suggests a concomitant process of Fe(III) (Hydr)oxides precipitation and Mo mobilization. To explore the relationship between released Mo and retained Fe, concentration differences of Mo and Fe(II) in the influent and effluent were compared (Fig. 4.1). Pearson correlation coefficients are 0.824 and 0.740 in the low and high Fe columns, respectively, which suggest a positive correlation between Mo release and Fe retention during the reduction experiment. It is inferred that Mo mobilization occurs during Fe(II)-induced Fe (hydr)oxide transformation and ceases when the transformation is completed.

The majority of released Mo occurred near the column inlet. The immediate mobilization of Mo at the onset of reduction can be explained by (1) the sudden reduce in surface area as a result of reductive transformation; (2) the released Mo could not be re-adsorbed because the columns completed Mo breakthrough and there was no available adsorption sites down the columns; (3) the secondary mineral formation is kinetically controlled, and the remaining Mo was sequestered by the secondary products over time, which results in the decreased release in the effluent.

The degree of Mo elution was influenced by Fe(II) concentration and the mineral precursor (goethite/ferrihydrite). Increasing Fe(II) concentration by an order of magnitude (from 0.2 mM to 2.0 mM) can substantially enhance Mo sequestration in both the goethite and ferrihydrite columns. Moreover, the ferrihydrite columns overall had a stronger ability to sequester Mo than the goethite columns at both low and high Fe concentrations, and similar retention ability has been observed for As (Tufano et al., 2008). Since the original goethite and ferrihydrite both underwent reductive transformation, it is suggested that the ferrihydrite systems have a stronger

ability to retain Mo compared with the goethite systems. Therefore, it is the interaction of Fe(II) concentration and the mineral precursor that governs Mo release.

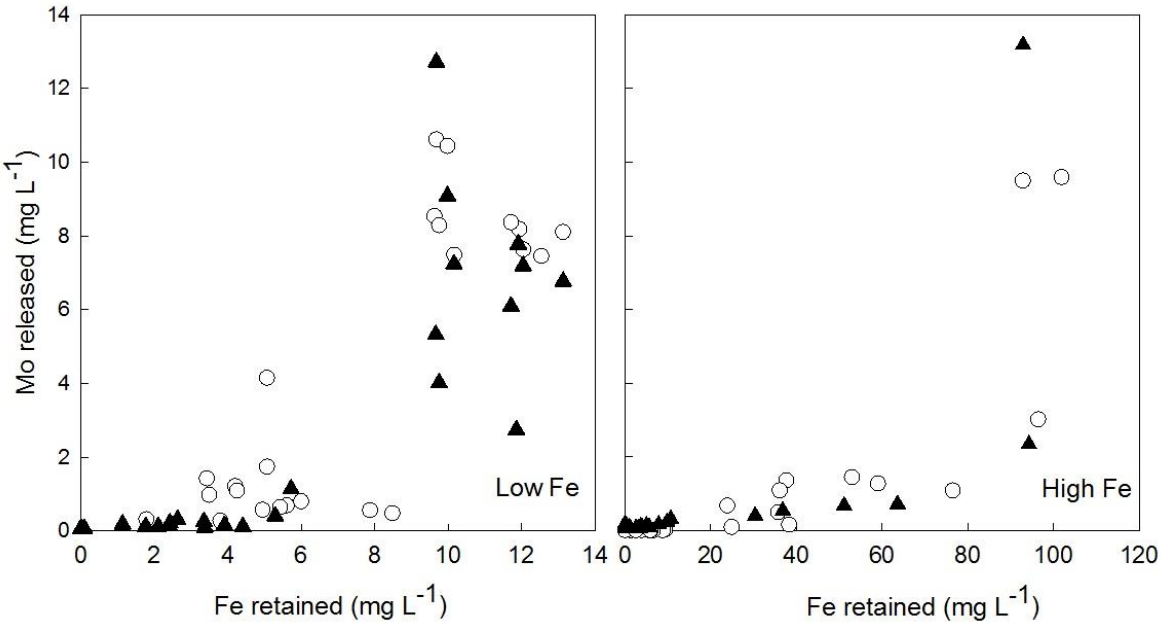

Figure 4.1: Concentration differences in Fe (retained in the solids) and Mo (released in the solution). Circles: the ferrihydrite columns and triangles: the goethite columns. Left: low Fe influent and effluent (KQ-2 and KQ-8); Right: high Fe influent and effluent (KQ-3 and KQ-9).

During reduction, a period of stable Mo and Fe concentrations was observed in the ferrihydrite columns but not in the goethite columns, which implies that the mineral precursor plays a role in the transformation mechanisms. In addition, the low Fe columns exhibited a longer reaction period in Mo release and Fe(II) retention than the high Fe columns; this result suggests the phase transformation kinetics is influenced by Fe(II) concentration (Hansel et al., 2003, 2004; Yang et al., 2010). As a consequence, Fe(II) concentration and the mineral precursor jointly influences the transformation mechanisms and kinetics, which dictates the composition of Fe transformation products and the extent of Mo sequestration. X-ray absorption spectroscopy indicated that the Mo coordination environment had changed from tetrahedral to octahedral during reduction (Phase II). These coordination changes suggest Mo substituted for the octaherally coordinated Fe in the transformation products (Brinza et al., 2015; Das et al., 2016). Since the ionic radius of Mo(VI) (73 pm) is slightly larger than that of Fe(III) (69 pm), Mo might increase the volume of the unit cell and result in a disordered geometry (Shannon, 1976; Brinza et al., 2015; Das et al., 2016). The slight peak shifts observed in post-reduction Mo K-edge XANES

spectra could also be indicative of a change in Mo oxidation state (Ressler et al., 2000, 2002). Further investigation identifying the oxidation state and the local coordination environment of Mo will be important for understanding the interaction between Mo and Fe (hydr)oxide under reducing conditions.

In addition, although $FeMoO_4$ and $Fe_2(MoO_4)_3$ precipitation during Phase II cannot be ruled out, the observed inverse relationship between effluent Mo and Fe concentrations suggests that these phases are unlikely to be major controls on Mo mobility. Furthermore, the XANES spectra reavealed that Mo coordination environment was largely octahedral, which suggests these Fe(II)-Mo(VI) phases were unlikely an important control on Mo mobility.

4.2 Fe (hydr)oxide transformation

4.2.1 Goethite

In the literature, no new phase was observed during the reduction of goethite (Coughlin and Stone, 1996; Hansel et al., 2005; Amstaetter et al., 2010; Beard et al., 2010; Handler et al., 2014). However, the present study showed column color change during reduction. In addition, changes in Mo coordination observed in Mo K-edge XANES spectra further suggests the interpretation that goethite transformation might occur. Raman spectroscopy indicated lepidocrocite formation and SEM displayed heterogeneous morphologies, indicating the presence of goethite, lepidocrocite, and possibly green rust. These observations suggest that mineralogical transformation during the abiotic reduction of goethite might happen and lepidocrocite is very likely to form as the transformation product. Considering the crystallographic unit cell of lepidocrocite and goethite are both orthorhombic, structural similarities permit solid state transformation from goethite to lepidocrocite (Jolivet et al., 1992; Cornell and Schwertmann, 2003; Cudennec and Lecerf, 2005; Liu et al., 2005; Lu et al., 2011; Usman et al., 2012b). Compared with the ferrihydrite columns, solid state transformation may explain the faster transformation rate in the goethite columns as it is much faster than dissolution/re-precipitation (Liu et al., 2009; Lu et al., 2011; Gomez et al., 2013). In this case, kinetic constraints override the thermodynamics which allow the formation of metastable lepidocrocite instead of goethite. Note that the lower level of Mo loadings in the goethite columns can be another factor for faster transformation rate.

As the polymorph of goethite, lepidocrocite is thermodynamically less stable and subject to structural rearrangement. Accordingly, in the long term, lepidocrocite conversion to the thermodynamically more stable goethite may proceed in solid forms (Cornell and Schwertmann, 2003; Hansel et al., 2003; Liu et al., 2007). It is understandable that mineralogical analyses may not be timely attained under certain circumstances. Therefore, the subsequent structural rearrangement from lepidocrocite to goethite can be a reason to explain why there was no new phase recorded if lepidocrocite is confirmed as the product. However, lepidocrocite formation can not be ruled out from the oxidation and subsequent dehydration of sorbed Fe(II) (Hansen et al., 1994; Schwertmann and Fechter, 1994; Schwertmann and Cornell, 2000). Therefore, future investigation regarding the transformation product of goethite will be needed.

4.2.2 Ferrihydrite

Raman spectroscopy and SEM suggested that lepidocrocite is the secondary product of Fe(II)-induced ferrihydrite transformation, though minor phases, such as green rust and goethite, may also exist. The transformation product suite is in good agreement with the prediction made based on previously published results (Benner et al., 2002; Hansel et al., 2005; Liu et al., 2007, 2010; Zachara et al., 2011). Lepidocrocite and goethite were commonly observed as the products of ferrihydrite reacting with Fe(II) at low concentrations; lepidocrocite formation is promoted at pH less than 7 and in the presence of Cl^-, whilst goethite formation was favored by HCO_3^- and SO_4^{2-} but suppressed by Cl^- (Schwertmann and Cornell, 2000; Hansel et al., 2003, 2005; Liu et al., 2008). Magnetite, which is widely reported during the interaction with high concentrations of Fe(II), was not observed in this study (Tronc et al., 1992; Schwertmann and Cornell, 2000; Benner et al., 2002; Hansel et al., 2005; Thomas et al., 2007; Liu et al., 2010; Yang et al., 2010; Zachara et al., 2011; Boland et al., 2014). Consequently, the presence of Cl^- in the influent promoted the formation of lepidocrocite (Schwertmann and Cornell, 2000; Hansel et al., 2003, 2005; Liu et al., 2008). The transformation from ferrihydrite to lepidocrocite is widely accpeted as a dissolution/reprecipitation process because there is no structural relationship between the transformation percursor and the product (Cornell et al., 1989; Benner et al., 2002; Hansel et al., 2003, 2005; Liu et al., 2009). Ferrihydrite has a hexagonal crystallographic structure while lepidocrocite belongs to the orthorhombic system (Cornell and Schwertmann, 2003; Cudennec and Lecerf, 2005; Lu et al., 2011).

Although the transformation rate of ferrihydrite (dissolution/reprecipitation) was slower than that of goethite (via solid state transformation and/or dissolution/re-precipitation), increasing Fe(II) concentration by an order of magnitude substantially accelerated the transformation velosity and improved Mo retention. Consequently, the amount of adsorbed Fe(II) and its transport rate from solution to solid surface, the dissolution rate of the precursor and its structural relationship with the products jointly dictate the type and precipitation rate of secondary minerals and the extent of Mo re-partitioning.

Chapter 5 Conclusions

The present study demonstrated that Fe (hydr)oxides can effectively attenuate MoO_4^{2-} at circumneutral pH conditions through inner-sphere complexation. Adsorption capacity evaluated by the mass ratio of Mo/Fe followed the order: ferrihydrite > goethite > hematite. Subsequent reductive transformation induced by dissolved Fe(II) led to Mo mobilization typically near the column inlet. The degree of Mo elution was influenced by Fe(II) concentration and the precursor (goethite/ferrihydrite): Mo mobilization was greater at low (0.2 mM) compared to high (2.0 mM) Fe(II) concentrations; the ferrihydrite columns overall had a stronger ability to sequester Mo.

On the other hand, mineralogical transformation was identified and lepidocrocite was suggested to be the primary transformation product in both the goethite and ferrihydrite columns. Although the transformation rate of ferrihydrite was slower than that of goethite, increasing Fe(II) concentration by an order of magnitude substantially accelerated the transformation velosity and improved Mo retention. Consequently, Fe(II) concentration and the mineral precursor jointly influences the transformation mechanisms and kinetics, which dictates the composition of transformation products and extent of Mo release. X-ray absorption spectroscopy (XAS) indicated that the coordination environment changed from tetrahedral to octahedral during reduction, which suggests Mo might be partially reduced and structurally incorporated into the Fe (hydr)oxide transformation products. A slight shift in the Mo K-edge position suggests that changes in Mo oxidation state cannot be ruled out. Future work identifying the local coordination environment of Mo and the associated secondary products can be helpful in understanding the interaction of Mo re-partitioning and phase transformation.

Iron (II)-induced reductive transformation of Fe (hydr)oxides leads to Mo re-partitioning: the majority of the pre-adsorbed Mo was retained in the columns, which experienced changes in coordination environment, suggesting possible Mo substitution of Fe. The resulting structural incorporation could have important environmental implications: the shift from surface adsorption

to structural fixation strengthens the interaction of Mo and Fe (hydr)oxides, which can limit subsequent Mo release in the long term.

References

Adelson, J.M., Helz, G.R., Miller, C. V., 2001. Reconstructing the rise of recent coastal anoxia; molybdenum in Chesapeake Bay sediments. Geochim. Cosmochim. Acta 65, 237–252.

Amstaetter, K., Borch, T., Larese-casanova, P., Kappler, A., 2010. Redox transformation of arsenic by Fe(II)-activated goethite(α-FeOOH). Environ. Sci. Technol. 44, 102–108.

Antelo, J., Fiol, S., Gondar, D., López, R., Arce, F., 2012. Comparison of arsenate, chromate and molybdate binding on schwertmannite: surface adsorption vs anion-exchange. J. Colloid Interface Sci. 386, 338–343.

Arai, Y., 2010. X-ray absorption spectroscopic investigation of molybdenum multinuclear sorption mechanism at the goethite-water interface. Environ. Sci. Technol. 44, 8491–8496.

Bae, S., Lee, W., 2013. Biotransformation of lepidocrocite in the presence of quinones and flavins. Geochim. Cosmochim. Acta 114, 144–155.

Balistrieri, L.S., Box, S., Tonkin, J.W., 2003. Modeling Precipitation and Sorption of Elements during Mixing of River Water and Porewater in the Coeur d'Alene River Basin. Environ. Sci. Technol. 37, 4694–4701.

Bay, D.S., Peterson, H.E., Singurindy, O., Aranda, C., Dockrey, J.W., Vargas, F.S., Gallegos, J.C.C., Mayer, K.U., Smith, L., Klein, B., Beckie, R.D., 2009. Assessment of Neutral pH Drainage from Three Experimental Waste-Rock Piles at the Antamina Mine, Peru, in: 8th International Conference on Acid Rock Drainage. pp. 188–199.

Beard, B.L., Handler, R.M., Scherer, M.M., Wu, L., Czaja, A.D., Heimann, A., Johnson, C.M., 2010. Iron isotope fractionation between aqueous ferrous iron and goethite. Earth Planet. Sci. Lett. 295, 241–250.

Benner, S.G., Hansel, C.M., Wielinga, B.W., Barber, T.M., Fendorf, S., 2002. Reductive dissolution and biomineralization of iron hydroxide under dynamic flow conditions. Environ. Sci. Technol. 36, 1705–1711.

Bergerhoff, G., Hundt, R., Sievers, R., Brown, I.D., 1983. The inorganic crystal structure data base. J. Chem. Inf. Model. 23, 66–69.

Bibak, A., Borggaard, O.K., 1994. Molybdenum adsorption by aluminum and iron oxides and humic acid. Soil Sci. 158, 323–328.

Boland, D.D., Collins, R.N., Miller, C.J., Glover, C.J., Waite, T.D., 2014. Effect of solution and solid-phase conditions on the Fe(II)-accelerated transformation of ferrihydrite to lepidocrocite and goethite. Environ. Sci. Technol. 48, 5477–5485.

Boland, D.D., Collins, R.N., Payne, T.E., Waite, T.D., 2011. Effect of amorphous Fe(III) oxide transformation on the Fe(II)-mediated reduction of U(VI). Environ. Sci. Technol. 45, 1327–1333.

Bonzongo, J.J., Nemer, B.W., Lyons, W.B., 2006. Hydrologic controls on water chemistry and mercury biotransformation in a closed river system: The Carson River, Nevada. Appl. Geochemistry 21, 1999–2009.

Bostick, B.C., Fendorf, S., Helz, G.R., 2003. Differential adsorption of molybdate and tetrathiomolybdate on pyrite (FeS_2). Environ. Sci. Technol. 37, 285–291.

Bourikas, K., Hiemstra, T., Riemsdijk, W.H. Van, 2001. Adsorption of molybdate monomers and polymers on titania with a multisite approach. J. Phys. Chem. B 105, 2393–2403.

Brinza, L., Vu, H.P., Shaw, S., Mosselmans, J.F.W., Benning, L.G., 2015. Effect of Mo and V on the hydrothermal crystallization of hematite from ferrihydrite: An in situ energy dispersive X-ray diffraction and X-ray absorption spectroscopy study. Cryst. Growth Des. 15, 4768–4780.

Burton, E.D., Johnston, S.G., Bush, R.T., 2011. Microbial sulfidogenesis in ferrihydrite-rich environments: Effects on iron mineralogy and arsenic mobility. Geochim. Cosmochim. Acta 75, 3072–3087.

Carlson, L., Schwertmann, U., 1990. The effect of CO_2 and oxidation rate on the formation of goethite versus lepidocrocite from an Fe(II) system at pH 6 and 7. Clay Miner. 25, 65–71.

Carroll, K.C., Artiola, J.F., Brusseau, M.L., 2006. Transport of molybdenum in a biosolid-amended alkaline soil. Chemosphere 65, 778–785.

Conlan, M.J.W., Mayer, K.U., Blaskovich, R., Beckie, R.D., 2012. Solubility controls for molybdenum in neutral rock drainage. Geochemistry Explor. Environ. Anal. 12, 21–32.

Cornell, R.M., Schneider, W., Giovanoli, R., 1989. Phase transformations in the ferrihydrite/cysteine system. Polyhedron 8, 2829–2836.

Cornell, R.M., Schwertmann, U., 2003. The Iron Oxides: Structure, Properties, Reactions, Occurences and Uses, 2nd ed. Wiley-VCH Verlag GmbH & Co. KGaA, Weinheim.

Coughlin, B.R., Stone, A.T., 1996. Nonreversible adsorption of divalent metal ions (Mn^{II}, Co^{II}, Ni^{II}, Cu^{II}, and Pb^{II}) onto goethite: effects of acidification, Fe^{II} addition, and picolinic acid addition. Environ. Sci. Technol. 29, 2445–2455.

Courtin-Nomade, A., Bril, H., Beny, J.-M., Kunz, M., Tamura, N., 2010. Sulfide oxidation

observed using micro-Raman spectroscopy and micro-X-ray diffraction: The importance of water/rock ratios and pH conditions. Am. Mineral. 95, 582–591.

Cruywagen, J.J., 2000. Protonation, oligomerization, and condensation reactions of vanadate(V), molybdate(VI), and tungstate(VI). Adv. Inorg. Chem. 49, 127–182.

Cudennec, Y., Lecerf, A., 2006. The transformation of ferrihydrite into goethite or hematite, revisited. J. Solid State Chem. 179, 716–722.

Cudennec, Y., Lecerf, A., 2005. Topotactic transformations of goethite and lepidocrocite into hematite and maghemite. Solid State Sci. 7, 520–529.

Dalai, T.K., Nishimura, K., Nozaki, Y., 2005. Geochemistry of molybdenum in the Chao Phraya River estuary, Thailand: Role of suboxic diagenesis and porewater transport. Chem. Geol. 218, 189–202.

Das, A.K., Chakraborty, R., Cervera, M.L., de la Guardia, M., 2007. A review on molybdenum determination in solid geological samples. Talanta 71, 987–1000.

Das, S., Essilfie-Dughan, J., Hendry, M.J., 2016. Applied Geochemistry Sequestration of molybdate during transformation of 2-line ferrihydrite under alkaline conditions. Appl. Geochemistry 73, 70–80.

Das, S., Essilfie-dughan, J., Hendry, M.J., 2015. Fate of adsorbed arsenate during phase transformation of ferrihydrite in the presence of gypsum and alkaline conditions. Chem. Geol. 411, 69–80.

Das, S., Hendry, M.J., 2013. Adsorption of molybdate by synthetic hematite under alkaline conditions: Effects of aging. Appl. Geochemistry 28, 194–201.

Das, S., Hendry, M.J., 2011. Application of Raman spectroscopy to identify iron minerals commonly found in mine wastes. Chem. Geol. 290, 101–108.

Das, S., Hendry, M.J., Essilfie-Dughan, J., 2011a. Effects of adsorbed arsenate on the rate of transformation of 2-line ferrihydrite at pH 10. Environ. Sci. Technol. 45, 5557–5563.

Das, S., Hendry, M.J., Essilfie-dughan, J., 2011b. Transformation of two-line ferrihydrite to goethite and hematite as a function of pH and temperature. Environ. Sci. Technol. 45, 268–275.

de Faria, D.L.A., Silva, S.V., de Oliveira, M.T., 1997. Raman microspectroscopy of some iron oxides and oxyhydroxides. J. Raman Spectrosc. 28, 873–878.

Dodbiba, G., Fujita, T., Kikuchi, T., Manjanna, J., Matsuo, S., Takahashi, H., Tohji, K., 2011. Synthesis of iron-based adsorbents and their application in the adsorption of molybdenum ions in nitric acid solution. Chem. Eng. J. 166, 496–503.

Erickson, B.E., Helz, G.R., 2000. Molybdenum(VI) speciation in sulfidic waters: Stability and lability of thiomolybdates. Geochim. Cosmochim. Acta 64, 1149–1158.

Essilfie-Dughan, J., Pickering, I.J., Hendry, M.J., George, G.N., Kotzer, T., 2011. Molybdenum Speciation in Uranium Mine Tailings Using X-Ray Absorption Spectroscopy. Environ. Sci. Technol. 45, 455–460.

Fendorf, S., Michael, H.A., Geen, A. van, 2010. Spatial and temporal variations of groundwater arsenic in South and Southeast Asia. Science (80-.). 328, 1123–1127.

Fredrickson, J.K., Zachara, J.M., Kukkadapu, R.K., Gorby, Y.A., Smith, S.C., Brown, C.F., 2001. Biotransformation of Ni-substituted hydrous ferric oxide by an Fe(III)-reducing bacterium. Environ. Sci. Technol. 35, 703–712.

Frierdich, A.J., Catalano, J.G., 2012. Controls on Fe(II)-activated trace element release from goethite and hematite. Environ. Sci. Technol. 46, 1519–1526.

Gibbs, M.M., 1979. A simple method for the rapid determination of iron in natural waters. Water Res. 13, 295–297.

Goldberg, S., 2010. Competitive adsorption of molybdenum in the presence of phosphorus or sulfur on gibbsite. Soil Sci. 175, 105–110.

Goldberg, S., 2009. Influence of soil solution salinity on molybdenum adsorption by soils. Soil Sci. 174, 9–13.

Goldberg, S., Forster, H.S., 1998. Factors affecting molybdenum adsorption by soils and minerals. Soil Sci. 163, 109–114.

Goldberg, S., Forster, H.S., Godfrey, C.L., 1996. Molybdenum adsorption on oxides, clay minerals, and soils. Soil Sci. Soc. Am. J. 60, 425–432.

Gomez, M.A., Hendry, M.J., Hossain, A., Das, S., Elouatik, S., 2013. Abiotic reduction of 2-line ferrihydrite: effects on adsorbed arsenate, molybdate, and nickel. RSC Adv. 3, 25812–25822.

Greenleaf, J.E., Cumbal, L., Staina, I., Sengupta, A.K., 2003. Abiotic As(III) oxidation by hydrated Fe(III) oxide (HFO) microparticles in a plug flow columnar configuration. Process Saf. Environ. Prot. 81(2), 87–98.

Gupta, V.K., Saini, V.K., Jain, N., 2005. Adsorption of As(III) from aqueous solutions by iron oxide-coated sand. J. Colloid Interface Sci. 288, 55–60.

Gustafsson, J.P., 2003. Modelling molybdate and tungstate adsorption to ferrihydrite. Chem. Geol. 200, 105–115.

Handler, R.M., Frierdich, A.J., Johnson, C.M., Rosso, K.M., Beard, B.L., Wang, C., Latta, D.E., Neumann, A., Pasakarnis, T., Premaratne, W.A.P.J., Scherer, M.M., 2014. Fe(II)-Catalyzed

Recrystallization of Goethite Revisited. Environ. Sci. Technol. 48, 11302–11311.

Hanna, K., Rusch, B., Lassabatere, L., Hofmann, A., Humbert, B., 2010. Reactive transport of gentisic acid in a hematite-coated sand column: Experimental study and modeling. Geochim. Cosmochim. Acta 74, 3351–3366.

Hanna, K., Usman, M., Chatain, V., 2013. Sorption and transport of aqueous Fe^{II} in a goethite-coated sand column under anoxic conditions. Appl. Geochemistry 35, 255–263.

Hansel, C.M., Benner, S.G., Fendorf, S., 2005. Competing Fe(II)-induced mineralization pathways of ferrihydrite. Environ. Sci. Technol. 39, 7147–7153.

Hansel, C.M., Benner, S.G., Neiss, J., Dohnalkova, A., Kukkadapu, R.K., Fendorf, S., 2003. Secondary mineralization pathways induced by dissimilatory iron reduction of ferrihydrite under advective flow. Geochim. Cosmochim. Acta 67, 2977–2992.

Hansel, C.M., Benner, S.G., Nico, P., Fendorf, S., 2004. Structural constraints of ferric (hydr)oxides on dissimilatory iron reduction and the fate of Fe(II). Geochim. Cosmochim. Acta 68, 3217–3229.

Hansen, H.C.B., Borggaard, O.K., Sørensen, J., 1994. Evaluation of the free energy of formation of Fe(II)-Fe(III) hydroxide-sulphate (green rust) and its reduction of nitrite. Geochim. Cosmochim. Acta 58, 2599–2608.

Hayes, J.R., Grosvenor, A.P., Rowson, J., Hughes, K., Frey, R.A., Reid, J., 2014. Analysis of the Mo speciation in the JEB tailings management facility at McClean Lake, Saskatchewan. Environ. Sci. Technol. 48, 4460–4467.

Hayes, K.F., Papelis, C., Leckie, J.O., 1988. Modeling ionic strength effects on anion adsorption at hydrous oxide/solution interfaces. J. Colloid Interface Sci. 125, 717–726.

Helz, G.R., Bura-Nakić, E., Mikac, N., Ciglenečki, I., 2011. New model for molybdenum behavior in euxinic waters. Chem. Geol. 284, 323–332.

Helz, G.R., Erickson, B.E., Vorlicek, T.P., 2014. Stabilities of thiomolybdate complexes of iron; implications for retention of essential trace elements (Fe, Cu, Mo) in sulfidic waters. Metallomics 6, 1131–1140.

Helz, G.R., Miller, C. V., Mosselmans, J.F.W., Pattrick, R.A.D., Garner, C.D., Vaughan, D.J., 1996. Mechanism of molybdenum removal from the sea and its concentration in black shales: EXAFS evidence. Geochim. Cosmochim. Acta 60, 3631–3642.

Herbel, M., Fendorf, S., 2006. Biogeochemical processes controlling the speciation and transport of arsenic within iron coated sands. Chem. Geol. 228, 16–32.

Hsu, J.-C., Lin, C.-J., Liao, C.-H., Chen, S.-T., 2008. Removal of As(V) and As(III) by reclaimed iron-oxide coated sands. J. Hazard. Mater. 153, 817–826.

Hwang, Y.S., Lenhart, J.J., 2010. Dicarboxylic acid transport through hematite-coated sand. Chemosphere 78, 1049–55.

Hwang, Y.S., Liu, J., Lenhart, J.J., Hadad, C.M., 2007. Surface complexes of phthalic acid at the hematite/water interface. J. Colloid Interface Sci. 307, 124–134.

Jolivet, J.P., Belleville, P., Tronc, E., Livage, J., 1992. Influence of Fe(II) on the formation of the spinel iron oxide in alkaline medium. Clays Clay Miner. 40, 531–539.

Kargar, M., Khorasani, N., Karami, M., Rafiee, G.-R., Naseh, R., 2011. Study of aluminum, copper and molybdenum pollution in groundwater sources surrounding (Miduk) Shahr-E-Babak Copper Complex Tailings Dam. World Acad. Sci. Eng. Technol. 52, 412–416.

Khawmee, K., Suddhiprakarn, A., Kheoruenromne, I., Singh, B., 2013. Surface charge properties of kaolinite from Thai soils. Geoderma 192, 120–131.

Kim, M., Jang, M., 2010. Adsorption of Molybdate onto Hematite: Kinetics and Equilibrium. Water Geosci. 170–173.

Kocar, B.D., Borch, T., Fendorf, S., 2010. Arsenic repartitioning during biogenic sulfidization and transformation of ferrihydrite. Geochim. Cosmochim. Acta 74, 980–994.

Kocar, B.D., Herbel, M.J., Tufano, K.J., Fendorf, S., 2006. Contrasting effects of dissimilatory iron(III) and arsenic(V) reduction on arsenic retention and transport. Environ. Sci. Technol. 40, 6715–6721.

Kozin, P.A., Salazar-Alvarez, G., Boily, J.F., 2014. Oriented aggregation of lepidocrocite and impact on surface charge development. Langmuir 30, 9017–9021.

Lang, F., Pohlmeier, A., Kaupenjohann, M., 2000. Mechanism of molybdenum sorption to iron oxides using pressure-jump relaxation. J. Plant Nutr. Soil Sci. 163, 571–575.

Latta, D.E., Gorski, C. a, Scherer, M.M., 2012. Influence of Fe^{2+}-catalysed iron oxide recrystallization on metal cycling. Biochem. Soc. Trans. 40, 1191–1197.

Legendre, G.R., Runnells, D.D., 1975. Removal of dissolved molybdenum from wastewaters by precipitates of ferric iron. Environ. Sci. Technol. 9, 744–748.

Legodi, M.A., Waal, D. de, 2007. The preparation of magnetite, goethite, hematite and maghemite of pigment quality from mill scale iron waste. Dye. Pigment. 74, 161–168.

Lindsay, M.B.J., Moncur, M.C., Bain, J.G., Jambor, J.L., Ptacek, C.J., Blowes, D.W., 2015. Geochemical and mineralogical aspects of sulfide mine tailings. Appl. Geochemistry 57, 157–177.

Lindsay, M.B.J., Ptacek, C.J., Blowes, D.W., Gould, W.D., 2008. Zero-valent iron and organic carbon mixtures for remediation of acid mine drainage: Batch experiments. Appl.

Geochemistry 23, 2214–2225.

Liu, H., Guo, H., Li, P., Wei, Y., 2009. Transformation from δ-FeOOH to hematite in the presence of trace Fe(II). J. Phys. Chem. Solids 70, 186–191.

Liu, H., Guo, H., Li, P., Wei, Y., 2008. The transformation of ferrihydrite in the presence of trace Fe(II): The effect of the anionic media. J. Solid State Chem. 181, 2666–2671.

Liu, H., Li, P., Zhu, M., Wei, Y., Sun, Y., 2007. Fe(II)-induced transformation from ferrihydrite to lepidocrocite and goethite. J. Solid State Chem. 180, 2121–2128.

Liu, H., Ma, M., Qin, M., Yang, L., Wei, Y., 2010. Studies on the controllable transformation of ferrihydrite. J. Solid State Chem. 183, 2045–2050.

Liu, H., Wei, Y., Sun, Y., 2005. The Formation of hematite from ferrihydrite using Fe(II) as a catalyst. J. Mol. Catal. A Chem. 226, 135–140.

Lovley, D.R., Phillips, E.J., 1988. Novel mode of microbial energy metabolism: organic carbon oxidation coupled to dissimilatory reduction of iron or manganese. Appl. Environ. Mcrobiology 54, 1472–1480.

Lu, B., Guo, H., Li, P., Liu, H., Wei, Y., Hou, D., 2011. Comparison study on transformation of iron oxyhydroxides: Based on theoretical and experimental data. J. Solid State Chem. 184, 2139–2144.

Masue-slowey, Y., Loeppert, R.H., Fendorf, S., 2011. Alteration of ferrihydrite reductive dissolution and transformation by adsorbed As and structural Al: Implications for As retention. Geochim. Cosmochim. Acta 75, 870–886.

McKenzie, R.M., 1983. The adsorption of molybdenum on oxide surfaces. Aust. J. Soil Res. 21, 505–513.

Mernagh, T.P., Liu, L., 1997. Temperature dependence of Raman spectra of the quartz- and rutile-types of GeO_2. Phys. Chem. Miner. 24, 7–16.

Miller, C. a., Peucker-Ehrenbrink, B., Walker, B.D., Marcantonio, F., 2011. Re-assessing the surface cycling of molybdenum and rhenium. Geochim. Cosmochim. Acta 75, 7146–7179.

Mok, W., Wal, C.M., 1990. Distribution and Mobilization of Arsenic and Antimony Species in the Coeur D'Alene River, Idaho. Environ. Sci. Technol. 24, 102–108.

Monika Hanesch, 2009. Raman spectroscopy of iron oxides and (oxy)hydroxides at low laser power and possible applications in environmental magnetic studies. Geophys. J. Int. 177, 941–948.

Ona-Nguema, G., Abdelmoula, M., Jorand, F., Benali, O., Géhin, A., Block, J.C., Génin, J.M.R., 2002. Iron(II,III) hydroxycarbonate green rust formation and stabilization from lepidocrocite

bioreduction. Environ. Sci. Technol. 36, 16–20.

Paktunc, A.D., Davé, N.K., 2002. Formation of secondary pyrite and carbonate minerals in the Lower Williams Lake tailings basin, Elliot Lake, Ontario, Canada. Am. Mineral. 87, 593–602.

Paktunc, D., 2013. Mobilization of arsenic from mine tailings through reductive dissolution of goethite influenced by organic cover. Appl. Geochemistry 36, 49–56.

Parkhurst, D.L., 1995. User's Guide To PHREEQC — A Computer Program for Speciation, Reaction-Path, Advective-Transport, and Inverse Geochemical Calculations, Water Resources Invertigations Report.

Ressler, T., Timpe, O., Neisius, T., Find, J., Mestl, G., Dieterle, M., Schlogl, R., 2000. Time-Resolved XAS Investigation of the Reduction/Oxidation of MoO_{3-x}. J. Catal. 191, 75–85.

Ressler, T., Wienold, J., Jentoft, R.E., Neisius, T., 2002. Bulk Structural Investigation of the Reduction of MoO_3 with Propene and the Oxidation of MoO_2 with Oxygen. J. Catal. 210, 67–83.

Rocco, M., Rubio, M.A., 2010. Chemical behavior of chromium, iron, lead, molybdenum, manganese and zinc in the surface water of two urban lagoons in Santiago, Chile. Fresenius Environ. Bull. 19, 438–446.

Routray, K., Zhou, W., Kiely, C.J., Grünert, W., Wachs, I.E., 2010. Origin of the synergistic interaction between MoO_3 and iron molybdate for the selective oxidation of methanol to formaldehyde. J. Catal. 275, 84–98.

Ruby, C., Géhin, A., Abdelmoula, M., Génin, J.-M.R., Jolivet, J.-P., 2003. Coprecipitation of Fe(II) and Fe(III) cations in sulphated aqueous medium and formation of hydroxysulphate green rust. Solid State Sci. 5, 1055–1062.

Rusch, B., Hanna, K., Humbert, B., 2010. Coating of quartz silica with iron oxides: Characterization and surface reactivity of iron coating phases. Colloids Surfaces A Physicochem. Eng. Asp. 353, 172–180.

Ryan, J.N., Gschwend, P.M., 1994. Effect of solution chemistry on clay colloid release from an iron oxide-coated aquifer sand. Environ. Sci. Technol. 28, 1717–1726.

Schwertmann, U., Cornell, R.M., 2000. Iron Oxides in Laboratory: Preparation and Characterization, 2nd ed, Wiley-VCH: Weinheim.

Schwertmann, U., Fechter, H., 1994. The formation of green rust and its transformation to lepidocrocite. Clay Miner. 29, 87–92.

Schwertmann, U., Stanjek, H., Becher, H.-H., 2004. Long-term in vitro transformation of 2-line ferrihydrite to goethite/hematite at 4, 10, 15 and 25°C. Clay Miner. 39, 433–438.

Sejkora, J., Čejka, J., Malíková, R., López, A., Xi, Y., Frost, R.L., 2014. A Raman spectroscopic study of a hydrated molybdate mineral ferrimolybdite, $Fe_2(MoO_4)_3 \cdot 7–8H_2O$. Spectrochim. Acta Part A Mol. Biomol. Spectrosc. 130, 83–89.

Sergent, A.S., Jorand, F., Hanna, K., 2011. Effects of Si-bearing minerals on the nature of secondary iron mineral products from lepidocrocite bioreduction. Chem. Geol. 289, 86–97.

Shannon, R.D., 1976. Revised Effective Ionic Radii and Systematic Studies of Interatomie Distances in Halides and Chaleogenides. Acta Cryst. A32, 751–767.

Sherman, D.M., Randall, S.R., 2003. Surface complexation of arsenic(V) to iron(III) (hydr)oxides: structural mechanism from ab initio molecular geometries and EXAFS spectroscopy. Geochim. Cosmochim. Acta 67, 4223–4230.

Smedley, P.L., Cooper, D.M., Ander, E.L., Milne, C.J., Lapworth, D.J., 2014. Occurrence of molybdenum in British surface water and groundwater: Distributions, controls and implications for water supply. Appl. Geochemistry 40, 144–154.

Smith, A.H., Lingas, E.O., Rahman, M., 2000. Contamination of drinking-water by arsenic in Bangladesh: a public health emergency. Bull. World Health Organ. 78, 1093–1103.

Szecsody, J.E., Zachara, J.M., Bruckhart, P.L., 1994. Adsorption-dissolution reactions affecting the distribution and stability of Co^{II} EDTA in iron oxide-coated sand. Environ. Sci. Technol. 28, 1706–1716.

Thomas, B., Masue, Y., Kukkadapu, R.K., Fendorf, S., 2007. Phosphate Imposed Limitations on Biological Reduction and Alteration of Ferrihydrite. Environ. Sci. Technol. 41, 166–172.

Tian, H., Wachs, I.E., Briand, L.E., 2005. Comparison of UV and visible Raman spectroscopy of bulk metal molybdate and metal vanadate catalysts. J. Phys. Chem. B 109, 23491–23499.

Toby, B.H., Von Dreele, R.B., 2013. GSAS-II: The genesis of a modern open-source all purpose crystallography software package. J. Appl. Crystallogr. 46, 544–549.

Tronc, E., Belleville, P., Jolivet, J.-P., Livage, J., 1992. Transformation of ferric hydroxide into spinel by Fe(II) adsorption. Langmuir 8, 313–319.

Tufano, K.J., Fendorf, S., 2008. Confounding impacts of iron reduction on arsenic retention. Environ. Sci. Technol. 42, 4777–4783.

Tufano, K.J., Reyes, C., Saltikov, C.W., Fendorf, S., 2008. Reductive processes controlling arsenic retention: revealing the relative importance of iron and arsenic reduction. Environ. Sci. Technol. 42, 8283–9.

Usman, M., Abdelmoula, M., Hanna, K., Grégoire, B., Faure, P., Ruby, C., 2012a. Fe^{II} induced mineralogical transformations of ferric oxyhydroxides into magnetite of variable stoichiometry and morphology. J. Solid State Chem. 194, 328–335.

Usman, M., Hanna, K., Abdelmoula, M., Zegeye, A., Faure, P., Ruby, C., 2012b. Formation of green rust via mineralogical transformation of ferric oxides (ferrihydrite, goethite and hematite). Appl. Clay Sci. 64, 38–43.

Vlek, P.L.G., Lindsay, W.L., 1977. Thermodynamic Stability and Solubility of Molybdenum Minerals In Soils. Soil Sci. Soc. Am. J. 41, 42–46.

Wang, Y., Morin, G., Ona-Nguema, G., Brown, G.E., 2014. Arsenic(III) and Arsenic(V) speciation during transformation of lepidocrocite to magnetite. Environ. Sci. Technol. 48(24), 14282–14290.

WHO, 2011. Molybdenum in Drinking-water, WHO Guidelines for Drinking-water Quality.

Xu, N., Braida, W., Christodoulatos, C., Chen, J., 2013. A review of molybdenum adsorption in soils/bed sediments: Speciation, mechanism, and model applications. Soil Sediment Contam. 22, 912–929.

Xu, N., Christodoulatos, C., Braida, W., 2006. Adsorption of molybdate and tetrathiomolybdate onto pyrite and goethite: effect of pH and competitive anions. Chemosphere 62, 1726–1735.

Xu, Y., Axe, L., 2005. Synthesis and characterization of iron oxide-coated silica and its effect on metal adsorption. J. Colloid Interface Sci. 282, 11–9.

Yang, L., Steefel, C.I., Marcus, M.A., Bargar, J.R., 2010. Kinetics of Fe(II)-catalyzed transformation of 6-line ferrihydrite under anaerobic flow conditions. Environ. Sci. Technol. 44, 5469–5475.

Zachara, J.M., Kukkadapu, R.K., Fredrickson, J.K., Gorby, Y.A., Smith, S.C., 2002. Biomineralization of poorly crystalline Fe(III) oxides by dissimilatory metal reducing bacteria (DMRB). Geomicrobiol. J. 19, 179–207.

Zachara, J.M., Kukkadapu, R.K., Peretyazhko, T., Bowden, M., Wang, C., Kennedy, D.W., Moore, D., Arey, B., 2011. The mineralogic transformation of ferrihydrite induced by heterogeneous reaction with bioreduced anthraquinone disulfonate (AQDS) and the role of phosphate. Geochim. Cosmochim. Acta 75, 6330–6349.

Zegeye, A., Ruby, C., Jorand, F., 2007. Kinetic and thermodynamic analysis during dissimilatory γ-FeOOH reduction: formation of green rust 1 and magnetite. Geomicrobiol. J. 24, 51–64.

Zhang, P.C., Sparks, D.L., 1989. Kinetics and mechanisms of molybdate adsorption/desorption at the goethite/waterinterface using pressure-Jump relaxation. Soil Sci. Soc. Am. J. 53, 1028–1034.

Zhao, Z., Jia, Y., Xu, L., Zhao, S., 2011. Adsorption and heterogeneous oxidation of As(III) on ferrihydrite. Water Res. 45, 6496–6504.

Appendix A: Column geochemistry raw data and supporting figures

Table A.1: Fe concentrations measured by ICP-OES and Ferrozine method (mg L^{-1}, input solutions only).

Sample ID	Low Fe			High Fe		
	ICP-OES	Ferrozine		ICP-OES	Ferrozine	
		Fe(II)	Fe_{tot}		Fe(II)	Fe_{tot}
KQ-MC-1	9.68	8.98	10.41	92.92	91.81	111.64
KQ-MC-2	9.99	10.23	11.15	101.91	104.34	111.52
KQ-MC-3	11.94	12.49	13.38	98.68	98.71	109.72
KQ-MC-4	12.05	12.16	14.01	99.38	100.30	108.98
KQ-MC-5	10.17	10.10	11.24	94.37	90.98	101.00
KQ-MC-6	13.14	13.53	14.22	99.30	100.23	112.39
KQ-MC-7	11.72	11.94	12.79	99.02	98.48	108.12
KQ-MC-8	9.70	9.53	10.06	98.51	100.12	108.52
KQ-MC-9	9.76	9.47	10.51	89.68	79.45	87.17
KQ-MC-10	12.59	13.08	14.10	98.53	97.39	106.48
KQ-MC-11	9.26	12.04	12.65	100.24	106.44	116.60
KQ-MC-12	11.60	11.18	12.07	100.56	100.87	108.83
KQ-MC-13	9.81	9.25	10.50	104.77	96.78	104.99
KQ-MC-14	10.50	10.17	10.86	102.21	97.37	106.33
KQ-MC-15	10.19	9.88	10.82	106.47	99.21	108.85
KQ-MC-16	9.59	8.21	9.88	100.17	101.78	107.33
KQ-MC-17	12.07	11.71	12.51	104.50	104.55	109.18
KQ-MC-18	11.37	10.18	11.10	103.31	95.09	103.61
KQ-MC-19	10.68	10.00	10.74	103.26	96.88	101.59
KQ-MC-20	10.41	10.09	10.81	102.63	99.50	104.68
KQ-MC-21	12.33	11.86	12.92	105.42	99.28	108.50
KQ-MC-22	12.75	12.29	13.54	102.60	98.77	109.13
KQ-MC-23	9.30	8.81	9.64	101.06	104.59	109.39
KQ-MC-24	10.70	10.99	11.20	101.32	105.37	106.52

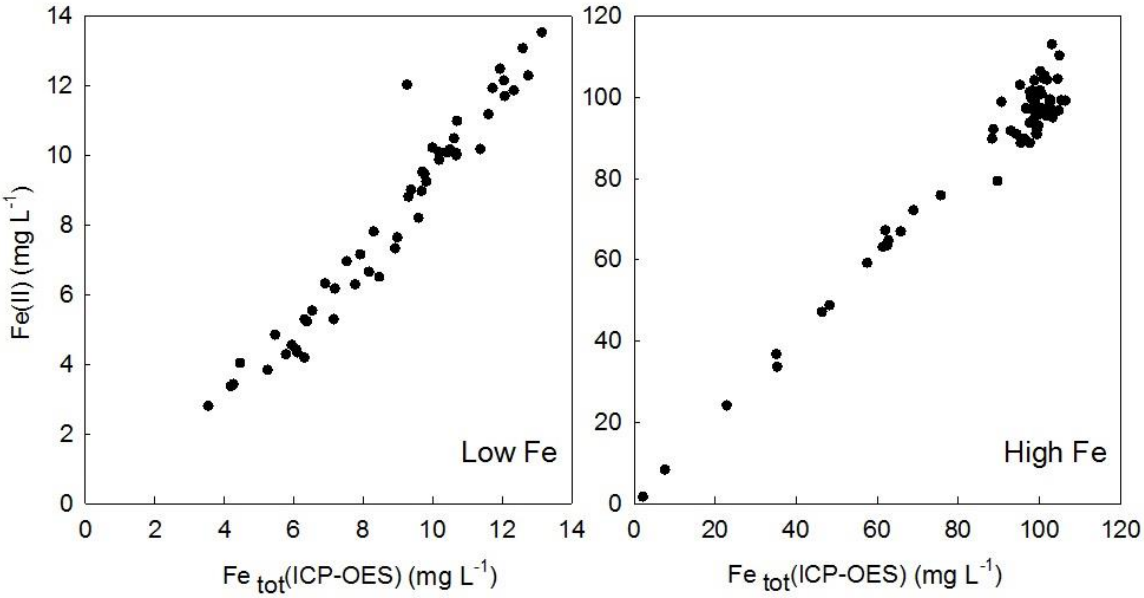

Figure A.1: Comparison of Fe(II) and Fe_{tot}(ICP-OES) concentrations from column influent and effluent. Left: low Fe influent and effluent (KQ-2 and KQ-8); Right: high Fe influent and effluent (KQ-3 and KQ-9).

Table A.2: Solid-phase concentrations of Fe, Mo, and S (per kg sand) and the mass ratio: Mo/Fe along the column length.

KQ-1				
Column Length	mg S/kg	mg Fe/kg	mg Mo/kg	Mass Ratio: Mo/Fe
1	20.31	3131.74	90.85	0.029
5	64.40	3451.10	98.70	0.029
7	53.78	3399.55	94.77	0.028
13	51.49	3344.76	87.10	0.026
17	96.05	3132.26	72.45	0.023
21.5	73.62	3431.29	79.84	0.023
KQ-2				
Column Length	mg S/kg	mg Fe/kg	mg Mo/kg	Mass Ratio: Mo/Fe
1	46.54	3356.36	47.55	0.014
5	74.16	3041.36	65.14	0.021
7	51.81	3822.63	81.09	0.021
11	32.10	2632.69	62.32	0.024
13	44.51	3145.17	62.10	0.020
17	75.99	2897.34	55.18	0.019
21.5	158.90	3422.37	65.22	0.019
KQ-3				
Column Length	mg S/kg	mg Fe/kg	mg Mo/kg	Mass Ratio: Mo/Fe
1	34.36	3509.92	89.27	0.025
5	64.22	3077.53	84.49	0.027

7	34.16	3056.43	85.48	0.028
13	47.53	3119.98	84.92	0.027
17	162.82	2841.85	77.97	0.027
21.5	104.51	2883.01	78.74	0.027

KQ-4

Column Length	mg S/kg	mg Fe/kg	mg Mo/kg	Mass Ratio: Mo/Fe
1	23.11	1030.08	11.00	0.011
5	30.18	1164.12	14.34	0.012
7	37.73	1238.95	13.47	0.011
13	43.17	1241.38	12.99	0.010
17	62.53	1159.40	13.81	0.012
21.5	56.91	1064.82	10.94	0.010

KQ-7

Column Length	mg S/kg	mg Fe/kg	mg Mo/kg	Mass Ratio: Mo/Fe
1	50.09	2802.94	310.23	0.111
5	47.58	2524.96	262.43	0.104
7	91.79	2545.12	255.30	0.100
13	107.61	2547.35	207.50	0.081
17	100.84	2679.13	16.54	0.006
21.5	132.53	2592.88	0.00	0.000

KQ-8

Column Length	mg S/kg	mg Fe/kg	mg Mo/kg	Mass Ratio: Mo/Fe
1	71.58	2842.93	108.36	0.038
5	61.58	2330.41	188.23	0.081
7	69.19	2710.77	249.46	0.092
13	82.76	2745.09	253.53	0.092
17	88.72	2440.23	210.12	0.086
21.5	135.48	2793.97	229.95	0.082

KQ-9

Column Length	mg S/kg	mg Fe/kg	mg Mo/kg	Mass Ratio: Mo/Fe
1	36.44	3106.42	290.94	0.094
5	44.77	2776.89	279.45	0.101
7	56.28	3032.42	299.01	0.099
13	67.18	2994.71	286.60	0.096
17	68.92	2540.07	229.89	0.091
21.5	107.65	2608.37	224.44	0.086

Table A.3: Column KQ-2: influent and effluent concentrations (mg L^{-1}) of SO_4^{2-}, Mo, Fe, alkalinity ($CaCO_3$), and pH.

	pH		Alkalinity		SO_4		Mo		Fe	
PV	Input	KQ-2	Input	KQ-2	Input	KQ-2	Input	KQ-2	Input	KQ-2
1.6	6.55	6.55	202.3	215.0	581.8	558.4	10.74	0.00	0.00	0.00
7.2	6.55	6.55	189.0	186.6	575.7	565.1	10.12	0.03	0.00	0.00
13.6	6.54	6.55	182.2	198.6	559.6	560.1	10.29	0.03	0.00	0.00
19.2	6.54	6.55	182.1	192.3	697.2	584.2	8.58	0.42	0.00	0.00
24.7	6.53	6.53	187.4	197.0	564.1	572.1	9.84	6.64	0.00	0.00
29.4	6.53	6.54	201.3	196.3	567.8	548.0	10.05	8.11	0.00	0.00
32.3	6.56	6.56	203.6	198.2	607.8	683.6	9.42	7.94	0.00	0.00
35.8	6.53	6.54	195.9	188.7	564.8	561.5	10.24	8.67	0.00	0.00
41.0	6.53	6.55	189.4	192.7	559.1	569.5	10.00	8.85	0.00	0.00
46.9	6.52	6.53	188.0	199.0	563.5	560.8	10.32	8.34	0.00	0.00
51.1	6.49	6.52	195.2	196.4	557.1	546.5	10.35	8.59	0.00	0.00
55.7	6.53	6.53	186.0	190.0	736.3	582.9	10.11	8.72	0.00	0.00
62.5	6.52	6.51	189.9	191.8	739.9	581.9	10.10	9.21	0.00	0.00
70.6	6.51	6.50	190.7	188.8	499.9	489.4	9.68	9.62	0.00	0.00
88.7	6.53	6.53	192.5	187.8	538.9	541.3	10.28	9.07	0.00	0.00
101.4	6.54	6.51	198.8	190.8	482.5	481.5	9.64	10.03	0.00	0.00
116.4	6.56	6.54	202.2	201.0	560.2	559.5	10.67	10.13	0.00	0.00
118.6	6.60	6.59	194.8	223.2	555.8	549.3	0.00	12.72	9.68	0.00
119.8	6.60	6.53	192.7	183.9	554.4	572.8	0.00	9.09	9.99	0.01
121.1	6.57	6.49	207.7	200.0	678.5	608.8	0.00	7.78	11.94	0.03
122.2	6.63	6.50	210.0	178.2	588.6	580.9	0.00	7.19	12.05	0.01
123.1	6.62	6.53	209.7	207.5	577.7	584.1	0.00	7.24	10.17	0.01
124.2	6.64	6.55	217.6	210.3	582.4	561.5	0.00	6.77	13.14	0.01
125.3	6.64	6.55	214.1	209.8	575.1	572.2	0.00	6.10	11.72	0.01
127.1	6.66	6.58	211.0	217.0	610.6	591.9	0.00	5.32	9.70	0.04
129.5	6.65	6.59	216.8	211.8	625.7	624.3	0.00	4.01	9.76	0.01
131.8	6.63	6.58	210.6	207.0	528.3	499.6	0.00	2.74	12.59	0.73
134.1	6.58	6.56	193.8	201.2	502.7	522.3	0.00	1.13	9.26	3.54
137.7	6.61	6.61	215.0	215.4	604.0	597.2	0.00	0.40	11.60	6.31
141.8	6.63	6.64	214.8	209.2	529.3	536.8	0.00	0.31	9.81	7.18
145.4	6.61	6.60	203.7	200.4	515.8	518.3	0.00	0.25	10.50	7.15
148.3	6.60	6.60	197.2	200.4	516.4	529.0	0.00	0.21	10.19	7.77
150.7	6.59	6.60	198.4	200.0	534.1	530.8	0.00	0.18	9.59	8.46
153.6	6.56	6.57	199.4	183.8	563.4	555.7	0.00	0.15	12.07	8.16
157.1	6.61	6.60	206.8	204.8	584.6	583.7	0.00	0.13	11.37	8.98
160.1	6.57	6.60	215.1	209.3	584.6	580.6	0.00	0.12	10.68	8.91
163.1	6.62	6.59	213.0	218.3	592.7	599.2	0.00	0.11	10.41	8.30
166.5	6.67	6.68	216.8	214.0	684.7	695.8	0.00	0.11	12.33	7.92
170.1	6.69	6.69	210.6	211.7	529.0	538.8	0.00	0.10	12.75	9.37
173.6	6.53	6.53	191.0	187.3	523.8	503.1	0.00	0.06	9.30	10.68
177.7	6.52	6.56	185.1	194.0	530.8	528.5	0.00	0.06	10.70	10.61

Table A.4: Column KQ-3: influent and effluent concentrations (mg L^{-1}) of SO_4^{2-}, Mo, Fe, alkalinity ($CaCO_3$), and pH.

	pH		Alkalinity		SO_4		Mo		Fe	
PV	Input	KQ-3	Input	KQ-3	Input	KQ-3	Input	KQ-3	Input	KQ-3
1.6	6.55	6.56	202.3	213.6	581.8	687.3	10.74	0.00	0.00	0.00
7.2	6.55	6.55	189.0	194.6	575.7	562.1	10.12	0.01	0.00	0.00
13.5	6.54	6.56	182.2	183.5	559.6	583.4	10.29	0.01	0.00	0.00
19.2	6.54	6.54	182.1	194.0	697.2	567.2	8.58	2.14	0.00	0.00
24.7	6.53	6.53	187.4	202.8	564.1	564.0	9.84	7.11	0.00	0.00
29.3	6.53	6.54	201.3	194.2	567.8	576.1	10.05	8.39	0.00	0.00
32.2	6.56	6.55	203.6	193.5	607.8	708.1	9.42	7.76	0.00	0.00
35.7	6.53	6.54	195.9	195.5	564.8	566.9	10.24	8.82	0.00	0.00
40.9	6.53	6.54	189.4	205.7	559.1	651.8	10.00	7.83	0.00	0.00
46.8	6.52	6.52	188.0	197.2	563.5	560.7	10.32	8.46	0.00	0.00
51.0	6.49	6.52	195.2	191.8	557.1	558.7	10.35	8.74	0.00	0.00
55.6	6.53	6.52	186.0	189.9	736.3	627.1	10.11	8.95	0.00	0.00
62.4	6.52	6.50	189.9	189.7	739.9	586.3	10.10	9.23	0.00	0.00
70.5	6.51	6.50	190.7	186.2	499.9	509.5	9.68	9.79	0.00	0.00
88.6	6.53	6.54	192.5	194.0	538.9	557.3	10.28	9.21	0.00	0.00
101.3	6.54	6.52	198.8	191.8	482.5	453.5	9.64	9.90	0.00	0.00
116.3	6.56	6.54	202.2	209.0	560.2	555.6	10.67	10.12	0.00	0.00
118.4	6.55	6.59	192.2	206.2	552.5	587.1	0.00	13.18	92.92	0.00
119.6	6.54	5.85	198.7	72.4	580.9	561.7	0.00	2.35	101.91	7.64
120.9	6.51	5.99	194.1	94.6	619.3	604.3	0.00	0.73	98.68	35.08
121.9	6.62	6.22	212.2	128.0	587.5	602.6	0.00	0.68	99.38	48.26
122.8	6.62	6.34	211.9	176.2	576.7	567.0	0.00	0.54	94.37	57.55
124.0	6.58	6.44	219.2	173.0	569.9	559.8	0.00	0.41	99.30	68.95
125.1	6.64	6.49	212.6	206.2	598.5	595.2	0.00	0.32	99.02	88.36
126.8	6.63	6.57	213.8	200.0	608.4	597.0	0.00	0.24	98.51	88.69
129.2	6.61	6.60	212.4	214.1	625.0	628.8	0.00	0.19	89.68	97.71
131.5	6.64	6.60	215.6	213.0	544.4	506.4	0.00	0.17	98.53	90.69
133.7	6.66	6.62	211.6	214.8	556.8	519.2	0.00	0.14	100.24	95.23
137.2	6.64	6.59	212.6	213.8	595.3	634.5	0.00	0.12	100.56	96.90
141.3	6.63	6.64	204.0	218.2	540.1	537.0	0.00	0.12	104.77	99.61
144.8	6.58	6.58	188.5	206.3	517.9	515.9	0.00	0.11	102.21	101.88
147.7	6.60	6.58	197.6	196.8	533.4	530.5	0.00	0.10	106.47	100.86
150.1	6.60	6.59	208.0	213.0	515.2	525.7	0.00	0.09	100.17	99.16
153.0	6.57	6.55	196.2	205.8	553.5	550.6	0.00	0.09	104.50	98.81
156.4	6.59	6.56	206.0	209.1	585.9	587.9	0.00	0.08	103.31	99.83
159.4	6.58	6.57	203.3	209.3	581.2	588.3	0.00	0.08	103.26	99.22
162.3	6.59	6.56	212.0	209.8	600.9	592.4	0.00	0.08	102.63	98.56
165.7	6.66	6.64	212.0	210.6	689.5	694.9	0.00	0.07	105.42	101.88
169.2	6.68	6.66	214.8	208.8	517.7	529.7	0.00	0.07	102.60	100.08
172.7	6.56	6.60	192.0	197.6	524.6	520.3	0.00	0.06	101.06	103.12
176.7	6.53	6.60	201.6	184.0	550.4	525.0	0.00	0.06	101.32	98.28

Table A.5: Column KQ-8: influent and effluent concentrations (mg L^{-1}) of SO_4^{2-}, Mo, Fe, alkalinity ($CaCO_3$), and pH.

	pH		Alkalinity		SO4		Mo		Fe	
PV	Input	KQ-8	Input	KQ-8	Input	KQ-8	Input	KQ-8	Input	KQ-8
1.6	6.55	6.42	202.3	199.5	581.8	674.7	10.74	0.00	0.00	0.00
7.4	6.55	6.56	189.0	195.1	575.7	609.3	10.12	0.01	0.00	0.00
19.8	6.54	6.54	182.1	192.5	697.2	583.5	8.58	0.02	0.00	0.00
34.3	6.56	6.56	203.6	202.6	607.8	656.6	9.42	0.03	0.00	0.00
43.3	6.53	6.56	189.4	192.0	559.1	574.4	10.00	0.04	0.00	0.00
58.5	6.53	6.55	186.0	194.2	736.3	719.3	10.11	0.01	0.00	0.00
65.5	6.52	6.50	189.9	185.2	739.9	587.7	10.10	0.01	0.00	0.00
73.8	6.51	6.52	190.7	191.1	499.9	509.5	9.68	0.01	0.00	0.00
81.0	6.51	6.54	191.3	204.0	569.1	582.2	9.34	0.01	0.00	0.00
85.1	6.53	6.54	191.3	187.4	574.9	579.3	9.36	0.01	0.00	0.00
88.8	6.54	6.55	202.9	196.0	567.3	572.9	9.60	2.21	0.00	0.00
92.6	6.53	6.55	192.5	193.6	538.9	458.1	10.28	5.19	0.00	0.00
95.4	6.52	6.53	186.9	196.6	536.1	536.6	9.75	6.11	0.00	0.00
98.8	6.52	6.54	190.2	196.7	576.1	572.3	9.83	6.63	0.00	0.00
102.5	6.53	6.52	191.7	190.2	631.1	682.1	10.03	6.51	0.00	0.00
104.4	6.56	6.55	205.2	206.3	743.4	722.3	9.51	7.54	0.00	0.00
105.6	6.54	6.52	198.8	193.4	482.5	453.2	9.64	7.90	0.00	0.00
107.3	6.53	6.54	193.2	196.4	574.8	597.3	9.87	8.47	0.00	0.00
110.7	6.53	6.53	205.2	195.2	700.3	678.5	10.15	9.11	0.00	0.00
117.7	6.54	6.54	204.9	195.9	725.2	643.8	9.27	8.08	0.00	0.00
121.2	6.56	6.55	202.2	204.6	560.2	566.1	10.67	8.20	0.00	0.00
123.3	6.60	6.58	194.8	209.8	555.8	564.9	0.00	10.62	9.68	0.00
124.6	6.60	6.58	192.7	200.9	554.4	546.5	0.00	10.44	9.99	0.01
126.0	6.57	6.51	207.7	199.0	678.5	620.7	0.00	8.19	11.94	0.00
127.0	6.63	6.49	210.0	183.8	588.6	573.3	0.00	7.64	12.05	0.00
128.0	6.62	6.51	209.7	208.0	577.7	566.4	0.00	7.49	10.17	0.01
129.1	6.64	6.55	217.6	194.8	582.4	584.9	0.00	8.11	13.14	0.01
130.3	6.64	6.55	214.1	217.0	575.1	593.3	0.00	8.37	11.72	0.01
132.1	6.66	6.57	211.0	205.2	610.6	601.8	0.00	8.54	9.70	0.07
134.6	6.65	6.60	216.8	211.4	625.7	619.3	0.00	8.29	9.76	0.01
137.0	6.63	6.58	210.6	215.8	528.3	522.6	0.00	7.46	12.59	0.05
139.3	6.58	6.58	193.8	197.0	502.7	530.4	0.00	4.15	9.26	4.19
143.0	6.61	6.62	215.0	215.8	604.0	615.0	0.00	1.74	11.60	6.53
147.2	6.63	6.63	214.8	216.8	529.3	513.2	0.00	1.42	9.81	6.38
150.9	6.61	6.59	203.7	200.0	515.8	523.2	0.00	1.21	10.50	6.30
153.9	6.60	6.59	197.2	202.8	516.4	527.8	0.00	1.09	10.19	5.94
156.4	6.59	6.58	198.4	201.0	534.1	531.5	0.00	0.97	9.59	6.10
159.4	6.56	6.55	199.4	190.0	563.4	566.7	0.00	0.80	12.07	6.07
163.0	6.61	6.55	206.8	209.1	584.6	597.6	0.00	0.69	11.37	5.77
166.1	6.57	6.57	215.1	204.8	584.6	587.5	0.00	0.64	10.68	5.25
169.1	6.62	6.55	213.0	202.8	592.7	602.4	0.00	0.57	10.41	5.46
172.6	6.67	6.66	216.8	212.9	684.7	712.1	0.00	0.56	12.33	4.45
176.3	6.69	6.66	210.6	207.8	529.0	551.1	0.00	0.48	12.75	4.26

179.9	6.53	6.54	191.0	182.2	523.8	508.9	0.00	0.31	9.30	7.52
184.2	6.57	6.52	185.1	192.8	530.8	526.9	0.00	0.27	10.70	6.90

Table A.6: Column KQ-9: influent and effluent concentrations (mg L^{-1}) of SO_4^{2-}, Mo, Fe, alkalinity ($CaCO_3$), and pH.

	pH		Alkalinity		SO4		Mo		Fe	
PV	Input	KQ-9	Input	KQ-9	Input	KQ-9	Input	KQ-9	Input	KQ-9
1.6	6.55	6.44	202.3	197.4	581.8	565.2	10.74	0.00	0.00	0.00
7.5	6.55	6.56	189.0	204.7	575.7	557.0	10.12	0.00	0.00	0.00
20.0	6.54	6.54	182.1	192.1	697.2	582.6	8.58	0.01	0.00	0.00
34.6	6.56	6.56	203.6	193.2	607.8	680.3	9.42	0.01	0.00	0.00
43.7	6.53	6.56	189.4	192.6	559.1	556.6	10.00	0.02	0.00	0.00
59.0	6.53	6.55	186.0	194.8	736.3	580.5	10.11	0.00	0.00	0.00
66.0	6.52	6.52	189.9	185.2	739.9	731.9	10.10	0.00	0.00	0.00
74.4	6.51	6.52	190.7	184.1	499.9	485.2	9.68	0.01	0.00	0.00
81.7	6.51	6.54	191.3	207.1	569.1	665.5	9.34	0.02	0.00	0.00
85.8	6.53	6.53	191.3	191.0	574.9	571.0	9.36	1.65	0.00	0.00
89.6	6.54	6.54	202.9	195.6	567.3	574.8	9.60	4.81	0.00	0.00
93.4	6.53	6.55	192.5	183.3	538.9	454.5	10.28	6.53	0.00	0.00
96.2	6.52	6.53	186.9	193.0	536.1	504.9	9.75	6.69	0.00	0.00
99.6	6.52	6.54	190.2	189.7	576.1	575.8	9.83	6.90	0.00	0.00
103.3	6.53	6.53	191.7	187.8	631.1	651.1	10.03	6.84	0.00	0.00
105.3	6.56	6.56	205.2	205.0	743.4	685.9	9.51	7.77	0.00	0.00
106.5	6.54	6.52	198.8	188.4	482.5	458.0	9.64	8.03	0.00	0.00
108.1	6.53	6.54	193.2	206.9	574.8	574.6	9.87	8.74	0.00	0.00
111.6	6.53	6.53	205.2	201.2	700.3	736.2	10.15	9.24	0.00	0.00
118.7	6.54	6.54	204.9	199.0	725.2	641.4	9.27	8.11	0.00	0.00
122.2	6.56	6.55	202.2	211.4	560.2	551.7	10.67	8.27	0.00	0.00
124.3	6.55	6.58	192.2	202.4	552.5	549.3	0.00	9.50	92.92	0.06
125.6	6.54	6.53	198.7	200.0	580.9	503.2	0.00	9.59	101.91	0.00
127.0	6.51	6.07	194.1	102.4	619.3	629.7	0.00	3.02	98.68	2.22
128.0	6.62	5.90	212.2	87.0	587.5	564.8	0.00	1.09	99.38	22.87
129.0	6.62	6.11	211.9	107.3	576.7	545.6	0.00	1.28	94.37	35.32
130.1	6.58	6.28	219.2	143.1	569.9	547.6	0.00	1.45	99.30	46.34
131.3	6.64	6.35	212.6	179.2	598.5	572.6	0.00	1.36	99.02	61.37
133.1	6.63	6.41	213.8	163.8	608.4	567.4	0.00	1.09	98.51	62.42
135.6	6.61	6.40	212.4	164.0	625.0	609.6	0.00	0.68	89.68	65.81
138.0	6.64	6.39	215.6	151.2	544.4	555.5	0.00	0.50	98.53	62.75
140.3	6.66	6.34	211.6	146.3	556.8	559.4	0.00	0.16	100.24	61.97
144.0	6.64	6.42	212.6	163.8	595.3	666.2	0.00	0.10	100.56	75.69
148.2	6.63	6.57	204.0	181.0	540.1	547.0	0.00	0.04	104.77	95.40
151.9	6.58	6.53	188.5	182.1	517.9	525.3	0.00	0.01	102.21	96.29
154.9	6.60	6.56	197.6	189.4	533.4	525.0	0.00	0.01	106.47	97.64
157.4	6.60	6.57	208.0	201.4	515.2	530.6	0.00	0.01	100.17	98.85
160.4	6.57	6.54	196.2	198.0	553.5	567.3	0.00	0.01	104.50	97.98
164.0	6.59	6.55	206.0	200.6	585.9	586.3	0.00	0.01	103.31	99.44

167.1	6.58	6.56	203.3	212.0	581.2	585.6	0.00	0.01	103.26	97.69
170.1	6.59	6.55	212.0	205.6	600.9	606.2	0.00	0.01	102.63	98.79
173.6	6.66	6.64	212.0	205.8	689.5	694.5	0.00	0.01	105.42	99.44
177.3	6.68	6.66	214.8	206.4	517.7	525.2	0.00	0.01	102.60	96.70
180.9	6.56	6.61	192.0	199.4	524.6	516.1	0.00	0.01	101.06	104.94
185.2	6.53	6.60	201.6	181.3	550.4	540.4	0.00	0.01	101.32	98.82

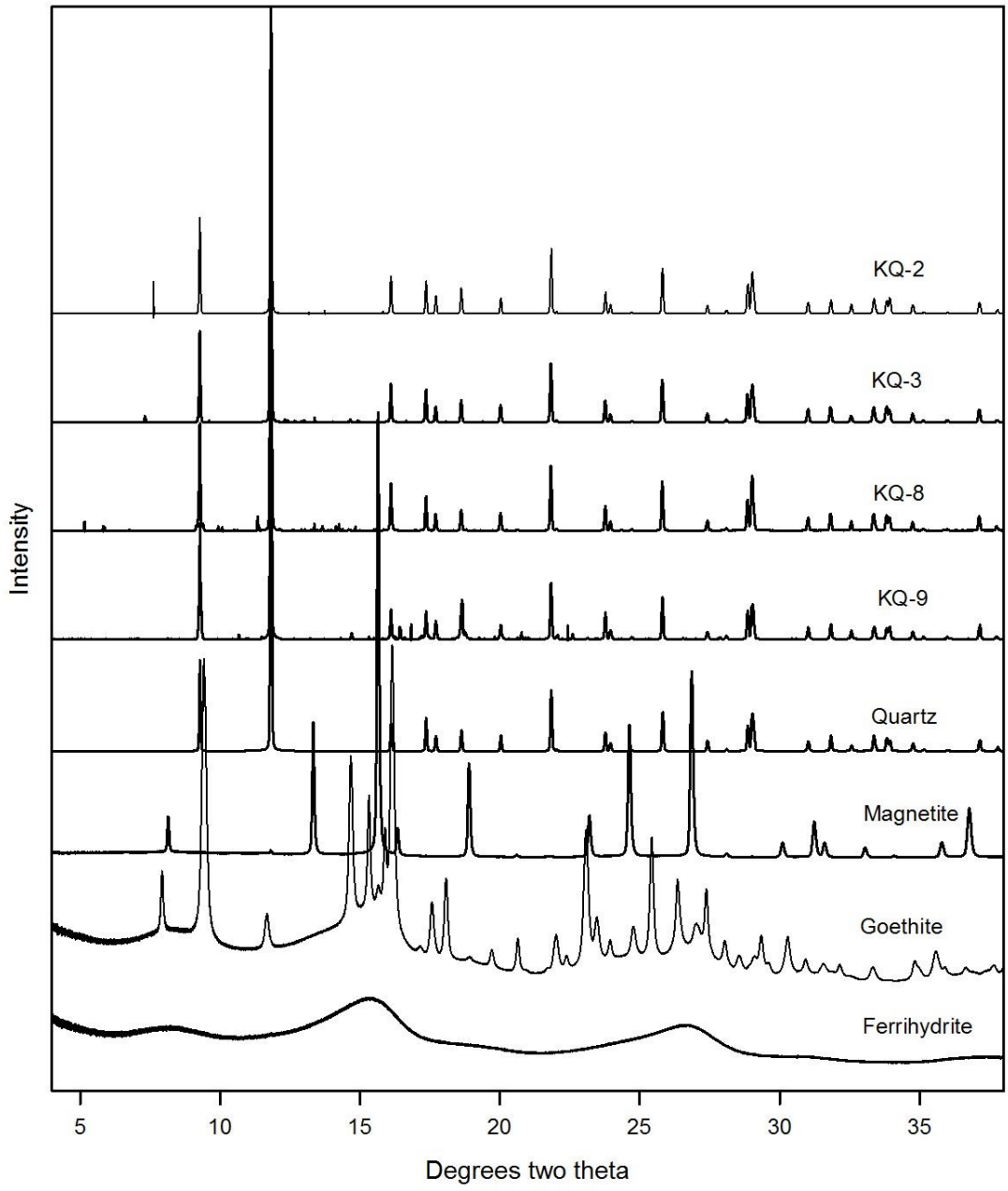

Figure A.2: PXRD patterns for of synthesized Fe (hydr)oxides and the sand samples.